

REPORT DOCUMENTATION PAGE

0662

Public reporting burden for this collection of information is estimated to average 1 hour per response, including the time for reviewing instructions, searching, collecting, maintaining the data needed, and completing and reviewing the collection of information. Send comments regarding this burden estimate or any other aspect of this collection of information, including suggestions for reducing this burden, to Washington Headquarters Services, Directorate for Information Operations and Reports, 1215 Jefferson Davis Highway, Suite 1204, Arlington, VA 22202-4302, and to the Office of Management and Budget, Paperwork Reduction Project (0704-0188), Washington, DC 20503.

1. AGENCY USE ONLY (Leave blank)	2. REPORT DATE November 7, 2000	3. REPORT TYPE AND DATES COVERED Final Report, 6/15/96 - 12/14/99	
4. TITLE AND SUBTITLE Advanced Concepts for Boundary Layer Control		5. FUNDING NUMBERS G: F49620-96-1-0296	
6. AUTHORS John Kim			
7. PERFORMING ORGANIZATION NAME(S) AND ADDRESS(ES) Mechanical and Aerospace Engineering Department 48-121 Engineering IV, Box 951597 University of California, Los Angeles Los Angeles, CA 90095-1597		8. PERFORMING ORGANIZATION REPORT NUMBER	
9. SPONSORING/MONITORING AGENCY NAME(S) AND ADDRESS(ES) AFOSR/NA 801 N. Randolph Street, Room 732 Arlington, VA 22203-1977		10. SPONSORING/MONITORING AGENCY REPORT NUMBER	
11. SUPPLEMENTARY NOTES The views, opinions and/or findings contained in this report are those of the author(s) and should not be construed as an official Department of the Air Force position, policy or decision, unless so designated by other documentation.			
12a. DISTRIBUTION/AVAILABILITY STATEMENT Approved for public release; distribution unlimited		12b. DISTRIBUTION CODE UL	
13. ABSTRACT (Maximum 200 words) A series of numerical experiments were performed to explore new control strategies suitable for distributed control. All numerical experiments were performed in a fully developed turbulent channel flow. Three different control schemes were developed. These include applications of a neural network, a suboptimal control theory and systems control theory. In all cases, substantial drag reductions were achieved. A simple feedback law obtained from the neural network was implemented into a chip, which contains microelectronics (for the control logic), microsensors and microactuators (M^3 chip). All cases used surface blowing and suction as control input. Development of a new numerical method for simulating a turbulent flow over distributed microflap actuators is included.			
14. SUBJECT TERMS Turbulent boundary layer control		15. NUMBER OF PAGES 66	
		16. PRICE CODE	
17. SECURITY CLASSIFICATION OF REPORT Unclassified	18. SECURITY CLASSIFICATION OF THIS PAGE Unclassified	19. SECURITY CLASSIFICATION OF ABSTRACT Unclassified	20. LIMITATION OF ABSTRACT UL

NSN 7540-01-280-5500

Computer Generated

STANDARD FORM 298 (Rev 2-89)

Prescribed by ANSI Std 239-18
298-102

NA

14 Nov 00

Acknowledgement of Receipt and Acceptance of Final Technical Report

PK

1. Reference F49620-96-1-0296

Grant or Contract Number

Univ of California, Los A/Kim

Institution and Principal Investigator

2. Status on the FINAL REPORT covering the period
15 Jun 96 to 14 Dec 99 is as follows

(X) Received on 19 Oct 00

(X) Accepted on 22 Nov 00

() Unacceptable - Grantee/Contractor informed of resubmission
suspend date of _____

() Other: _____


DR. THOMAS BEUTNER
Program Manager

*** DTIC DATA ***

P. R. NUMBER: FQ8671-9601134
PROPOSAL NUMBER: 96-NA-060 (located in 6060a, pg 10)
TYPE SUBMISSION: Final Report
INST. CONTROL NUMBER: F49620-96-1-0296
INSTITUTION: Univ of California, Los Angeles
P.I. NAME: Professor John Kim
INVENTION IND: NONE
PROJECT/TASK: 3484 WS
PROGRAM MANAGER: Dr. Thomas Beutner

1. Objective:@36.1@UNARR. ----- OBJT.

!!The objective of this research was to explore new concepts for boundary layer control using neural networks and surface arrays of sensors and actuators.

2. Approach:@37.1@UNARR. ----- APPR.

The research conducted numerical simulations of turbulent boundary layers under the influence of distributed arrays of nerual network controlled sensors and actuators.

3. Progress:@38.1@UNARR. ----- PROG. - FROM DD MMM YY TO DD MMM YY

Insertion of a microflap into the flow domain creates an internal boundary which must be simulated properly. We used an idea of Peskin and McQueen (1989) of using a body force to represent the dynamical effect on the fluid of a moving wall immersed in the fluid. In their method, and our application1 the position of the internal boundary within the flow domain does not generally coincide with the computational mesh. Flow properties are interpolated from the computational mesh to the locations of boundary nodes in order to calculate the force of the boundary on the fluid. Then that force is distributed onto nodes of the computational mesh near the internal boundary.

The force in Peskin and McQueen's work was based on a balance of tension in an elastic wall against the hydrodynamic forces. We instead use an idea developed by Jamaludin Mohd-Yusof (1997) of creating a fictitious force constructed so as to drive the velocity at desired locations to desired values. In his application, the desired locations are a riblet surface and the desired values are zero to fulfill the no-slip condition. In our application, the desired locations are the flap positions and the desired values are the flap velocities, also to fulfill the no-slip condition. A difference in Mohd-Yusof's application and ours is the moving boundary created by the flap. Another difference is that the flap is an internal boundary with flow on both sides. Mohd-Yusof's riblet surface is an external boundary with only one side within the flow domain. There was some question whether we could use this method with an internal boundary. It was used, however, to simulate internal boundaries in some simple flows with known analytic solutions, and it did converge to the proper results.

4. Progress:

A series of numerical experiments were performed to explore new control strategies suitable for distributed control. All computations were conducted in two-dimensional channel geometry. The Reynolds numbers, based on the wall-shear velocity and channel half-height, were between 100 and 400. A spectral channel code ,was used for all computations. A summary of various control schemes explored is given along with relevant publications, to which the interested reader is referred for detailed descriptions of each control algorithm. One of these control algorithms (a simple feedback law obtained from a neural network) was implemented into an M3 chip. Detailed descriptions of the M3 chip will be reported in the final report of the AFOSR/DARPA program mentioned above.

Advanced Concepts For Boundary Layer Control

F49620-96-1-0296

(June 15, 1996 – December 14, 1999)

Principal Investigator:

John Kim

Department of Mechanical and Aerospace Engineering
University of California, Los Angeles
Los Angeles, CA 90095-1597

Phone: 310-825-4393, 310-206-4830 (fax)
e-mail: jkim@seas.ucla.edu

1. Background and Objective

This research effort was conducted in close collaboration with an AFOSR/URI grant (F49620-93-1-0332, Integrated Microtransducer and Neural Network Systems for Distributed Control), an AFOSR/DARPA grant (F49620-97-1-0514, Distributed Turbulent Flow Control by MEMS Integrated with Neural Networks), and an AFOSR grant (F49620-95-1-0263, Advanced Concepts for Boundary Layer Control). The objectives of the first two programs were to develop a microsensor-microelectronics-microactuator (M^3) system on a chip, which can be used in real-time control for reducing the viscous drag in turbulent boundary layers. The third AFOSR grant mentioned above and the present grant were awarded to assist the design of microelectronics by developing new control strategies suitable for the M^3 system. Since the control logic must be included on a chip that contains multiple sensors and actuators, it was imperative to develop a simple control algorithm. Various different approaches, ranging from a nonlinear adaptive controller based on a neural network to a linear controller based on a linear systems theory, were explored by testing in numerical experiments.

2. Accomplishments

A series of numerical experiments were performed to explore new control strategies suitable for distributed control. All computations were conducted in two-dimensional channel geometry. The Reynolds numbers, based on the wall-shear velocity and channel half-height, were between 100 and 400. A spectral channel code was used for all computations. A summary of various control schemes explored is given below along with relevant publications, to which the interested reader is referred for detailed descriptions of each control algorithm. One of these control algorithms (a simple feedback law obtained from a neural network) was implemented into an M^3 chip. Detailed descriptions of the M^3 chip will be reported in the final report of the AFOSR/DARPA program mentioned above.

2.1 Neural Network

The first control scheme considered was an adaptive controller based on a neural network. Motivation of this work was a successful demonstration of drag reduction from the opposition control by Choi et al. (1993). The major drawback of the opposition control, however, is that it requires information inside the flow, rendering the approach impractical. A neural network was constructed and trained as an inverse model of a turbulent channel flow. The inverse model was used as an adaptive controller. A simple control network, which employs blowing and suction at the wall based only on the wall-shear stresses in the spanwise direction, was shown to reduce the skin friction by as much as 20% in direct numerical simulations of a turbulent channel flow. Also, a stable pattern was observed in the distribution of weights associated with the neural network. This allowed us to derive a simple control scheme that produced the same amount of drag reduction. This simple control scheme generates optimum wall blowing and suction proportional to a local sum of the wall-shear stress in the spanwise direction. The distribution of corresponding weights is simple and localized, thus making real implementation relatively easy. Further details on this work can be found in Lee et al. (1997), which is attached to this report as Appendix 1. We also used the

same control algorithm in the application of the Lorentz force to a boundary layer control, resulting in a substantial improvement over an open-loop control (Berger et al., 2000).

2.2 Suboptimal Control

In another approach exploring new control strategies, we developed a suboptimal control approach for a turbulent channel flow. Instead of searching for a global optimal condition, for which time iterations are required (and hence no practical importance), the suboptimal approach seek an optimal control within a short time horizon, thus avoiding time iterations. Two simple feedback laws for drag reduction were obtained. These new feedback control laws required pressure or shear-stress information at the wall. More practical control laws requiring only the local distribution of the wall pressure or one component of the wall shear stress were also derived and were shown to work equally well. Further details of his work can be found in Lee et al. (1998), which is attached to this report as Appendix 2. It is worth mentioning here that the final control algorithm obtained from this suboptimal control approach was very similar to that obtained from the neural network mentioned above. Both control schemes reduced the viscous drag by mitigating the strength of near-wall streamwise vortices, thus confirming our earlier premise that controlling near-wall streamwise vortices is a key to viscous drag reduction in turbulent boundary layers.

2.3 Systems Theory Approach

A third approach considered was a system theory approach to flow control. The main objective of this approach is to design a robust controller entirely based on the information of the system to be controlled rather than control designer's physical intuitions or prior knowledge of the system. This approach resulted in a feedback stabilization to delay the transition in a laminar channel flow to a reduction in viscous drag in a fully developed turbulent flow. This work demonstrated that although the system theory approach is based on a linear theory, it can be applied to fully nonlinear flows. Further details of this work can be found in Joshi et al. (1997), which is attached to this report as Appendix 3. In Lee et al. (2000), a reduced-order linear model was successfully applied to a turbulent channel flow, resulting in similar viscous drag reduction to that obtained by using a neural network as an adaptive controller mentioned earlier. Motivated by the success of the linear system theory approach, we also investigated a role of linear processes in fully nonlinear flows. It was found that a linear process plays an essential role in maintaining near-wall turbulence to the extent that without a particular linear process, turbulence could not be maintained in a turbulent channel flow. Further descriptions of this work can be found in Kim and Lim (2000), which is attached to this report as Appendix 4. We mention in passing that the present work has generated much interest in the application of control theories to flow problems in the control and fluid mechanics community as evidenced by several recent publications on the subject matter.

2.4 Microflap and Immersed-Boundary Method

All of the control algorithms mentioned above used surface blowing and suction as control input. Although such actuation is simple to implement in numerical experiments, precise control of blowing and suction in practice in the same manner as implemented in the numerical experiments is

difficult to achieve. In order to develop a control strategy for currently available actuators such as micro-flap actuators, development of a new numerical approach, known as an immersed-boundary approach, is currently underway. A brief description of the method is given below.

It was our desire to simulate flow over a complex boundary while retaining the simplicity and efficiency of computation in a Cartesian system. This was done through use of an immersed boundary method. The equations of fluid motion are calculated on the regular geometry of a periodic channel. Insertion of a microflap into the flow domain creates an internal boundary, which must be simulated properly. We used an idea of Peskin and McQueen (1989) of using a body force to represent the dynamical effect on the fluid of a moving wall immersed in the fluid. In their method, and our application, the position of the internal boundary within the flow domain does not generally coincide with the computational mesh. Flow properties are interpolated from the computational mesh to the locations of boundary nodes in order to calculate the force of the boundary on the fluid. Then that force is distributed onto nodes of the computational mesh near the internal boundary.

The force in Peskin and McQueen's work was based on a balance of tension in an elastic wall against the hydrodynamic forces. We instead used an idea developed by Mohd-Yusof (1997) of creating a fictitious force constructed so as to drive the velocity at desired locations to desired values. In Mohd-Yusof's application, the desired locations are a riblet surface and the desired values are zero to fulfill the no-slip condition. In our application, the desired locations are the flap positions and the desired values are the flap velocities, also to fulfill the no-slip condition. A difference between Mohd-Yusof's application and ours is the moving boundary created by the flap. Another difference is that the flap is an internal boundary with flow on both sides. Mohd-Yusof's riblet surface is an external boundary with only one side within the flow domain.

The Navier-Stokes equation with a forcing term is temporally discretized to yield,

$$\frac{\mathbf{u}^{n+1} - \mathbf{u}^n}{\Delta t} + \mathbf{u} \cdot \nabla \mathbf{u} = -\nabla p + \nu \nabla^2 \mathbf{u} + \mathbf{f}. \quad (1)$$

In a neighborhood of the flow boundary, we already know what we want the velocity to be at the end of the time step,

$$\mathbf{u}^{n+1} = \mathbf{w}, \quad (2)$$

so we solve for the body force that would bring that velocity about

$$\mathbf{f} = \frac{\mathbf{w} - \mathbf{u}^n}{\Delta t} + \mathbf{u} \cdot \nabla \mathbf{u} + \nabla p - \nu \nabla^2 \mathbf{u}. \quad (3)$$

The body force is applied at two sets of points, those just below the immersed boundary and those just above. Where the boundary coincides with the grid the body force is applied at the boundary and at the points just below it. Application of the force at additional points, particularly below the immersed boundary, was tested but found to give no benefit. Our method of applying the body

force gives flexibility in choosing the immersed boundary not found in some other methods, since there is no need to line up the boundary with a grid.

This simulation method has been useful for examining the interaction of the MEMS actuator with the fluid. Velocity data in the wind tunnel experiments was gathered at discrete stations downstream from the microflap. Data resolution is high in the spanwise and wall-normal directions, but not in the streamwise direction. The numerical simulations make data at any point in the flow available for interrogation. The ability to fill in the gaps of the wind tunnel data has helped explain the operation of the actuator. Wind tunnel data showed the flap causing fluid to move away from the wall at a velocity four times faster than the flap itself. There was some question as to whether this could be correct. The numerical simulation produced similar results and provided an explanation. Movement of the flap into higher speed fluid, combined with sucking fluid under the opening flap, created a shear layer, which would roll up into a vortex behind the flap and eject fluid away from the wall. This ejected fluid moved away from the wall much faster than deflection alone could produce. This observation is useful for a couple of reasons. First, it shows the mechanisms whereby the microflap can be most effective in influencing the flow. Second, it shows that a flap's actuation will be felt most strongly not at the flap itself, but instead a short distance downstream.

Laminar flow with a streamwise vortex passing over the flap was generated in the wind tunnel experiments. This was meant to be a simplified analog for the coherent structures found near the wall in a boundary layer. The vortex pulls high-speed fluid close to the wall and generates a high shear region at the wall. This is similar to the sweep events in turbulent boundary layers. The microflap actuator counteracts the action of the streamwise vortex and reduces shear at the wall in a region downstream from the flap. Our numerical simulations give results similar to those from the wind tunnel, thus adding further confidence in the immersed-boundary method in handling microflaps.

Qualitative comparisons between CFD and experimental results have been strong and encouraging. Quantitative comparisons are nearing completion, and when successfully completed will provide a strong validation of using our body force formulation as a model for the microflaps. When that work is completed, simulation efforts will turn to the interaction of arrays of microflaps with turbulent channel flows. This situation has not yet been investigated with physical experiments. Simpler flap models will also be compared and validated against the body force formulation.

Development of the immersed-boundary method for simulation of a turbulent flow with microflaps has not been completed yet. However, we believe that the immersed-boundary approach is an efficient and cost-effective approach to simulate turbulent flows involving complex geometry. We anticipate that the immersed-boundary method will emerge as a powerful tool for simulating many turbulent flows.

References:

Choi, H., Moin, P. and Kim, J., "Active turbulence control for drag reduction in wall-bounded flows," *Journal of Fluid Mechanics, J. Fluid Mech.*, **262**, 1994.

Joshi, S., Speyer, J. and Kim, J., "A systems theory approach to the feedback stabilization of infinitesimal and finite-amplitude disturbances in plane Poiseuille flow," *J. Fluid Mech.*, **332**, 1997.

Kim, J. and Lim, J., "A linear process in wall-bounded turbulent shear flows," *Phys. Fluids*, **12**, 2000.

Lee, C., Kim, J., Babcock, D. and Goodman, R., "Application of neural networks to turbulence control for drag reduction," *Phys. Fluids*, **9** (6), 1997.

Lee, C., Kim, J. and Choi, H., "Suboptimal control of turbulent channel flow for drag reduction," *J. Fluid Mech.*, **358**, 1998.

Lee, K., Cortelezzi, L., Kim, J. and Speyer, J., "Application of robust reduced-order controller to turbulent flows for drag reduction," submitted for publication, 2000.

3. Honors

NASA Medal for Exceptional Scientific Achievement (1985)

Fellow of APS (1989)

Rockwell International Endowed Chair (1993)

H. Julian Allen Award from NASA Ames Research Center (1994)

Editor of Physics of Fluids (1998-)

4. Personnel Supported

Sanjay Joshi (Graduate Student), Ph.D. awarded

David Babcock (Graduate Student), Ph.D awarded

Tim Berger (Graduate Student)

5. List of Publications

Berger, T., Kim, J., Lee, C. and Lim, J., "Turbulent boundary layer control utilizing the Lorentz force," *Phys. Fluids*, **12**, 2000.

Joshi, S., Speyer, J. and Kim, J. "A systems theory approach to the feedback stabilization of infinitesimal and finite-amplitude disturbances in plane Poiseuille flow," *J. Fluid Mech.*, **332**, 1997.

Kim, J. and Lim, J., "A linear process in wall-bounded turbulent shear flows," *Phys. Fluids*, **12**, 2000.

Kim, J., "Active control of turbulent boundary layers for drag reduction," IUTAM Symposium on Mechanics of Passive and Active Flow Control (eds. Meier and Viswanath), Kluwer Academic Publishers, 1999.

Lee, C., Kim, J., Babcock, D. and Goodman, R., "Application of neural networks to turbulence control for drag reduction," *Phys. Fluids*, **9** (6), 1997.

Lee, C., Kim, J. and Choi, H., "Suboptimal control of turbulent channel flow for drag reduction," *J. Fluid Mech.*, **358**, 1998.

Tsao, T., F. Jiang, C. Liu, R. Miller, S. Tung, J. Huang, B. Gupta, D. Babcock, C. Lee, Y. Tai, C. Ho, J. Kim and R. Goodman, "MEMS-based active drag reduction in turbulent boundary layers," *Microengineering Aerospace Systems* (ed. H. Helvajian), The Aerospace Press, 1999.

6. Patents

None

7. Transitions

A control logic based on a neural network was implemented into a final design of the M³-chip.

Appendix 1

Application of neural networks to turbulence control for drag reduction

Changhoon Lee and John Kim^{a)}

Department of Mechanical and Aerospace Engineering, University of California at Los Angeles,
Los Angeles, California 90095-1597

David Babcock and Rodney Goodman

Department of Electrical Engineering, California Institute of Technology, Pasadena, California 91125

(Received 16 September 1996; accepted 24 February 1997)

A new adaptive controller based on a neural network was constructed and applied to turbulent channel flow for drag reduction. A simple control network, which employs blowing and suction at the wall based only on the wall-shear stresses in the spanwise direction, was shown to reduce the skin friction by as much as 20% in direct numerical simulations of a low-Reynolds number turbulent channel flow. Also, a stable pattern was observed in the distribution of weights associated with the neural network. This allowed us to derive a simple control scheme that produced the same amount of drag reduction. This simple control scheme generates optimum wall blowing and suction proportional to a local sum of the wall-shear stress in the spanwise direction. The distribution of corresponding weights is simple and localized, thus making real implementation relatively easy. Turbulence characteristics and relevant practical issues are also discussed. © 1997 American Institute of Physics. [S1070-6631(97)02706-2]

I. INTRODUCTION

The ability to control turbulent flows is of significant economic interest. Successful control of turbulent boundary layers by reducing drag, for example, can result in a substantial reduction in operational cost for commercial aircraft and marine vehicles. Recent studies^{1,2} show that near-wall streamwise vortices are responsible for high skin-friction drag in turbulent boundary layers. Some attempts have been made to reduce the skin-friction drag by controlling the interactions between these vortices and the wall. Choi *et al.*,² for example, used blowing and suction at the wall equal and opposite to the wall-normal component of velocity at $y^+ = 10$. They showed that this control effectively mitigated the streamwise vortices, giving approximately 25% drag reduction in a turbulent channel flow. Although the method employed in their work is impractical, since the information at $y^+ = 10$ is usually not available, it demonstrates a control scheme which reduces skin-friction drag by manipulation of the near-wall streamwise vortices. Another way to control the streamwise vortices is to impose spanwise oscillation by a moving wall or externally imposed body force.^{3,4} These methods, however, require a large amount of energy input.

A systematic approach using suboptimal control theory has also been tried in the past. This approach, which attempts to minimize a cost function, was successfully applied to the stochastic Burgers equation.⁵ Moin and Bewley⁶ applied a similar approach to a turbulent channel flow to achieve up to 50% drag reduction. The control, however, requires information from the entire velocity field inside the flow domain and excessive computational time, making it impractical to implement in real situations. For practical implementation, a control scheme should utilize only quantities that are easily

measurable at the wall, and should be fast enough to be applied in real time.

The objective of the present work is to seek wall actuations, in the form of blowing and suction at the wall, dependent on the wall-shear stress to achieve a substantial skin-friction reduction. This requires knowledge of how the wall-shear stresses respond to wall actuations, i.e., the correlation between the wall-shear stresses and the wall actuations. Because of the complexity of the solutions to the Navier-Stokes equations, however, it is not possible to find such a correlation in closed form or to approximate it in simple form. Instead, we use a neural network to approximate the correlation which then predicts the optimal wall actuations to achieve the minimum value of the skin-friction drag. Neural networks have been used to obtain complicated, nonlinear correlations without *a priori* knowledge of the system that is to be controlled. Jacobson and Reynolds,⁷ for instance, used a neural network to obtain about 7% drag reduction in their simulation of an artificial flow. In this paper, we describe how we constructed and trained a neural network off-line, and then implemented an on-line control scheme (blowing and suction at the wall) for drag reduction based on that neural network. Applying this control scheme to direct numerical simulations of turbulent channel flow at low Reynolds number, we observed about 20% drag reduction. We then describe how examination of the weight distribution from the on-line neural network led to a very simple control scheme that worked equally well while being computationally more efficient.

In Sec. II, a brief description of the architecture of the neural network used in the present work is given. In Sec. III, results obtained from control using an off-line trained network are presented, while results obtained from control using a network with continuous on-line training are given in Sec. IV. In Sec. V, a simple control law based on the weight distribution from the successful neural network control is presented. A few turbulence statistics are given in Sec. VI,

^{a)}Corresponding author. Telephone: (310)825-4393; Fax: (310)206-4830;
Electronic mail: jkim@turb.seas.ucla.edu

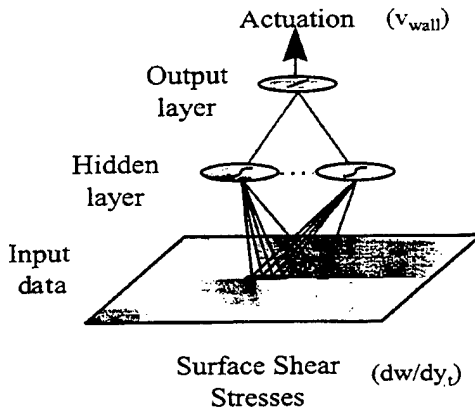


FIG. 1. Neural network architecture.

followed in Sec. VII by a discussion of practical implementation and the conclusions.

In this paper we use (x, y, z) for the streamwise, wall-normal, and spanwise coordinates, respectively, and (u, v, w) for the corresponding velocity components.

II. NEURAL NETWORK

In this section we describe the construction of a neural network to learn the correlation between wall-shear stresses and wall actuations from a given data set. Although a neural network generally requires no prior knowledge of the system (or “plant”), knowledge about the near-wall turbulence structures provides a guideline for the design of the network architecture. Initially $\partial u / \partial y$ and $\partial w / \partial y$ at the wall at several instances of time were used as input data fields and the actuation at the wall was used for the output data of the network. Experimentally we found that only $\partial w / \partial y$ at the wall from the current instance of time was necessary for sufficient network performance. Because we wanted the output to be based only on a local input area, we designed our network using shared weights. The network had a single set of weights (a template) that is convolved over the entire input space to generate output values; that is, we used the same set of weights for each data point and the training involves iterating over all data points. The template extracts spatially invariant correlations between input and output data. The size of the template was initially chosen to include information about a single streak and streamwise vortex, and then was varied to find an optimal size.

We used a standard two-layer feedforward network with hyperbolic tangent hidden units and a linear output unit (see Fig. 1). The functional form of our final neural network is

$$v_{jk} = W_a \tanh \left(\sum_{i=-(N-1)/2}^{(N-1)/2} W_i \frac{\partial w}{\partial y} \Big|_{j,k+i} - W_b \right) - W_c, \quad (1)$$

$$1 \leq j \leq N_x, \quad 1 \leq k \leq N_z,$$

where the W 's denote weights, N is the total number of input weights, and the subscripts j and k denote the numerical grid point at the wall in the streamwise and spanwise directions respectively. N_x and N_z are the number of computational

domain grid points in each direction. The summation is done over the spanwise direction. Seven neighboring points ($N=7$), including the point of interest, in the spanwise direction (corresponding to approximately 90 wall units with our numerical resolution) were found to provide enough information to adequately train and control the near-wall structures responsible for the high-skin friction. Note that the blowing and suction are applied at each grid location according to (1) as a numerical approximation of distributed blowing and suction on the surface. A scaled conjugate gradient learning algorithm⁸ was used to produce rapid training. For given pairs of $(v_{jk}^{\text{des}}, \partial w / \partial y|_{jk})$, network was trained to minimize the sum of a weighted-squared error given by

$$\text{error} = \frac{1}{2} \sum_j \sum_k e^{\lambda |v_{jk}^{\text{des}}|} (v_{jk}^{\text{des}} - v_{jk}^{\text{net}})^2, \quad (2)$$

where v^{des} is the desired output value and v^{net} is the network output value given by Eq. (1). The weights were initialized with a set of random numbers. Note that the error defined in (2) exponentially emphasizes (proportional to λ) large actuations. This error scaling was chosen based on Choi *et al.*'s² observation that large actuations are more important for drag reduction. Usually within 100 training epochs, the error reached its asymptotic limit.

III. OFF-LINE TRAINING AND CONTROL

As an initial experiment we investigated whether we could train a neural network to predict the velocity at $y^+ = 10$ from only the wall-shear stresses. The rationale behind this experiment was to duplicate an existing control law using only measurements available at the wall such that the output from the network could be used as input to the actuator. The network should yield a similar amount of drag reduction to that obtained by Choi *et al.*² through prediction of the velocity at $y^+ = 10$. The training data consisted of 100 time steps of output obtained from a numerical simulation of channel flow under the control employed by Choi *et al.*,² i.e., using the wall-normal velocity at $y^+ = 10$. The flow regime is turbulent channel flow with $Re_\tau = 100$, where Re_τ is the Reynolds number based on the wall-shear velocity, u_τ , and the channel half-width, δ . All numerical simulations presented in this paper were obtained using a modified version of Kim *et al.*'s⁹ spectral code with the computational domain $(4\pi, 2, 4\pi/3)\delta$, and a grid resolution of $(32, 65, 32)$ in the (x, y, z) directions, respectively. Each time step contained a 32×32 array of input values $(\partial w / \partial y|_w)$ and corresponding actuations, $-v$ at $y^+ = 10$.

We trained several networks with one hidden unit and different sized input templates: 7×1 , 7×3 , 7×5 , 9×1 , 9×3 , 11×1 , and 11×3 (the number of input points in the spanwise direction by the number of input points in the streamwise direction). After training was completed, the distribution of input weights was examined to see whether there was a discernible pattern in the input template. The weight distributions in the spanwise direction at the same streamwise location for different input templates are shown in Fig. 2. The same pattern for all 7 input template sizes was observed, and is similar to a finite difference approximation of

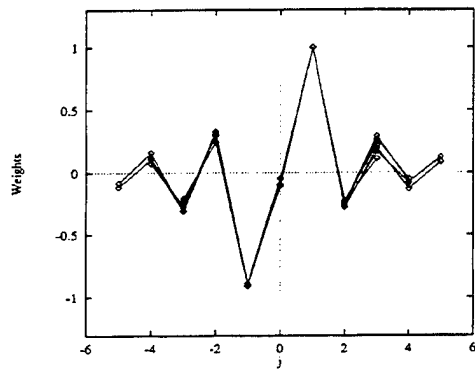


FIG. 2. Weight distribution from off-line trainings for various sizes of the input template: $7 \times 1, 7 \times 3, 7 \times 5, 9 \times 1, 9 \times 3, 11 \times 1, 11 \times 3$. Weights are normalized by W_1 .

spanwise differentiation. Increasing the number of hidden units only marginally improved performance, whereas increasing the template size significantly reduced the final training error.

We then applied a control scheme to a regular channel flow by fixing the final input weights obtained from the off-line training. This was perhaps a somewhat naive approach since the weights were obtained from fully controlled flow data and the shear stresses used for the training were already altered by the actuations. Nevertheless, two cases were tested: a control scheme based on 7 weights in the spanwise direction, and another based on the same 7 weights plus 3 more in the immediate downstream location. These 10 weights were chosen because among all weights obtained from the off-line training they had non-negligible values. In Fig. 3, the mean shear stress variations at the wall (i.e., drag) obtained with these two controls are plotted along with the no-control case. Nearly 18% drag reduction was achieved, with slightly better performance from the 10-weight network.

These results demonstrate that a correlation exists between the shear stresses at the wall and the desired actua-

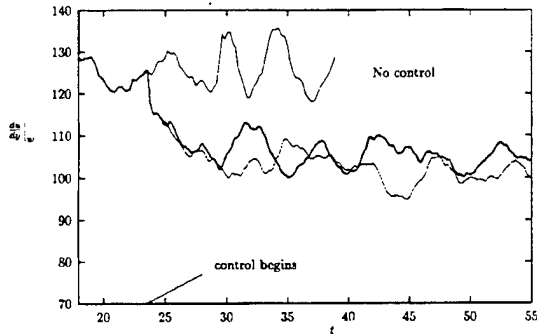


FIG. 3. Mean wall-shear stress histories for various control laws compared to the no-control case: —, no control; —, control with 7 fixed weights obtained from off-line control; ···, control with 10 fixed weights from the same off-line control. All runs with control shown in this paper were integrated over at least 20 time units that is much longer than the typical turn-over time of the streamwise vortices, 1 time unit.

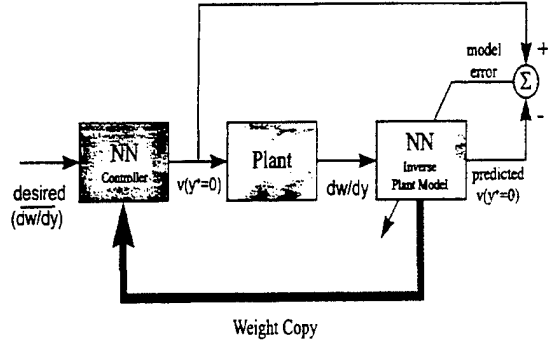


FIG. 4. Schematic representation of adaptive inverse model control.

tions, and that control based on this correlation produces a significant amount of drag reduction. This fixed-weight control scheme, however, was deduced from fully controlled flow data; thus it does not guarantee the same performance for other flow situations.

IV. ON-LINE CONTROL

In the previous section we showed how successful control based on off-line training can be obtained. However, since the system we are trying to control is time-varying and nonlinear, this approach is not likely to generalize well. Continuous on-line training allows a controller to adapt to the evolution of the system. In this section, we describe an adaptive controller for on-line training and control.

There are various schemes for on-line neural network control. The most direct scheme is adaptive-inverse model control.¹⁰ A schematic representation of this approach is shown in Fig. 4. Here the plant denotes the numerical solver of the Navier-Stokes equations. This configuration employs a neural network to model the (possibly time-varying) inverse plant mapping from wall-shear stress $\partial w / \partial y|_w$ to the wall-normal actuations, and then uses a copy of the model as the controller with the desired shear stresses as input. One restriction of this technique is that it usually requires an initial model training phase using random plant inputs and corresponding plant outputs. This, however, caused no serious problems since usually one time step was enough for model training because of the shared-weight architecture in our application (each time step is 1024 data points and our networks only have a few weights). Once the model represents a reasonably close approximation to the actual plant inverse, a copy is then implemented as a feedforward controller.

The desired inputs to the controller are a fractional reduction in the shear stress from the previous step, i.e.,

$$\left(\frac{\partial w}{\partial y} \right)_{t+\Delta t}^{\text{des}} = \eta \left(\frac{\partial w}{\partial y} \right)_t, \quad (3)$$

where $0 < \eta < 1$. Based on the networks and techniques we investigated, this indirect suppression of $\partial w / \partial y|_w$, instead of $\partial u / \partial y|_w$, turns out to be more efficient in achieving drag reduction. The output of the controller, which is the input to the plant, is the predicted actuation necessary to produce this shear-stress reduction. The quantity η should be chosen such

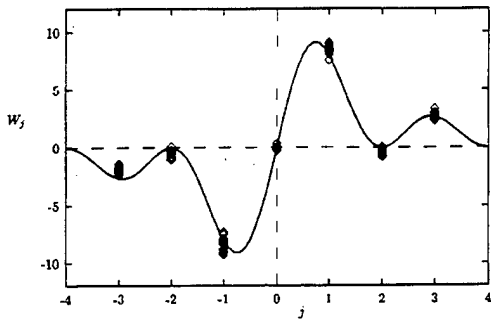


FIG. 5. Distribution of the weights: \diamond , from on-line training; —, $A(1-\cos(\pi j))/j$. $\Delta z^+ = 13$.

that sets of the desired large amplitude outputs are among the sets that are well represented by the training sets. Good performance was achieved for the range of $\eta = 0.8-0.85$.

A turbulent channel flow at Reynolds number $Re_\tau = 100$ was used to test the neural network. We allowed all the weights in the network to adapt and examined the input template pattern after each time step. As the control began, the weight distribution immediately assumed a fixed pattern similar to the off-line pattern. There was no appreciable change in the relative magnitudes of the template weights over time, indicating that the pattern is preserved. The absolute magnitudes, however, did vary indicating the need for gain and bias adaptation for each layer. The number of hidden layers, the number of the hidden units, the size of the input template, and the error scale of the training error [λ of Eq. (2)] were 1, 1, 7×1 , and 5, respectively. We varied the values of the error scale and found 5 to be optimum, with larger values causing an instability in training. We also varied the number of the hidden units, but the network with a single hidden unit produced the best result. The converged weight distributions for 20 consecutive time steps after an asymptotic state was reached are shown in Fig. 5. The pattern is only slightly different from the one obtained from the off-line training (see Fig. 2). It should be noted that this pattern emerged immediately after the on-line control began.

Time histories of the wall-shear stress for 3 different input template sizes are shown in Fig. 6. All other network parameters are kept the same. The abscissa represents non-dimensional time normalized by u_τ and δ . One time unit roughly corresponds to the time for a fluid particle traveling with the centerline velocity to move about 20 channel half widths. The computations were carried out long enough to ensure that a statistically steady state was reached. As the control began, the drag quickly drops to about 80% of that observed without control, for the two cases with template sizes of 7×1 and 9×1 . The template size of 5×1 , however, did not produce as much reduction, indicating that at least 7 spanwise points (which extended about 90 wall units, with our grid resolution) should be used for good performance. At the initial stage of our study, we tested a control using both $\partial w/\partial y|_w$ and $\partial u/\partial y|_w$ as input, with a 7×5 input template. It produced about the same amount of reduction, but with excessive training time due to a significantly larger number

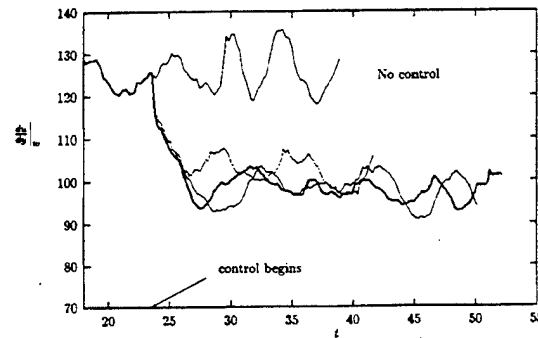


FIG. 6. Mean wall-shear stress histories for on-line control with different input template sizes: —, no control; ···, control with 5×1 ; -·-, control with 7×1 ; —, control with 9×1 .

of weights. Furthermore, it did not produce coherent patterns in the weight distributions.

Since the 7 weights showed a fixed pattern, we fixed the input template weights to this pattern and used a single hidden unit network, giving only 4 adaptable parameters (a bias and gain for each layer). This simplified network had the following functional form:

$$v_{jk} = W_a \tanh(W_b g - W_c) - W_d \quad (4)$$

with

$$g = \sum_{i=-3}^3 W_i \frac{\partial w}{\partial y} \Big|_{j,k+i}, \quad (5)$$

where W_i 's are the fixed-weight pattern obtained from the previous on-line control. On-line control using this network produced a similar amount of drag reduction. The weight variations with time were also monitored. The bias weights (W_c and W_d) were negligibly small. Those controlling the gain (W_a and W_b), which had finite values, changed in time significantly, although the product of the two gain-weights remained almost constant. This suggests that effective control can be achieved by simply using g with an adjustable amplitude. This will be discussed in the following section.

V. A SIMPLE CONTROL SCHEME

Since the control based on the network given by Eq. (4) produced a substantial reduction in drag, this section develops a control scheme based only on the weighted sum of the wall-shear stress. The distribution of the weights can be approximated by (see Fig. 5):

$$W_j = A \frac{1 - \cos(\pi j)}{j}, \quad (6)$$

where $j=0$ corresponds to the point where the control is applied. Since only the relative values are important, the constant A has no special meaning. A computation with a twice higher resolution was run to confirm that Eq. (6) gives the proper form of the weight distribution (see Fig. 7). It turns out that Eq. (6) is the inverse Fourier transform of $ik_z/|k_z|$, where k_z is the wave number in the spanwise direction, for the finite maximum wave number, i.e.,

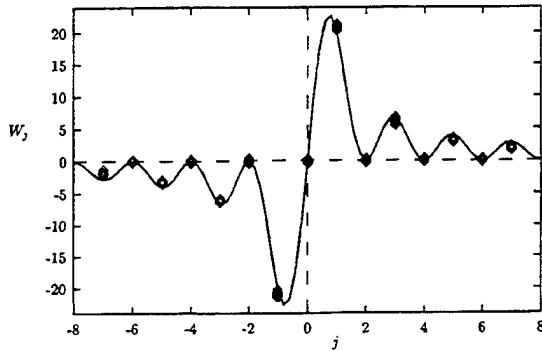


FIG. 7. Distribution of the weights: \diamond , from on-line training; —, $A(1 - \cos(\pi j))/j$. $\Delta z^+ = 6$.

$$\int_{-k_m}^{k_m} \frac{ik_z}{|k_z|} \exp(-ik_z z) dk_z = 2 \frac{1 - \cos(k_m z)}{z}, \quad (7)$$

where $k_m = \pi/\Delta z$ is the maximum wave number and Δz is the numerical grid spacing. Replacing z with $j\Delta z$ in the right-hand-side of Eq. (7) leads to Eq. (6). From this result and the convolution theorem, one can suggest the following simple control law for wall transpiration:

$$\hat{v}_w = C \frac{ik_z}{|k_z|} \left. \frac{\partial w}{\partial y} \right|_w = C \frac{1}{|k_z|} \frac{\partial}{\partial z} \left(\frac{\partial \hat{w}}{\partial y} \right), \quad (8)$$

where the “hat” denotes a Fourier transformed quantity and C is a positive scale factor determining the amplitude of the actuation. Equation (8), which should produce similar drag reduction as the result with 7 fixed weights [Eq. (4)], implies that the optimum blowing and suction at the wall is proportional to $\partial(\partial w/\partial y)/\partial z$ with the high wave number component suppressed by $1/|k_z|$. Note that the wall-normal actuation proportional to $\partial(\partial w/\partial y)/\partial z$ counteracts the up-and-down motion induced by a streamwise vortex (see Fig. 8), consistent with that used by Choi *et al.*² Smith *et al.*¹¹ discussed the stability of the near-wall turbulence structure to a local adverse pressure gradient imposed near the surface.

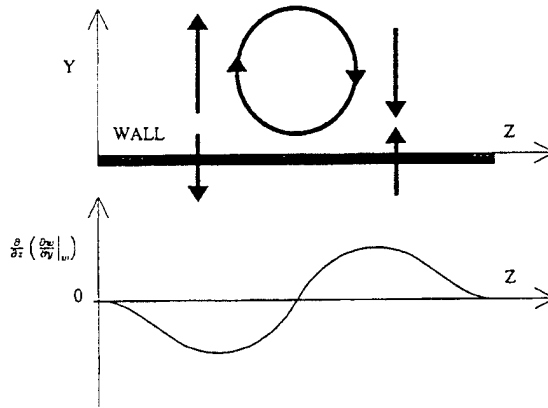


FIG. 8. A schematic of a flow field induced by a streamwise vortex and corresponding $\partial(\partial w/\partial y)|_w / \partial z$.

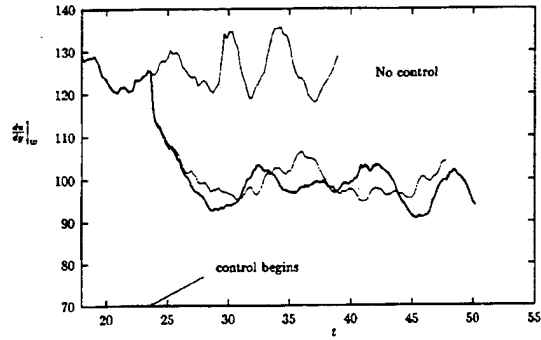


FIG. 9. Mean wall-shear stress histories for various control schemes compared to the no-control case: —, no control; —, on-line control with neural network with 7×1 template; ···, control with 7 fixed weights.

The suction at the left side of the vortex in Fig. 8 can relieve such adverse pressure gradient, thus preventing the surface-layer eruption. Choi *et al.*² reported that actuation based only on the local value of $\partial(\partial w/\partial y)/\partial z$, which is also a dominant term of the Taylor expansion of v at some distance away from the wall, did not produce such a substantial drag reduction. This indicates that suppression of high wave number components by $1/|k_z|$, or equivalently using locally weighted value of $\partial w/\partial y$, plays a key role in reducing drag. Note that the weights at even numbered grid points away from the center point vanish. This is beneficial for physical implementation, since sensors and actuators cannot be placed at the same location.¹² Because the Fourier integral is computed for a finite value of k_m , the values of the weight at noninteger j in Eq. (6) have no meaning. Equation (8) is equivalent to

$$v_{jk} = C \sum_{i=-(N-1)/2}^{(N-1)/2} W_i \left. \frac{\partial w}{\partial y} \right|_{j,k+i}, \quad (9)$$

where W_i is given by Eq. (6). The magnitude of the weights decays with increasing distance from the center, which allows for good approximation using only a small number of weights, i.e., successful control requires only local values of the shear stress. A natural concern is how different grid spacings affect the control. Since the above control law [Eq. (9)] is simply another expression of Eq. (8), which is a good approximation as long as k_m is large enough, the control should be relatively independent of resolution. This was confirmed by a computation with a higher resolution.

Control based on Eq. (9) with 7 points produced the same amount of drag reduction (20%) as the neural network control (see Fig. 9). The constant C is chosen so that the root-mean-squared (rms) value of the actuation is kept at $0.15u_\tau$. Blowing and suction of this magnitude at the wall suppress the near-wall streamwise vortices by counteracting the up-and-down motions associated with these vortices (see Fig. 8).

The fact that a control scheme that is essentially linear [Eq. (9)] produced the same amount of drag reduction as on-line control with a nonlinear network led to the following question: Can the same weight pattern be captured when on-line control with a “linear” network is used? To answer

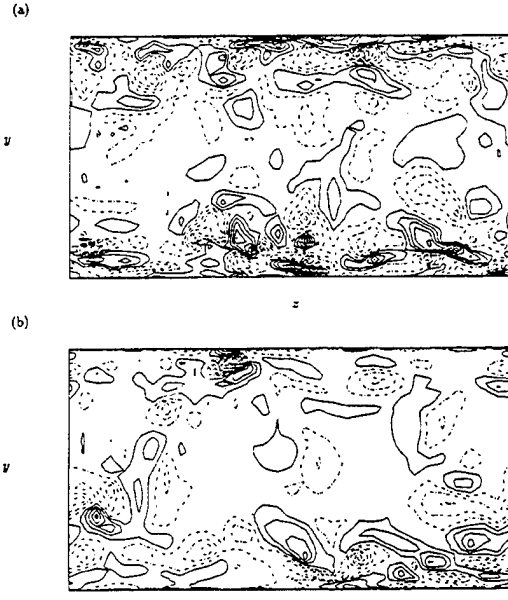


FIG. 10. Contours of streamwise vorticity in a cross-flow plane: (a) no control; (b) control using 7 fixed weights. The contour level increment is the same for both figures. Negative contours are chain-dotted.

this question, we tested an on-line controller utilizing a linear network. The hyperbolic tangent function in Eq. (1) was replaced with a linear function and the hidden layer was removed. All other parameters were kept the same as the nonlinear network case. The linear network seemed to produce almost the same pattern in weights as the one produced by our nonlinear network. Also, drag was reduced by the same amount. The pattern that was obtained by averaging over time, however, was not well preserved in time. The weight W_3 of Eq. (1), for example, frequently showed order of magnitude excursions resulting in a large standard deviation, 1.5, compared to the value of the weight, 0.3 (weights were normalized by the maximum amplitude W_1). The nonlinear network, however, produced more constant weights; the standard deviation of W_3 was only 0.15. This result indicates that the nonlinearity should add robustness by bounding the weights. This can simplify hardware implementation by limiting the signals and subsequently the necessary dynamic range of the processing circuitry.

VI. TURBULENCE STATISTICS

The computed flow fields for a no-control case and a successful control case, based on the 7-point weighted sum of $\partial w / \partial y|_w$ [Eq. (9)], were examined to investigate the mechanism by which the drag reduction is achieved. The most salient feature of the controlled case was that the strength of the near-wall streamwise vortices was drastically reduced. In Fig. 10, contours of streamwise vorticity in a cross plane are shown. This result further substantiates the notion that a successful suppression of the near-wall stream-

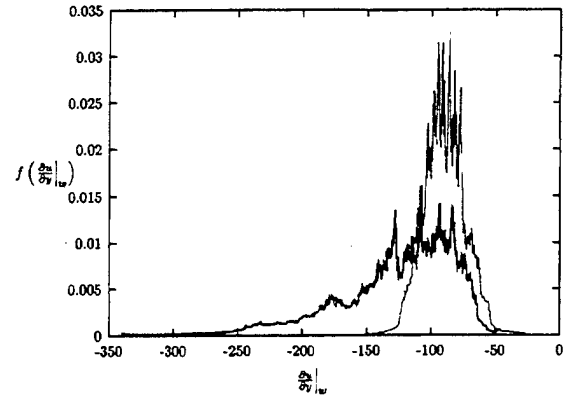


FIG. 11. Probability-density function of the wall-shear stress: —, no control; —, control with 7 fixed weights. The area under each curve is normalized to one.

wise vortices leads to a significant reduction in drag. Note that for the controlled case the wall actuations were applied at both walls.

The probability-density function of the wall-shear stress in the streamwise direction is shown in Fig. 11. It is evident that the control is very effective in suppressing large fluctuations, thus reducing the mean-skin friction. Furthermore, the root-mean-square (rms) values of turbulent fluctuations in the wall region are also reduced as shown in Fig. 12(a). The same trend was observed by Choi *et al.*² The rms vorticity fluctuations are also significantly reduced, except for ω_x very

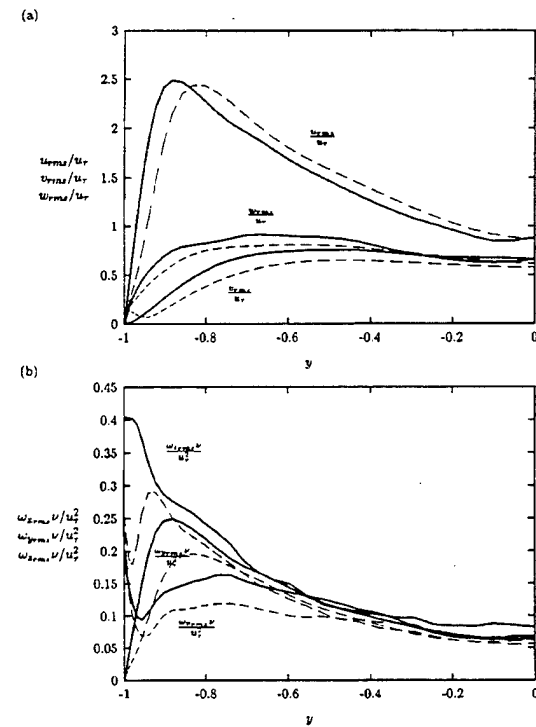


FIG. 12. Root-mean-square fluctuations normalized by the wall variables: —, no control; ···, control with 7 fixed weights. (a) Velocity fluctuations; (b) vorticity fluctuations.

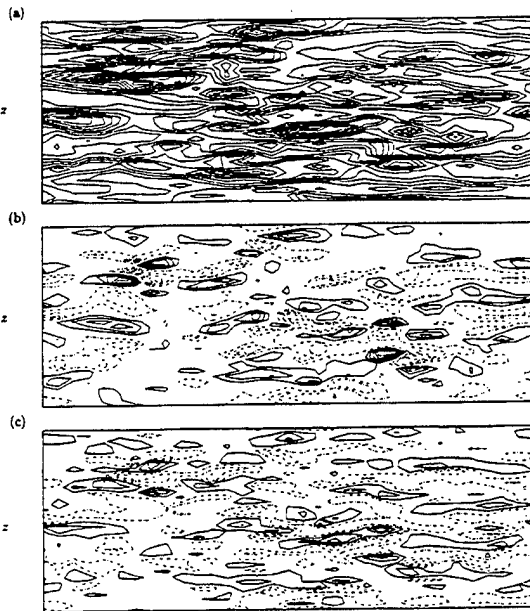


FIG. 13. Contours of the wall actuation: (a) control using $\partial w / \partial y|_w$ with 7 fixed weights; (b) control using information at $y^+ = 10$. Negative contours are chain-dotted.

close to the wall. The increase for the latter is caused by additional $\partial v / \partial z$ due to the wall actuation. The rms fluctuations of ω_z at the wall, which is mainly due to $\partial u / \partial y$ at the wall, is also decreased. This indicates that the control scheme led to a reduction in the mean shear and its variance at the wall by suppressing large fluctuations as shown in Fig. 11. The reduction in the rms fluctuations in ω_x and ω_y indicates that the control scheme indeed reduced the strength of the near-wall streamwise vortices and the wall-layer streaks.

Figure 13 compares the distribution of wall actuation used in our control with that from Choi *et al.*'s² v -control using the information at $y^+ = 10$ for the same wall-shear stress distribution. The corresponding wall-shear stress distribution is also shown in Fig. 13. The wall actuations indicate a strikingly similar distribution to each other, even though the wall actuation of our control is based only on the wall-shear stress $\partial w / \partial y|_w$. Basically our control scheme detects edges of locally high-shear stress regions by measuring the spanwise variation of $\partial w / \partial y$, and applies appropriate wall actuation as shown in Figs. 13(a) and 13(b). Since high-shear stress regions are usually elongated in the streamwise direction, only spanwise variation is necessary for detecting the edges. Since $\partial w / \partial y$ is a direct measurement of streamwise vortices (see Fig. 8), it provides more appropriate information than $\partial u / \partial y$. This is consistent with our finding that $\partial w / \partial y$ at several points in spanwise direction are enough for good performance of control.

VII. DISCUSSION AND CONCLUSION

We have presented a successful application of a neural network to turbulence control for drag reduction. First we

were able to construct and train a neural network off-line to find a correlation between the wall-shear stress and the desired wall actuations coming from the information at $y^+ = 10$. Based on the optimal network structure from the off-line training, we successfully implemented an on-line inverse model controller in numerical experiments of a turbulent channel flow, resulting in about 20% drag reduction. Finally, we were able to deduce a simple control scheme [Eq. (9)] for drag reduction based on observation of the weight distribution from a successful control case. This control scheme uses a minimal amount of wall-shear stress information and requires only simple operations, thus rendering a scheme whose actual hardware implementation would be relatively easy.

Beginning with a nonlinear network, we found a simple linear control scheme from the pattern of the weights, suggesting the use of a linear network. Although a linear network produced a similar pattern, the pattern was not well preserved in time. The weights can vary significantly increasing the difficulty in circuit implementation due to the larger required dynamic range. The nonlinear network, however, produced bounded weights simplifying hardware implementation. This suggests that a certain amount of nonlinearity is beneficial to capture a stable coherent pattern for our system.

Although the present control scheme is a significant improvement over earlier approaches that require velocity information within the flow, there is a technical issue before the present control scheme can be implemented in real practice. Precise control of blowing and suction distributed over a surface is difficult to implement. Other approaches, such as surface movements by deformable surface, may prove to be more practical.

There are also several fundamental issues that must be addressed. First, our numerical experiments were performed in a very low Reynolds number flow. It remains to be seen whether the same control scheme extends to higher Reynolds numbers. If the main cause of high-skin friction in turbulent boundary layers at higher Reynolds numbers is also due to the near-wall streamwise vortices, the same scheme should work equally well. Detection of these vortices through the wall-shear stress would become more difficult, however, because the scales associated with these vortices decrease as the Reynolds number increases.

Another important issue is the influence of the spatial resolution of sensors and actuators on performance. We showed that a simple control scheme with 4 neighboring points in the spanwise direction (3 among 7 weights are zeros), which span 90 wall units, performed very well. This suggests that the distance between sensors should be about 20 wall units. As the Reynolds number increases, the physical separation between sensors must decrease. We note in passing that recent advances in micromachined sensors and actuators make these scales feasible,¹³ and the present work is part of a joint research project aimed at integrating micron-sized sensors and actuators with analog VLSI control circuitry.

A third issue is determining an appropriate scale factor C in Eq. (9). We tested a range of C and empirically found

that values yielding an actuation rms value between $0.1\mu_r$ and $0.15\mu_r$ gave the best performance. Smaller values resulted in less reduction, while larger ones caused rapid fluctuations of the wall-shear stress over time. The experiments were only performed for $Re_r=100$ and 180, from which the optimum value was deduced, but we expect that the same amplitude level should produce similar reductions for higher Reynolds number flows. We further note that for this amplitude the required power input per unit area to produce the actuation, $p_w v_w + 0.5\rho v_w^3 (\sim 0.1\rho u_r^3)$ was significantly less compared to the power saved due to the reduced drag, $\Delta C_f/C_f \cdot \tau_w U_c (\sim 3.5\rho u_r^3)$ for 20% reduction in C_f . Here p_w , ρ , C_f , τ_w and U_c are the wall pressure, density, friction coefficient, averaged wall-shear stress in the streamwise direction, and centerline velocity, respectively. Note that we did not account for device loss to deliver blowing and suction nor the power consumed by sensors in this estimate.

One final practical issue worth mentioning is the time delay between sensing and actuation. None was included in any of our numerical experiments. In a real situation, however, there will be a finite time delay between sensing and actuation. The process time for the simple control scheme should be negligible since a weighted summation is an involved process, thus not imposing any restriction on the time delay. Ideally, sensors should register the response of the near-wall structures to be controlled due to wall actuations, which will take a certain amount of time. Blowing and suction at the wall, however, can produce an immediate spurious response at nearby sensors due to local conservation. One possible remedy to this problem is an under-relaxation of the actuation signal with past signals, accounting for the response of a longer time scale. For example, an underrelaxation scheme using the following formula

$$v_{jk}^{t+\Delta t} = \xi C \sum_i W_i \frac{\partial w}{\partial y} \Big|_{j,k+i} + (1 - \xi) v_{jk}^t \quad (10)$$

could take into account all past signals with a single parameter ξ ($0 < \xi < 1$). We used this approach successfully in our numerical experiment for $Re_r=180$ and found that there is an optimum ξ depending on temporal resolution.

The most significant finding of the present study is that a single spanwise strip of $\partial w / \partial y|_w$ is enough to achieve significant drag reduction. Additional information about $\partial w / \partial y|_w$ in the streamwise direction or $\partial u / \partial y|_w$ in either direction reduced the efficiency of our neural-network based control. We also tested different-sized input templates and found that as the template size increased in the streamwise direction, the training time became excessive and the fixed pattern in the weight disappeared, indicating that too many unnecessary weights caused training problems.

ACKNOWLEDGMENTS

We are grateful to Dr. Gary Coleman for comments on a draft of this paper and Tim Berger for preparation of Figs. 10 and 13. We also are grateful to a referee for suggestion about the linear network. This work is supported by AFOSR Grants Nos. F49620-93-1-0332 and F49620-95-1-0263 (Dr. James M. McMichael, Program Manager). It is also supported in part by the Center for Neuromorphic Systems Engineering as a part of the National Science Foundation Engineering Research Center Program under Grant No. EEC-9402726. Computer time has been supplied by the San Diego Supercomputer Center, NASA Ames Research Center and by the NAS program at NASA Ames Research Center.

- ¹J. Kim, "Study of turbulence structure through numerical simulations: The perspective of drag reduction," AGARD Report No. R-786, AGARD FDP/VKI Special Course on "Skin Friction Drag Reduction," 2-6 March 1992, VKI, Brussels (1992).
- ²H. Choi, P. Moin, and J. Kim, "Active turbulence control for drag reduction in wall-bounded flows," *J. Fluid Mech.* **262**, 75 (1994).
- ³R. Akhavan, W. J. Jung, and N. Mangiacavalli, "Turbulence control in wall-bounded flows by spanwise oscillations," *Appl. Sci. Res.* **51**, 299 (1993).
- ⁴J. Kim, C. Lee, T. Berger, J. Lim, and H. Choi, "Effects of electromagnetic force on near-wall turbulence," *Bull. Am. Phys. Soc.* **40**, 1989 (1995).
- ⁵H. Choi, R. Temam, P. Moin, and J. Kim, "Feedback control for unsteady flow and its application to the stochastic Burgers equation," *J. Fluid Mech.* **253**, 509 (1993).
- ⁶P. Moin and T. Bewley, "Application of control theory to turbulence," in the 12th Australasian Fluid Mechanics Conference, Sydney 10-15 December 1995 (unpublished), p. 109.
- ⁷S. L. Jacobson and W. C. Reynolds, "Active control of boundary layer wall shear stress using self-learning neural networks," AIAA Shear Flow Conference, Orlando, 1993 (unpublished), p. 1.
- ⁸M. Moller, "Efficient training of feed-forward neural networks," Ph.D. thesis, Aarhus University, Denmark, 1993.
- ⁹J. Kim, P. Moin, and R. Moser, "Turbulence statistics in fully-developed channel flow at low Reynolds number," *J. Fluid Mech.* **177**, 133 (1987).
- ¹⁰B. Widrow, "Adaptive inverse control," In the Second IFAC Workshop on Adaptive Systems in Control and Signal Processing, Lund, Sweden, 1987 (unpublished), pp. 1-5.
- ¹¹C. R. Smith, J. D. A. Walker, A. H. Haidari, and U. Sobrun, "On the dynamics of near-wall turbulence," *Philos. Trans. R. Soc. London Ser. A* **336**, 131 (1991).
- ¹²This staggered distribution of sensors and actuators would result in actuators at only half the grid points and this might reduce the effectiveness of the control. This problem can be solved simply by increasing resolution twice so that actuators locate at every grid point of the old grid system (these correspond to half the grid points in the new grid system) still with sensors located in staggered positions. This is possible since the weight distribution does not depend on the grid distance, but depends on the grid index as shown in Figs. 5 and 7.
- ¹³C. Liu, Y. C. Tai, J. B. Huang, and C. M. Ho, "Surface micromachined thermal shear stress sensor," in ASME Application of Microfabrication to Fluid Mechanics, Chicago, 1994 (unpublished), pp. 9-15.

Appendix 2

Suboptimal control of turbulent channel flow for drag reduction

By CHANGHOON LEE^{1†}, JOHN KIM¹
AND HAECHEON CHOI²

¹Department of Mechanical and Aerospace Engineering,
University of California, Los Angeles, CA 90095-1597, USA

²Department of Mechanical Engineering, Seoul National University, Seoul, Korea

(Received 13 May 1997 and in revised form 27 October 1997)

Two simple feedback control laws for drag reduction are derived by applying a suboptimal control theory to a turbulent channel flow. These new feedback control laws require pressure or shear-stress information only at the wall, and when applied to a turbulent channel flow at $Re_t = 110$, they result in 16–22% reduction in the skin-friction drag. More practical control laws requiring only the local distribution of the wall pressure or one component of the wall shear stress are also derived and are shown to work equally well.

1. Introduction

Recent studies have shown that near-wall streamwise vortices are responsible for high skin-friction drag in turbulent boundary layers. Many attempts aiming at controlling these vortices have been made in order to achieve a skin-friction drag reduction in turbulent boundary layers. Most of such attempts, however, have been *ad hoc*, largely based on physical intuition. The active control by Choi, Moin & Kim (1994), for example, used blowing and suction at the wall that is equal and opposite to the wall-normal component of the velocity at $y^+ = 10$, resulting in as much as 25% reduction in their numerical simulation. This approach, however, is impractical since the required velocity information at $y^+ = 10$ is not normally available. For any practical implementation a control scheme should be based solely on quantities measurable at the wall.

A more systematic approach based on an optimal control theory was proposed by Abergel & Temam (1990). Choi *et al.* (1993) proposed a ‘suboptimal’ control procedure, in which the iterations required for a global optimal control were avoided by seeking an optimal condition over a short time period. The suboptimal control procedure was successfully applied to control of the Burgers equation. Bewley & Moin (1994) were the first to apply the suboptimal control procedure to a turbulent flow and reported about 17% drag reduction. The procedure developed by Bewley & Moin (1994) still requires velocity information inside the flow in order to solve the adjoint problem, from which a feedback control input was derived. In spite of this obvious drawback, however, the fact that a control theory applied to a turbulent flow resulted in a substantial drag reduction is encouraging, since their control procedure was derived rigorously from a control theory, in which a pre-determined

† Present address: Department of Mechanical Engineering, University of Seoul, Seoul, Korea.

cost functional was minimized. Hill (1993, 1994) derived a control input as a function of the streamwise wall shear only by modeling the near-wall flow with a spanwise velocity growing linearly, and normal velocity growing quadratically, with normal distance from the wall. About 15% drag reduction was obtained from this study. We, however, derive a simple control scheme by minimizing cost functionals that are related to the streamwise vortices, which have been found to be responsible for large local drag in turbulent boundary layers. We also tried to minimize drag directly by having drag itself in the cost functional, but it was not successful (see §3). The objective of this paper is to demonstrate that a wise choice of the cost functional coupled with a variation of the formulation can lead to a more practical control law.

We present how to choose a cost functional and how to minimize it to yield simple feedback control laws that require quantities measurable only at the wall. One of the laws requires spatial information on the wall pressure over the entire wall and the other requires information, also over the entire wall, on one component of the wall shear stress. We then derive more practical control schemes that only require local wall pressure or local surface shear stress information, and show that they work equally well.

2. Suboptimal procedure

We follow a similar procedure used by Choi *et al.* (1993) and Bewley & Moin (1994). The problem under consideration is a turbulent channel flow, for which the governing equations are the Navier-Stokes and continuity equations with the no-slip boundary condition:

$$\frac{\partial u_i}{\partial t} + u_j \frac{\partial u_i}{\partial x_j} = -\frac{\partial p}{\partial x_i} + \frac{1}{Re} \frac{\partial^2 u_i}{\partial x_j \partial x_j}, \quad (2.1)$$

$$\frac{\partial u_j}{\partial x_j} = 0, \quad (2.2)$$

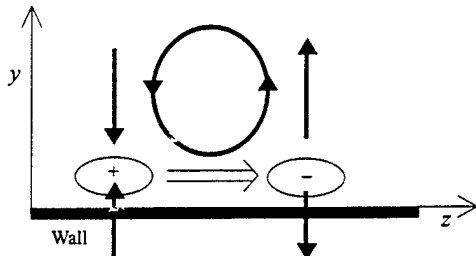
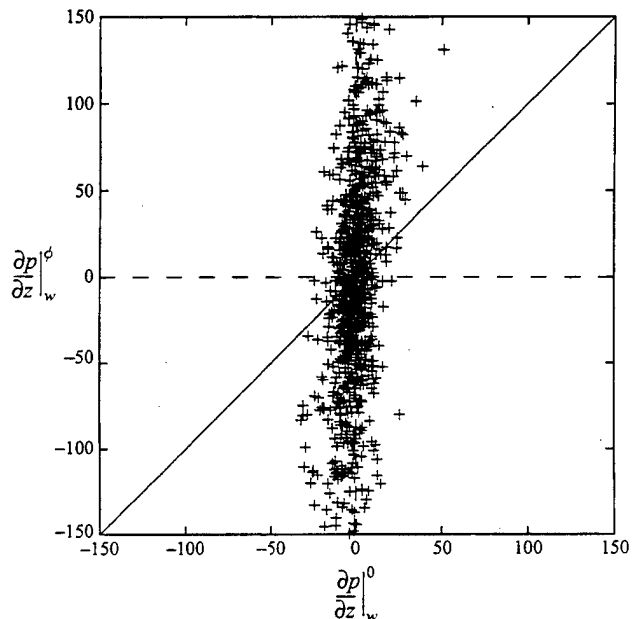
with

$$u_i|_w = \phi(x, z, t)\delta_{i2}, \quad (2.3)$$

where t is the time, x_1, x_2, x_3 are the streamwise, wall-normal, and spanwise directions respectively, u_i are the corresponding velocity components, p is the pressure, and Re is the Reynolds number, and the control input is the wall-normal velocity at the wall, ϕ .

All variables are non-dimensionalized by the wall shear velocity, u_t , and the channel half-width, δ . We also use interchangeably x, y, z for x_i and u, v, w for u_i . Periodic boundary conditions are imposed in the streamwise and spanwise directions. The flow rate in the streamwise direction is kept constant, and the drag is measured by the mean pressure gradient necessary to maintain the constant flow rate.

We found that the choice of the cost functional to be minimized is critical in the performance of the control. Since the streamwise vortices have been known to be responsible for large drag in turbulent boundary layers, we tried to choose the cost functional that is directly related to them. This is based on our conjecture that a suitable manipulation of the streamwise vortices would lead to drag reduction. We carefully selected two cost functionals based on our observation of a successful control of Choi *et al.* (1994). As shown in figure 1, Choi *et al.*'s (1994) blowing and suction, which are equal and opposite to the wall-normal velocity component at $y^+ = 10$, effectively suppress a streamwise vortex by counteracting up-and-down

FIGURE 1. Schematic of a pressure field induced by a control based on $y^+ = 10$.FIGURE 2. Correlation between a pressure field of a no-control case and a pressure field modified by a control based on information at $y^+ = 10$. A line indicating no change of the pressure field is drawn for guidance.

motion induced by the vortex. This blowing and suction creates locally high pressure in the near-wall region marked with '+', and low pressure in the region marked with '−' in figure 1. A crucial aspect of the present analysis is the observation that this blowing and suction *increases* the pressure gradient in the spanwise direction under the streamwise vortex near the wall. To demonstrate this behaviour, we examine computed flow fields. Figure 2 shows a scatter plot between two pressure gradient fields: $\partial p / \partial z|_w^0$ is the pressure gradient before the control is applied and $\partial p / \partial z|_w^\phi$ is the pressure gradient at the same location after the control of Choi *et al.* (1994) is applied for one time step. It is apparent that the control increased the pressure gradient significantly. For the uncontrolled case, Re_τ , based on the wall-shear velocity and the channel half-width is about 110. The spectral code of Kim, Moin & Moser (1987) is used for all the computations presented here. Simulations are carried out

using $32 \times 65 \times 32$ spectral modes (with dealiasing in the streamwise and spanwise directions) with the computational domain of $4\pi\delta \times 2\delta \times 4\pi\delta/3$, respectively.

The above argument suggests that we should seek blowing and suction that increases the pressure gradient in the spanwise direction near the wall for a short time period (i.e. in the suboptimal sense) in order to achieve a similar drag reduction to that achieved by Choi *et al.*'s (1994) control. The cost functional $\mathcal{J}(\phi)$ to be minimized is then

$$\mathcal{J}(\phi) = \frac{\ell}{2A\Delta t} \int_S \int_t^{t+\Delta t} \phi^2 dt dS - \frac{1}{2A\Delta t} \int_S \int_t^{t+\Delta t} \left(\frac{\partial p}{\partial z} \right)_w^2 dt dS, \quad (2.4)$$

where the integrations are over the wall (S) in space and over a short duration in time Δt , which typically corresponds to the time step used in the numerical computation, and ℓ is the relative price of the control since the first term on the right-hand side represents the cost of the actuation ϕ . Note that there is a minus sign in front of the second term since we want to maximize the pressure gradient. It should be noted that the spanwise pressure gradient at the wall will be eventually reduced when the strength of the near-wall streamwise vortices is reduced through successful control. Here, blowing and suction that increase the spanwise pressure gradient for the next step are sought as a suboptimal control.

To minimize the cost functional, we first define the differential states of the velocity and pressure, (θ_i, ρ) , using a Fréchet differential (Finlayson 1972),

$$\theta_i = \frac{\mathcal{D}u_i(\phi)}{\mathcal{D}\phi} \tilde{\phi}, \quad (2.5)$$

$$\rho = \frac{\mathcal{D}p}{\mathcal{D}\phi} \tilde{\phi}, \quad (2.6)$$

where

$$\frac{\mathcal{D}f(\phi)}{\mathcal{D}\phi} \tilde{\phi} = \lim_{\epsilon \rightarrow 0} \frac{f(\phi + \epsilon \tilde{\phi}) - f(\phi)}{\epsilon}, \quad (2.7)$$

$\tilde{\phi}$ being an arbitrary perturbation field to ϕ .

Next, we choose the Crank–Nicolson scheme for the linear terms and a Runge–Kutta scheme for the nonlinear terms to yield a discretized form of (2.1) and (2.2):

$$u_i^{n+1} - \frac{\Delta t}{2Re} \frac{\partial^2 u_i^{n+1}}{\partial x_j \partial x_j} + \frac{\Delta t}{2} \frac{\partial p^{n+1}}{\partial x_i} + R^n = 0, \quad (2.8)$$

$$\frac{\partial u_j^{n+1}}{\partial x_j} = 0, \quad (2.9)$$

with

$$u_i^{n+1}|_w = \phi \delta_{i2}, \quad (2.10)$$

where the superscripts $n+1$ and n denote the time step, and R^n includes the nonlinear terms and the explicit parts of the pressure gradient and viscous terms. The Fréchet differential of (2.8)–(2.10) yields the governing equations for the differential states (θ_i, ρ) ,

$$\theta_i^{n+1} - \frac{\Delta t}{2Re} \frac{\partial^2 \theta_i^{n+1}}{\partial x_j \partial x_j} + \frac{\Delta t}{2} \frac{\partial \rho^{n+1}}{\partial x_i} = 0, \quad (2.11)$$

$$\frac{\partial \theta_j^{n+1}}{\partial x_j} = 0, \quad (2.12)$$

with

$$\theta_i^{n+1}|_w = \tilde{\phi} \delta_{i2}. \quad (2.13)$$

Note that $(\mathcal{D}R^n/\mathcal{D}\phi) \tilde{\phi} = 0$. Hereinafter, we drop the superscript $n+1$ and all variables are understood to be at the $(n+1)$ th time step. Note that there is no contribution from the nonlinear terms, thus making the equations linear. Generally, the suboptimal formulation depends on the time advancement scheme used, as shown here (see also Choi *et al.* 1993). Dropping the nonlinear terms may miss important flow dynamics. However, we found from our numerical tests with the full nonlinear terms included that the contribution from the nonlinear terms is negligible in our boundary control with short optimization interval Δt ; it turns out that the conservation of mass due to the wall actuation dominates the near-wall dynamics.

Under the approximation that $2Re/\Delta t \gg k^2$, where $k = (k_x^2 + k_z^2)^{1/2}$, and k_x and k_z denote the streamwise and spanwise wavenumbers in the x - and z -directions respectively†, the above equations have the following solutions in the semi-infinite domain with periodic conditions in the x - and z -directions (see the Appendix):

$$\hat{\theta}_1(y) = \frac{ik_x}{k} \hat{\phi} (\exp[-(2Re/\Delta t)^{1/2}y] - e^{-ky}), \quad (2.14)$$

$$\hat{\theta}_3(y) = \frac{ik_z}{k} \hat{\phi} (\exp[-(2Re/\Delta t)^{1/2}y] - e^{-ky}), \quad (2.15)$$

$$\hat{\theta}_2(y) = \hat{\phi} e^{-ky}, \quad (2.16)$$

$$\hat{\rho}(y) = \frac{2}{k \Delta t} \hat{\phi} e^{-ky}, \quad (2.17)$$

where $\hat{\theta}_j$, $\hat{\rho}$, and $\hat{\phi}$ are the Fourier coefficients of θ_j , ρ , and $\tilde{\phi}$ respectively. For the channel geometry, we originally considered both walls and found that the interaction between two walls is negligible as long as the typical wavelength ($\sim 2\pi/k$) associated with near-wall structures is much smaller than the channel width.

The Fréchet differential of the cost functional (2.4) becomes

$$\frac{\mathcal{D}\mathcal{J}}{\mathcal{D}\phi} \tilde{\phi} = \frac{\ell}{A\Delta t} \int_S \int_t^{t+\Delta t} \phi \tilde{\phi} dt dS - \frac{1}{A\Delta t} \int_S \int_t^{t+\Delta t} \left. \frac{\partial p}{\partial z} \right|_w \left. \frac{\partial \rho}{\partial z} \right|_w dt dS. \quad (2.18)$$

The Fourier representation of the above equation is

$$\widehat{\frac{\mathcal{D}\mathcal{J}}{\mathcal{D}\phi}} \hat{\phi}^* = \ell \hat{\phi} \hat{\phi}^* - \left. \widehat{\frac{\partial p}{\partial z}} \right|_w \left. \widehat{\frac{\partial \rho}{\partial z}} \right|_w, \quad (2.19)$$

where the hat denotes the Fourier coefficient, and the superscript * denotes the complex conjugate. From (2.17), $\widehat{\partial \rho / \partial z}|_w$ can be expressed in terms of $\hat{\phi}^*$,

$$\left. \widehat{\frac{\partial \rho}{\partial z}} \right|_w = -\frac{2ik_z}{k \Delta t} \hat{\phi}^*. \quad (2.20)$$

Equation (2.19) then reduces to

$$\widehat{\frac{\mathcal{D}\mathcal{J}}{\mathcal{D}\phi}} \hat{\phi}^* = \ell \hat{\phi} \hat{\phi}^* - \frac{2k_z^2}{k \Delta t} \hat{\rho}_w \hat{\phi}^*. \quad (2.21)$$

† It can be shown that $2Re/\Delta t k_{max}^2 \sim Re^{1/4} \gg 1$. Here we used $u\Delta t/\Delta x \sim O(1)$ and $k_{max} \sim k_\eta \sim Re^{3/4}$, where k_η is the wavenumber corresponding to the Kolmogorov length scale.

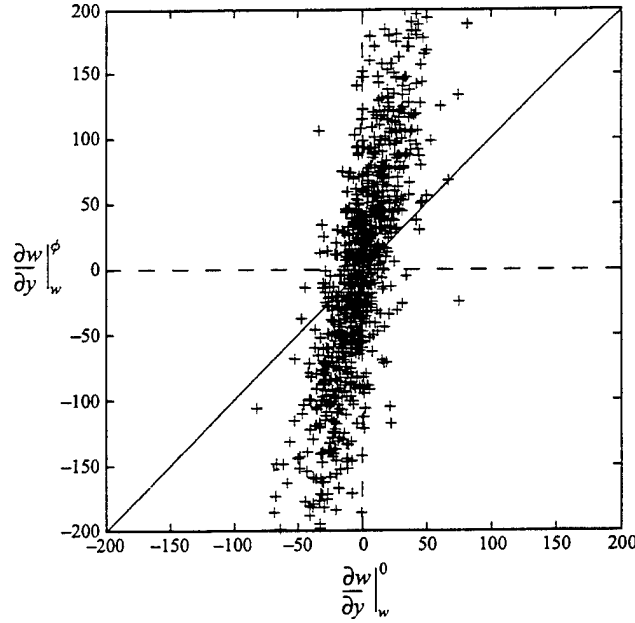


FIGURE 3. Correlation between a spanwise wall-shear stress of a no-control case and a spanwise wall-shear stress modified by a control based on $y^+ = 10$. A line indicating no change of the spanwise wall-shear stress field is drawn for guidance.

For an arbitrary $\hat{\phi}$, equation (2.21) should be satisfied, yielding

$$\widehat{\frac{\mathcal{D}\mathcal{J}}{\mathcal{D}\phi}} = \ell\hat{\phi} - \frac{2k_z^2}{k\Delta t}\hat{p}_w. \quad (2.22)$$

From the requirement that the Fréchet differential of the cost functional be minimized, i.e. $\mathcal{D}\mathcal{J}/\mathcal{D}\phi = 0$, the optimum $\hat{\phi}$ then becomes

$$\hat{\phi} = C \frac{k_z^2}{k} \hat{p}_w, \quad (2.23)$$

where C is a positive scale factor that determines the cost of the actuation. Equation (2.23) indicates that the optimum wall actuation is negatively proportional to the second spanwise derivative of the wall pressure, with the high-wavenumber components reduced by $1/k$.

Another wall quantity that indicates similar changes of the near-wall dynamics due to the altered pressure field is the spanwise shear at the wall, $\partial w/\partial y$. Owing to the added pressure gradient in the spanwise direction below the streamwise vortex, the spanwise flow near the wall is also induced, thus increasing the spanwise shear stress at the wall (see figure 1). The scatter plot between the spanwise shear stress at the wall from two different fields, one of which is from an unperturbed channel and the other with the control based on $y^+ = 10$, is shown in figure 3. Thus another choice for the cost functional to be minimized is

$$\mathcal{J}(\phi) = \frac{\ell}{2A\Delta t} \int_S \int_t^{t+\Delta t} \phi^2 dt dS - \frac{1}{2A\Delta t} \int_S \int_t^{t+\Delta t} \left(\frac{\partial w}{\partial y} \right)_w^2 dt dS. \quad (2.24)$$

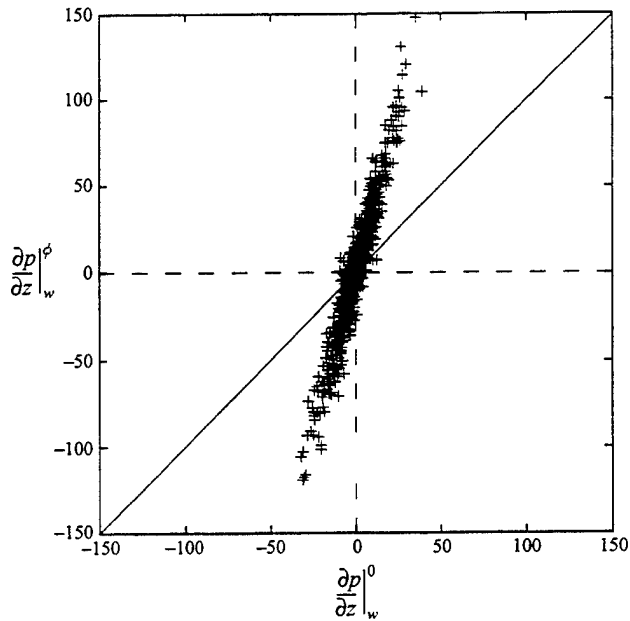


FIGURE 4. Correlation between a pressure field of a no-control case and a pressure field modified by a control based on equation (2.23).

Following the procedure that led to equation (2.23) yields the optimum actuation:

$$\hat{\phi} = C \frac{ik_z}{k} \left. \widehat{\frac{\partial w}{\partial y}} \right|_w . \quad (2.25)$$

Equation (2.25) indicates that the optimum wall actuation should be proportional to the spanwise derivative of the spanwise shear at the wall, with the high-wavenumber components reduced by $1/k$. Note that the scale factor C in equations (2.23) and (2.25) is arbitrary. As mentioned before, the suboptimal formulation depends on the time-advancement scheme used. However, if we used a different implicit scheme, only the resulting constant C would be different. This does not cause a problem since C is chosen such that the r.m.s. value of the wall actuation is maintained at a given value.

In the following simulations, we set the r.m.s. value of ϕ to be equal to that of the wall-normal velocity at $y^+ = 10$, which gives the same r.m.s. value of wall actuations as that of Choi *et al.* (1994).

3. Results

The above control laws (2.23) and (2.25) are tested in a turbulent channel flow. The pressure gradient at the wall is monitored to see if the equation (2.23) control increases the pressure gradient when the control law is applied. It behaves as expected, as shown in figure 4. The spanwise shear stress at the wall also increases when the equation (2.25) control is applied (see figure 5). These results also confirm that a suboptimal procedure without the nonlinear terms does not cause an error for our

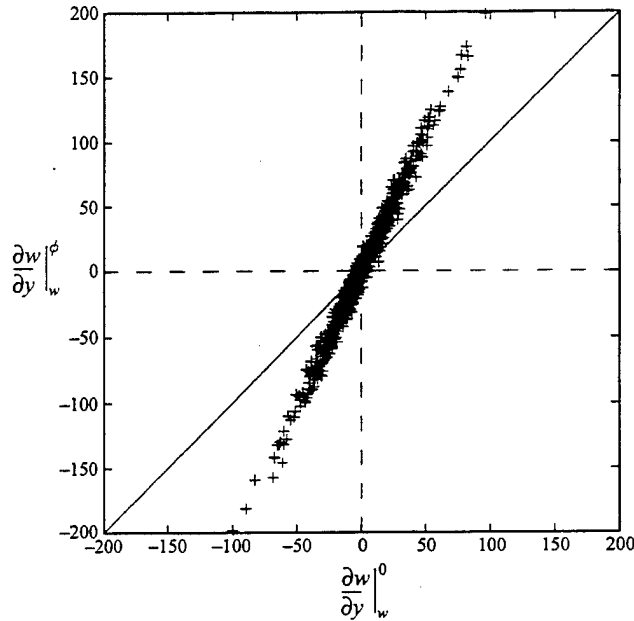


FIGURE 5. Correlation between a spanwise wall-shear stress of a no-control case and a spanwise wall-shear stress modified by a control based on equation (2.25).

boundary controls. Since these control laws specifically increase the wall pressure gradient or spanwise wall-shear stress, correlations between these variables before and after control are much higher than those corresponding to the control based on $y^+ = 10$ information. This suggests that the controls based on equations (2.23) and (2.25) modify the flow in a different manner from the control based on information at $y^+ = 10$.

Time histories of the mean streamwise wall-shear stress for different control laws are shown in figures 6 and 7. As control begins, an immediate drop in the shear stress is observed for all cases. At the same expense (i.e. the same r.m.s. value of ϕ), the control based on (2.25), which reduces drag by as much as 22%, is apparently more effective than that based on (2.23) which reduces drag by 16%. This indicates that the spanwise wall-shear stress is a better quantity for control input.

The control laws presented above, however, are still impractical to implement, since they are expressed in terms of the Fourier coefficients (i.e. in wavenumber space), which require information over the entire spatial domain. Therefore, the inverse transforms of k_z^2/k and ik_z/k are sought numerically so that the convolution integral can be used to express the control laws in physical space. The discrete representation of each control law then becomes†:

$$\phi(x_j, z_k) = C \sum_{j'} \sum_{k'} W_{jk'}^p p_w(x_{j+j'}, z_{k+k'}) \quad (3.1)$$

† Since k_z^2/k and ik_z/k are not periodic in the wavenumber space, a high resolution was used to obtain W_{jk}^p and W_{jk}^w to minimize aliasing error.

	$k (= z/\Delta z)$							
	0	1	2	3	4	5	6	
$j (= x/\Delta x)$	0	1.0000	-0.4427	0.0031	-0.0440	0.0044	-0.0138	0.0032
	1	0.0413	-0.0007	-0.0040	-0.0037	-0.0029	-0.0021	-0.0016
	2	-0.0110	0.0057	0.0019	0.0011	0.0002	0.0000	-0.0003

TABLE 1. The weight distribution of equation (3.1), W_{jk}^p . The weights are symmetric between j and $-j$ and k and $-k$. The weights are normalized by W_{00}^p . Bold faced weights are used in the calculation of figure 6. Here, $\Delta x^+ = 40$ and $\Delta z^+ = 13$ ($\Delta x = 3\Delta z$).

	$k (= z/\Delta z)$							
	0	1	2	3	4	5	6	
$j (= x/\Delta x)$	0	0.0000	1.0000	-0.1039	0.2679	-0.0852	0.1419	-0.0671
	1	0.0086	0.0537	0.0503	0.0310	0.0340	0.0148	0.0237
	2	0.0001	-0.0104	0.0059	0.0051	0.0100	0.0074	0.0092

TABLE 2. The weight distribution of equation (3.2), W_{jk}^w . The weights are symmetric between j and $-j$ and antisymmetric between k and $-k$. The weights are normalized by W_{01}^w . Bold faced weights are used in the calculation of figure 7. Here, $\Delta x^+ = 40$ and $\Delta z^+ = 13$ ($\Delta x = 3\Delta z$).

and

$$\phi(x_j, z_k) = C \sum_{j'} \sum_{k'} W_{jk'}^w \left. \frac{\partial w}{\partial y} \right|_w (x_{j+j'}, z_{k+k'}), \quad (3.2)$$

respectively. The subscripts, j and k , denote the discretizing indices in the x - and z -directions respectively. The weights, W_{jk}^p and W_{jk}^w , are given in tables 1 and 2. Note that the weights decay rapidly with distance from the point of interest, suggesting that the optimum actuation can be obtained by a local weighted average of the pressure or spanwise shear stress. The results obtained using a 37-point average for the pressure and an 11-point average for the spanwise shear stress yield about the same drag reduction as that obtained from full integration using equations (2.23) and (2.25) (see figures 6 and 7). The weights used in these calculations are bold-faced in tables 1 and 2. It is remarkable that localized information can produce such a significant drag reduction, especially for the control with the spanwise shear stress.

The weight distribution W_{jk}^w for $j = 0$ is very similar to the one found in the application of neural networks to the same turbulent flow (Lee *et al.* 1997), in which only a single strip of the spanwise shear information was used in the network. The control law of Lee *et al.*,

$$\hat{\phi} = C \frac{ik_z}{|k_z|} \left. \widehat{\frac{\partial w}{\partial y}} \right|_w, \quad (3.3)$$

produces almost the same distribution of blowing and suction as the present results. Note that blowing and suction from equation (2.25) are nearly the same as those from equation (3.3) because the near-wall structures have relatively slow variation in the streamwise direction (the $k_x = 0$ component is dominant). This blowing and suction distribution is also very similar to the one based on $y^+ = 10$ data (see Lee *et al.* 1997).

In figure 8, contours of the streamwise vorticity in a cross-flow plane for the control with equation (2.25) are compared with a no-control case. Significant reduction in

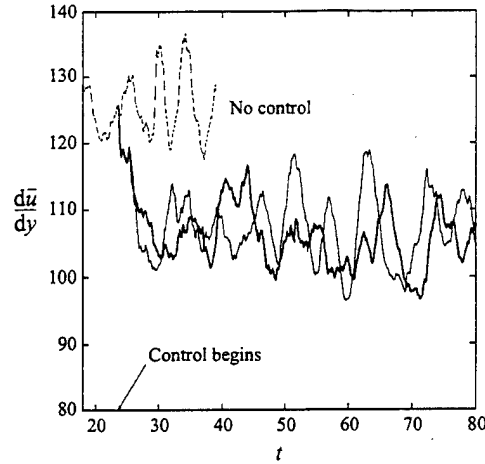


FIGURE 6. Mean streamwise wall-shear stress for various control laws based on the wall pressure, compared to the no-control case: thick solid line, the control law expressed in Fourier space, equation (2.23); thin solid line, the control law expressed in physical space, equation (3.1) with the integration radius of $6\Delta z$. $\Delta t^+ \simeq 0.2$.

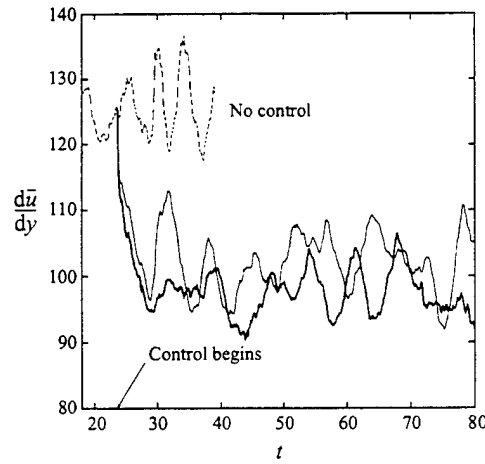


FIGURE 7. Mean streamwise wall-shear stress for various control laws based on the spanwise wall-shear stress compared to the no-control case: thick solid line, the control law expressed in Fourier space, equation (2.25); thin solid line, the control law expressed in physical space, equation (3.2) with 11 points in the spanwise direction only. $\Delta t^+ \simeq 0.2$.

the strength of the streamwise vortices is evident. This again confirms the notion that a successful manipulation of the near-wall streamwise vortices can lead to drag reduction. The mean streamwise velocity and root-mean-square velocity near the wall are shown in figures 9 and 10, respectively, and compared with the no-control case. The trends are very similar to Choi *et al.* (1994) and Lee *et al.* (1997).

Finally, we mention that we tried to find a feedback control scheme minimizing the

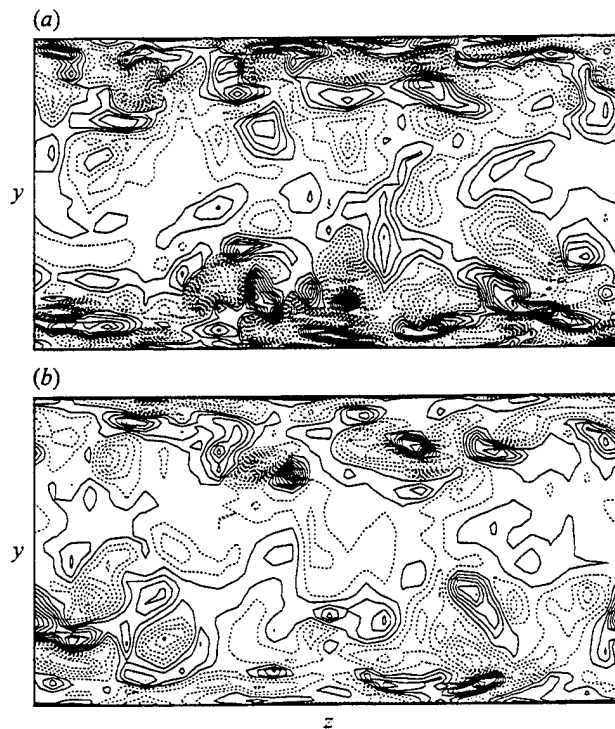


FIGURE 8. Contours of the streamwise vorticity in a cross-flow plane: (a) no control; (b) control based on wall-shear stress (equation (2.25)). The contour level increment is the same for both figures. Negative contours are dashed.

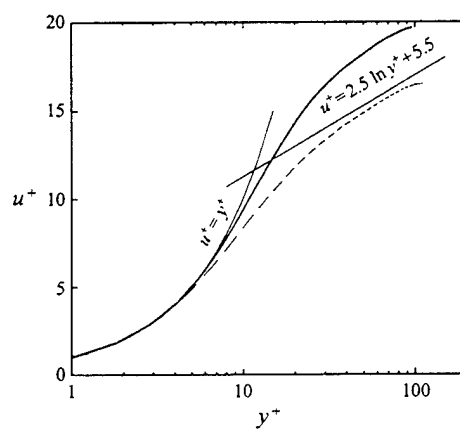


FIGURE 9. The mean streamwise velocity normalized by u_t : Thick solid line, control law (2.25); dashed line, no control. For the controlled case, the velocity is normalized by the controlled u_t .

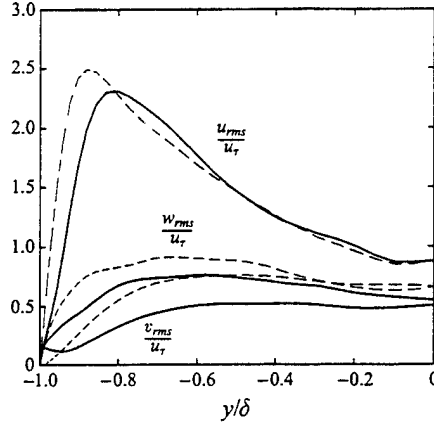


FIGURE 10. The root-mean-square velocity normalized by u_r of the uncontrolled flow: thick solid line, control law (2.25); dashed line, no control.

following cost functional:

$$\mathcal{J}(\phi) = \frac{\ell}{2A\Delta t} \int_S \int_t^{t+\Delta t} \phi^2 dt dS + \frac{1}{2A\Delta t} \int_S \int_t^{t+\Delta t} \left(\frac{\partial u}{\partial y} \right)_w^m dt dS, \quad (3.4)$$

with $m = 1$ or 2 . This cost functional is the most natural choice since it contains the quantity directly related to drag. We followed the same procedure to derive the following control schemes:

$$\hat{\phi} = 0, \quad (3.5)$$

for $m = 1$, and

$$\hat{\phi} = -C \frac{ik_x}{k} \left. \widehat{\frac{\partial u}{\partial y}} \right|_w, \quad (3.6)$$

for $m = 2$. Equation (3.5) obviously does not reduce drag and equation (3.6) increased drag in our numerical simulations. This failure appears to be due to the neglect of the nonlinear terms in our formulation, since the numerical solution of the optimum wall actuations with the full nonlinear terms gave different results (Bewley & Moin 1994). This suggests that even in a short time interval the nonlinear terms should be included in the suboptimal formulation when drag itself is chosen as the cost functional. Manipulation of the streamwise vortices by wall actuation, however, can be accomplished through a linear process as shown in the previous section. It appears that having a term that is directly related to near-wall streamwise vortices in the cost functional indirectly includes the nonlinear effect. This is probably related to the fact that near-wall streamwise vortices are self-sustained by a nonlinear process (Hamilton, Kim & Waleffe 1995). If the nonlinear terms are included, of course, it is impossible to derive the feedback control law in closed form without approximation. Hill (1993), on the other hand, considered the nonlinear term by modelling the near-wall flow using the Taylor series expansion and presented a feedback control law in closed form, which resulted in about 15% drag reduction.

4. Summary

We have obtained two simple feedback control laws for drag reduction by applying a suboptimal control procedure to a turbulent flow. This was possible since we selected two cost functionals guided by the successful control based on quantities monitored at $y^+ = 10$. The present control laws perform very well resulting in substantial drag reductions when applied to a turbulent channel flow. More convenient control schemes requiring only local information were also derived, and were shown to work equally well. They require quantities measurable only at the surface and thus should be easier to implement in practice. The present results further substantiate the notion that a successful manipulation of the near-wall streamwise vortices is the key to boundary-layer control for drag reduction.

We are grateful to Dr Gary Coleman and Mr Hong Zhang for useful discussions. This work was supported by AFOSR grant F49620-95-10263 (Program Managers, Drs James M. McMichael and Marc N. Glauser). Computer time was provided by the NAS Program of NASA Ames Research Center, the San Diego Supercomputer Center, and the DoD High Performance Computing Center. H.C. acknowledges the support by KOSEF through Turbo and Power Machinery Research Center.

Appendix. Derivation of the solution (2.14)–(2.17)

Equations for the differential states (θ_i, ρ) , (2.11), (2.12) can be rewritten in terms of the Fourier coefficients,

$$\hat{\theta}_1 - \frac{\Delta t}{2Re} \left(\frac{d^2}{dy^2} - k^2 \right) \hat{\theta}_1 + \frac{ik_x \Delta t}{2} \hat{\rho} = 0, \quad (\text{A } 1)$$

$$\hat{\theta}_2 - \frac{\Delta t}{2Re} \left(\frac{d^2}{dy^2} - k^2 \right) \hat{\theta}_2 + \frac{\Delta t}{2} \frac{d\hat{\rho}}{dy} = 0, \quad (\text{A } 2)$$

$$\hat{\theta}_3 - \frac{\Delta t}{2Re} \left(\frac{d^2}{dy^2} - k^2 \right) \hat{\theta}_3 + \frac{ik_z \Delta t}{2} \hat{\rho} = 0, \quad (\text{A } 3)$$

$$ik_x \hat{\theta}_1 + ik_z \hat{\theta}_3 + \frac{d\hat{\theta}_2}{dy} = 0, \quad (\text{A } 4)$$

with

$$\hat{\theta}_i(0) = \hat{\phi}\delta_{i2}, \quad \hat{\theta}_i(\infty) = 0, \quad (\text{A } 5)$$

where $\hat{\theta}_i$ and $\hat{\rho}$ are defined as follows:

$$\theta_i = \sum_{k_x} \sum_{k_z} \hat{\theta}_i(y) e^{ik_x x} e^{ik_z z}, \quad (\text{A } 6)$$

$$\rho = \sum_{k_x} \sum_{k_z} \hat{\rho}(y) e^{ik_x x} e^{ik_z z}. \quad (\text{A } 7)$$

The operation $ik_x \cdot (\text{A } 1) + d/dy(\text{A } 2) + ik_z \cdot (\text{A } 3)$ together with equation (A 4) yields

$$\frac{d^2 \hat{\rho}}{dy^2} - k^2 \hat{\rho} = 0, \quad (\text{A } 8)$$

which has a non-growing solution,

$$\hat{\rho} = \hat{\rho}_w e^{-ky}, \quad (\text{A } 9)$$

with a wall value, $\hat{\rho}_w$, which will be determined later. Using (A 9), we can find solutions to equations (A 1), (A 2), (A 3),

$$\hat{\theta}_1(y) = \frac{\Delta t}{2} i k_x \hat{\rho}_w (\exp[-(k^2 + 2Re/\Delta t)^{1/2}y] - e^{-ky}), \quad (A 10)$$

$$\hat{\theta}_3(y) = \frac{\Delta t}{2} i k_z \hat{\rho}_w (\exp[-(k^2 + 2Re/\Delta t)^{1/2}y] - e^{-ky}), \quad (A 11)$$

$$\hat{\theta}_2(y) = \left(\hat{\phi} - \frac{\Delta t}{2} k \hat{\rho}_w \right) \exp[-(k^2 + 2Re/\Delta t)^{1/2}y] + \frac{\Delta t}{2} k \hat{\rho}_w e^{-ky}. \quad (A 12)$$

With these, equation (A 4) reduces to

$$\left(-\left(k^2 + \frac{2Re}{\Delta t} \right)^{1/2} \left(\hat{\phi} - \frac{\Delta t}{2} k \hat{\rho}_w \right) - \frac{\Delta t}{2} k^2 \hat{\rho}_w \right) \exp[-(k^2 + 2Re/\Delta t)^{1/2}y] = 0. \quad (A 13)$$

Since $2Re/\Delta t \gg k^2$, equation (A 13) yields

$$\hat{\rho}_w = \frac{2}{\Delta t k} \hat{\phi}. \quad (A 14)$$

With this, equations (A 10), (A 11), (A 12), (A 9) become equations (2.14), (2.15), (2.16), (2.17), respectively.

REFERENCES

- ABERGEL, F. & TEMAM, R. 1990 On some control problems in fluid mechanics. *Theor. Comput. Fluid Dyn.* 1, 303.
- BEWLEY, T. & MOIN, P. 1994 Optimal control of turbulent channel flows. In *Active Control of Vibration and Noise* (ed. K. W. Wang, A. H. Von Flotow, R. Shoureshi, E. W. Hendricks & T. W. Farabee). ASME DE-Vol. 75.
- CHOI, H.; MOIN, P. & KIM, J. 1994 Active turbulence control for drag reduction in wall-bounded flows. *J. Fluid Mech.* 262, 75.
- CHOI, H., TEMAM, R., MOIN, P. & KIM, J. 1993 Feedback control for unsteady flow and its application to the stochastic Burgers equation. *J. Fluid Mech.* 245, 509.
- FINLAYSON, B. A. 1972 *The Method of Weighted Residuals and Variational Principles*. Academic.
- HAMILTON, J. M., KIM, J. & WALEFFE, F. 1995 Regeneration mechanisms of near-wall turbulence structures. *J. Fluid Mech.* 287, 317.
- HILL, D. C. 1993 Drag reduction at a plane wall. *Annual Research Briefs*. Center for Turbulence Research, Stanford University.
- HILL, D. C. 1994 Drag reduction strategies. *Annual Research Briefs*. Center for Turbulence Research, Stanford University.
- KIM, J., MOIN, P. & MOSER, R. 1987 Turbulence statistics in fully developed channel flow at low Reynolds number. *J. Fluid Mech.* 177, 133.
- LEE, C., KIM, J., BABCOCK, D. & GOODMAN, R. 1997 Application of neural networks to turbulence control for drag reduction. *Phys. Fluids* 9, 1740.

Appendix 3

A systems theory approach to the feedback stabilization of infinitesimal and finite-amplitude disturbances in plane Poiseuille flow

By SANJAY S. JOSHI†, JASON L. SPEYER AND JOHN KIM

School of Engineering and Applied Science, University of California, Los Angeles
Los Angeles, CA 90024, USA

(Received 14 February 1995 and in revised form 15 July 1996)

A systems theory framework is presented for the linear stabilization of two-dimensional laminar plane Poiseuille flow. The governing linearized Navier–Stokes equations are converted to control-theoretic models using a numerical discretization scheme. Fluid system poles, which are closely related to Orr–Sommerfeld eigenvalues, and fluid system zeros are computed using the control-theoretic models. It is shown that the location of system zeros, in addition to the well-studied system eigenvalues, are important in linear stability control. The location of system zeros determines the effect of feedback control on both stable and unstable eigenvalues. In addition, system zeros can be used to determine sensor locations that lead to simple feedback control schemes. Feedback controllers are designed that make a new fluid–actuator–sensor–controller system linearly stable. Feedback control is shown to be robust to a wide range of Reynolds numbers. The systems theory concepts of modal controllability and observability are used to show that feedback control can lead to short periods of high-amplitude transients that are unseen at the output. These transients may invalidate the linear model, stimulate nonlinear effects, and/or form a path of ‘bypass’ transition in a controlled system. Numerical simulations are presented to validate the stabilization of both single-wavenumber and multiple-wavenumber instabilities. Finally, it is shown that a controller designed upon linear theory also has a strong stabilizing effect on two-dimensional finite-amplitude disturbances. As a result, secondary instabilities due to infinitesimal three-dimensional disturbances in the presence of a finite-amplitude two-dimensional disturbance cease to exist.

1. Introduction

A basic problem in fluid dynamics is the theoretical understanding of how instability in laminar shear flow leads to transition to turbulence. Since laminar flow is preferred in many applications, the suppression of fluid instabilities to maintain laminar flow would be very useful. Towards this goal, active boundary layer control of instability has been proposed. The nonlinear aspects of the transition process are still not clearly known. It has been shown (Orszag & Patera 1983) that some shear flows may sustain two-dimensional finite-amplitude instabilities that cause infinitesimal three-dimensional disturbances to be highly unstable. This two-dimensional primary instability/three-dimensional secondary instability process may be one nonlinear mechanism that leads to transition. Conversely, the behaviour of infinitesimal

† Present address: Jet Propulsion Laboratory, 4800 Oak Grove Drive, Pasadena, CA 91109, USA.

(linear) disturbances in laminar shear flow is well understood (Orr 1907; Sommerfeld 1908; Drazin & Reid 1981). Therefore, linear analysis provides a natural starting point to begin to develop active control schemes that may eventually lead to full transition control. It is the purpose of this paper to develop feedback controllers based on linear theory that stabilize two-dimensional plane Poiseuille flow to infinitesimal disturbances. In addition, it will be shown that a controller designed upon linear theory has a strong stabilizing effect on two-dimensional finite-amplitude instabilities. As a result, secondary three-dimensional instabilities as described in Orszag & Patera (1983) cease to exist in such a system.

Most prior work in the area of laminar flow linear instability suppression has concentrated on the wave superposition approach. A nice survey of past work is given in Joslin, Erlebacher & Hussaini (1994). The basic idea is that boundary layer instabilities appear as a combination of many sinusoidally growing waves of certain frequencies, phases, and amplitudes. If these wave parameters are known, or if they can be determined, a second wave may be stimulated in the flow that is exactly out of phase with the instability wave. In this way, the two waves may destructively interfere and flow may be stabilized. Disturbance of the flow field to cause a wave motion to appear has been experimentally demonstrated using several methods such as vibrating ribbons (Schubauer & Skramstad 1947), vibrating wires (Milling 1981), and heating elements (Nosenchuck 1982). In addition, several authors have numerically obtained wave superposition results based on Navier-Stokes simulations (Beringen 1984; Metcalfe *et al.* 1986). Most of the results, however, report incomplete destruction of instability waves. Joslin *et al.* (1994) explain that wave cancellation is very sensitive to the wave parameters and postulate that incomplete destruction reported in past studies was due to improper phase or amplitude properties of the cancelling wave.

In addition, Bower, Kegelman & Pal (1987) considered the Orr-Sommerfeld equation in designing an input to channel flow that may counteract the effects of a disturbance that excites instabilities. They showed that if an oscillating flat pulse function at the lower boundary of a channel excited inherent instabilities, a second oscillating flat pulse function could be constructed downstream that negated excitement of the instabilities. Much like the wave superposition approach, their aim was not to stabilize the underlying dynamics of the problem, but rather to 'cancel' the effects of a specific disturbance.

Unlike past work, our aim is to use systems theory to construct a combination fluid-actuator-sensor-controller *system* that is inherently stable. In essence, the approach changes the philosophy of the problem from thinking about how inputs can mitigate an inherently unstable system to thinking about how sensors and actuators can be added to form an entirely new *stable* system. Recently, mathematical control systems theory has begun to be applied to fluid systems (Burns & Ou 1994; Gunzburger, Hou & Suobodny 1992; Choi, Moin & Kim 1993). A control theory approach for laminar flow linear instability suppression will be shown to have several advantages over the traditional wave cancellation approach. It will eliminate the need to explicitly measure phase and frequency of instabilities. Also, it will provide a framework to select sensor locations in order to have the least complex controller. Further, feedback control will be shown to be extremely robust to changing Reynolds numbers given proper sensor location. In addition, linear feedback controllers will be shown to have a strong stabilizing effect on two-dimensional finite-amplitude disturbances.

This paper is organized as follows. In §2, we formulate the linear channel flow problem using the linearized Navier-Stokes equations. Boundary input in the form

of blowing/suction and boundary output in terms of shear are represented within the equations. In §3, we introduce the concepts of zeros and poles of a system, as well as control-theoretic models. The governing partial-differential equation for the system is converted into a set of first-order, ordinary differential equations via a Galerkin method. These first-order, ordinary differential equations are then converted into a control-theoretic model. Section 4 describes the infinite-dimensional nature of the channel flow system and how it affects the selection of actuation. Section 5 describes the numerical model and the verification of the calculated poles and zeros. Section 6 introduces feedback control design. It is shown that judicious sensor placement, based on zero locations, can lead to simple control schemes. Furthermore, the control system is extremely robust to change in Reynolds number. Section 7 explores unobservable modal reinforcement as a possible path of ‘bypass’ transition in a controlled system. It then shows how a particular control model, called the modal-canonical state space model, may be used to assess observability of modal reinforcement. Section 8 demonstrates multiple-wavenumber instability control. Section 9 demonstrates that a linear controller has a strong stabilizing effect on two-dimensional, finite-amplitude instabilities. As a result, secondary three-dimensional instabilities as described by Orszag & Patera (1983) cease to exist. Finally, §10 outlines conclusions.

2. Problem formulation

2.1. Dynamic equations

We consider two-dimensional plane Poiseuille flow between two parallel stationary plates. Let the channel be of finite length and finite height, with the centreline at zero. The flow in the channel is described by the unsteady nonlinear incompressible Navier–Stokes equations. In order to study the linear stability of the system, we follow the standard procedure. Consider small perturbations in the velocities of $\hat{u}(x, y, t)$ in the horizontal direction, $\hat{v}(x, y, t)$ in the vertical direction, and $\hat{p}(x, y, t)$ in the pressure field. Let the primary flow be represented by $U(y)$ with U_c being the centreline velocity. The linearized incompressible Navier–Stokes equations may be formed by substituting the primary flow and small perturbations into the nonlinear incompressible Navier–Stokes equations and disregarding the second-order terms involving the perturbations,

$$\frac{\partial \hat{u}(x, y, t)}{\partial t} + U(y) \frac{\partial \hat{u}(x, y, t)}{\partial x} + \frac{dU(y)}{dy} \hat{v}(x, y, t) = -\frac{\partial \hat{p}(x, y, t)}{\partial x} + \frac{1}{Re} \nabla^2 \hat{u}(x, y, t), \quad (2.1)$$

$$\frac{\partial \hat{v}(x, y, t)}{\partial t} + U(y) \frac{\partial \hat{v}(x, y, t)}{\partial x} = -\frac{\partial \hat{p}(x, y, t)}{\partial y} + \frac{1}{Re} \nabla^2 \hat{v}(x, y, t), \quad (2.2)$$

$$\frac{\partial \hat{u}(x, y, t)}{\partial x} + \frac{\partial \hat{v}(x, y, t)}{\partial y} = 0, \quad (2.3)$$

where the flow variables are non-dimensionalized by the channel half-height, H , and centreline velocity, U_c . Re is the Reynolds number defined as $(U_c H / v)$ where v is the kinematic viscosity. By introducing a ‘stream function’, $\psi(x, y, t)$,

$$\hat{u}(x, y, t) \triangleq \frac{\partial \psi(x, y, t)}{\partial y} \quad (2.4)$$

and

$$\hat{v}(x, y, t) \triangleq -\frac{\partial \psi(x, y, t)}{\partial x}, \quad (2.5)$$

(2.1)–(2.3) may be combined into a single equation,

$$\frac{\partial}{\partial t} \frac{\partial^2 \psi}{\partial x^2} + \frac{\partial}{\partial t} \frac{\partial^2 \psi}{\partial y^2} = -U(y) \frac{\partial^3 \psi}{\partial x^3} - U(y) \frac{\partial}{\partial x} \frac{\partial^2 \psi}{\partial y^2} + \frac{d^2 U(y)}{dy^2} \frac{\partial \psi}{\partial x} + \frac{1}{Re} \nabla^2 (\nabla^2 \psi). \quad (2.6)$$

Assume periodic boundary conditions in the streamwise (x) direction. For channel flow, with rigid plates at $y = -1$ and $y = 1$, the no-slip boundary conditions become

$$\psi(x, y = -1, t) = 0, \quad (2.7)$$

$$\frac{\partial \psi}{\partial y}(x, y = -1, t) = 0, \quad (2.8)$$

$$\psi(x, y = 1, t) = 0, \quad (2.9)$$

$$\frac{\partial \psi}{\partial y}(x, y = 1, t) = 0. \quad (2.10)$$

With an initial condition

$$\psi(x, y, t = 0) = g(x, y) \quad (2.11)$$

the boundary value problem is completely formed. Existence and uniqueness of solutions for the linearized Navier–Stokes equations have been studied in Ladyzhenskaya (1969), Kreiss & Lorenz (1989), and Temam (1984). Equations (2.6)–(2.11) represent the starting point for construction of a feedback control system. These equations neither include any control terms nor do they describe any sensing of flow field variables.

2.2. Boundary input

We consider the case of blowing/suction at the lower wall of the channel. The boundary conditions are now modified from before to include boundary input, represented as the *known* separable function $q(t)w(x)f(y)$,

$$\psi(x, y = -1, t) = q(t)w(x)f(y = -1), \quad (2.12)$$

$$\frac{\partial \psi}{\partial y}(x, y = -1, t) = q(t)w(x) \frac{\partial f(y = -1)}{\partial y} = 0, \quad (2.13)$$

$$\psi(x, y = 1, t) = 0, \quad (2.14)$$

$$\frac{\partial \psi}{\partial y}(x, y = 1, t) = q(t)w(x) \frac{\partial f(y = 1)}{\partial y} = 0. \quad (2.15)$$

Note that these conditions constrain the function $f(y)$ such that

$$f(y = -1) \neq 0, \quad (2.16)$$

$$\frac{\partial f(y = -1)}{\partial y} = 0, \quad (2.17)$$

$$f(y = 1) = 0, \quad (2.18)$$

$$\frac{\partial f(y = 1)}{\partial y} = 0. \quad (2.19)$$

Many functions may be equally appropriate. One such function is

$$f(y) = \frac{1}{2}y^4 + \frac{1}{4}y^3 - y^2 - \frac{3}{4}y + 1. \quad (2.20)$$

In order to relate boundary conditions on ψ to blowing/suction in the wall-normal direction, we use (2.5) to relate $\widehat{v}(x, y, t)$ and $\psi(x, y, t)$. Then (2.12) becomes

$$\widehat{v}(x, y = -1, t) = -q(t) \frac{\partial w(x)}{\partial x} f(y = -1). \quad (2.21)$$

Note that $\widehat{v}(x, y, t)$ is related to the derivative of $w(x)$. The homogeneous equation (2.6) and the inhomogeneous boundary condition (2.12) can be converted into an inhomogeneous equation with homogeneous boundary conditions by introducing

$$\phi(x, y, t) \triangleq \psi(x, y, t) - q(t)f(y)w(x). \quad (2.22)$$

Then by substituting into (2.6), we obtain

$$\begin{aligned} \frac{\partial}{\partial t} \frac{\partial^2 \phi}{\partial x^2} + \frac{\partial}{\partial t} \frac{\partial^2 \phi}{\partial y^2} &= -U(y) \frac{\partial^3 \phi}{\partial x^3} - U(y) \frac{\partial}{\partial x} \frac{\partial^2 \phi}{\partial y^2} + \frac{d^2 U(y)}{dy^2} \frac{\partial \phi}{\partial x} + \frac{1}{Re} \frac{\partial^4 \phi}{\partial x^4} + 2 \frac{1}{Re} \frac{\partial^2}{\partial x^2} \frac{\partial^2 \phi}{\partial y^2} \\ &+ \frac{1}{Re} \frac{\partial^4 \phi}{\partial y^4} - \frac{\partial q(t)}{\partial t} \frac{\partial^2 w(x)}{\partial x^2} f(y) - \frac{\partial q(t)}{\partial t} w(x) \frac{\partial^2 f(y)}{\partial y^2} - q(t) \frac{\partial^3 w(x)}{\partial x^3} U(y) f(y) \\ &- q(t) \frac{\partial w(x)}{\partial x} U(y) \frac{\partial^2 f(y)}{\partial y^2} + q(t) \frac{\partial w(x)}{\partial x} \frac{d^2 U(y)}{dy^2} f(y) + \frac{1}{Re} q(t) \frac{\partial^4 w(x)}{\partial x^4} f(y) \\ &+ 2 \frac{1}{Re} q(t) \frac{\partial^2 w(x)}{\partial x^2} \frac{\partial^2 f(y)}{\partial y^2} + \frac{1}{Re} q(t) w(x) \frac{\partial^4 f(y)}{\partial y^4}. \end{aligned} \quad (2.23)$$

The boundary conditions in terms of ϕ are now

$$\phi(y = -1) = 0, \quad (2.24)$$

$$\frac{\partial \phi(y = -1)}{\partial y} = 0, \quad (2.25)$$

$$\phi(y = 1) = 0, \quad (2.26)$$

$$\frac{\partial \phi(y = 1)}{\partial y} = 0. \quad (2.27)$$

2.3. Boundary output

We use the streamwise component of shear at a single boundary point, $z(x_i, y = -1, t)$, as our boundary output, which is given by

$$z(x_i, y = -1, t) = \frac{\partial \widehat{u}(x_i, y = -1, t)}{\partial y}. \quad (2.28)$$

By expressing $\widehat{u}(x_i, y = -1, t)$ in terms of the stream function (2.4),

$$z(x_i, y = -1, t) = \frac{\partial^2 \psi(x_i, y = -1, t)}{\partial y^2}, \quad (2.29)$$

and by observing (2.22)

$$z(x_i, y = -1, t) = \frac{\partial^2 \psi(x_i, y = -1, t)}{\partial y^2} = \frac{\partial^2 \phi(x_i, y = -1, t)}{\partial y^2} + q(t) \frac{\partial^2 f(y = -1)}{\partial y^2} w(x_i). \quad (2.30)$$

3. Zeros, eigenvalues, and control-theoretic models

Linear stability analysis of (2.6) (Drazin & Reid 1981) shows that the system is linearly unstable for a range of Reynolds numbers. The goal of this paper is to

stabilize the system using control theory. To do this, we first transform the governing equations into special control-theoretic models.

3.1. System transfer function

We have defined a single-input/single-output (SISO) system in the sense that only one scalar function, $q(t)$, defines the entire input and one scalar function, $z(t)$, defines the output. A common form of control model for a finite-dimensional SISO system is the transfer function model. The transfer function, $H(s)$, is defined as the Laplace transform of the output, $z(t)$, divided by the Laplace transform of the input, $q(t)$, where zero initial conditions are assumed. Then

$$H(s) \triangleq \frac{\mathcal{L}[z(t)]}{\mathcal{L}[q(t)]} = \frac{Z(s)}{Q(s)}. \quad (3.1)$$

For finite-dimensional systems, $Z(s)$ and $Q(s)$ take the form of polynomials in the complex variable s . These polynomials may be factored to yield an equivalent representation,

$$H(s) \triangleq \frac{Z(s)}{Q(s)} = \frac{\prod_{j=1}^J (s - \zeta_j)}{\prod_{i=1}^I (s - p_i)}. \quad (3.2)$$

In this form, $p_1 \dots p_I$ are the *poles* of the system. The poles of any system are dependent solely on the physics of the underlying system, independent of any particular input or output. Unstable modes of the system appear as poles whose real part is greater than zero. As will be seen in later sections, the poles are closely related to the eigenvalues of the Orr-Sommerfeld equation. The values $\zeta_1 \dots \zeta_J$ are the *zeros* of the system. They are heavily dependent on which particular inputs and outputs are used on the system. As will be seen later, the position of these zeros will dictate sensor locations and will reveal the effect of feedback control on the eigenvalues. A graphical representation of the transfer function can be produced by plotting the poles and zeros in the complex s -space.

3.2. State-variable model

Much of modern control theory is based on the state-variable representation of a dynamic system. This representation relies on the basic fact that the motion of any finite-dimensional dynamic system may be expressed as a set of first-order ordinary differential equations. As a simple example of a state variable model (Franklin, Powell & Emami-Naeini 1988), Newton's law for a constant single mass, M , moving in one dimension, x , under a force, $F(t)$, is

$$M \frac{d^2x(t)}{dt^2} = F(t). \quad (3.3)$$

If we define one state variable as the position $x_1 \triangleq x(t)$ and the other state variable as the velocity $x_2 \triangleq dx(t)/dt$, (3.3) can be written as

$$\frac{dx_1}{dt} = x_2, \quad (3.4)$$

$$\frac{dx_2}{dt} = \frac{F(t)}{M}. \quad (3.5)$$

Furthermore, the first-order linear ordinary differential equations can be expressed using matrix notation

$$\begin{bmatrix} \frac{dx_1}{dt} \\ \frac{dx_2}{dt} \end{bmatrix} = \begin{bmatrix} 0 & 1 \\ 0 & 0 \end{bmatrix} \begin{bmatrix} x_1 \\ x_2 \end{bmatrix} + \begin{bmatrix} 0 \\ 1 \end{bmatrix} \frac{F}{M} \quad (3.6)$$

or

$$\frac{dx}{dt} = Ax + Bq. \quad (3.7)$$

If we take output as position, x_1 ,

$$z = [1 \ 0] \begin{bmatrix} x_1 \\ x_2 \end{bmatrix} \quad (3.8)$$

or

$$z = C \cdot x \quad (3.9)$$

The matrix A , and the vectors B and C are called the state space matrices of the single-input, single-output (SISO) system. More specifically, the A matrix is referred to as the dynamic matrix of the system. It can be shown that the poles of the system are simply the eigenvalues of the A matrix. In the more general case of multiple-input, multiple-output (MIMO) systems, B and C are matrices. For generality, we may add another term, Dq , to the output equation to account for systems in which there is direct feedthrough from the input to the output. Then,

$$z = C \cdot x + Dq \quad (3.10)$$

In the case of no direct feedthrough, $D = 0$, the state space and transfer function models are related as

$$H(s) \triangleq \frac{Z(s)}{Q(s)} = C(sI - A)^{-1}B. \quad (3.11)$$

3.3. State-space formulation for channel system

We will convert our problem into a set of first-order ordinary differential equations and then form a state-space model from these equations. The state-space model can then be represented with transfer function poles and zeros. We will proceed in this way for two reasons. First, our system lends itself to decomposition into first-order ordinary-differential equations by use of a Galerkin method. More importantly, however, the state-space model lends itself to extremely elegant ways to control eigenvalues of a system in well prescribed ways. It should be noted that unlike the single-mass example given above, the channel system requires an infinite number of ordinary differential equations to describe its motion. This is known as an infinite-dimensional system. As a result, any finite number of ordinary-differential equations used in a state-space model will not completely describe the system. The difficulties associated with such a system are taken up after a discussion of the Galerkin method used to obtain the ordinary-differential equations.

3.3.1. First-order system

We use a standard Galerkin procedure to convert the governing partial differential equation (2.23) into a system of ordinary-differential equations. Assume an

approximate solution of (2.23) as

$$\phi_a(x, y, t) \triangleq \sum_{n=-N}^N \sum_{m=0}^M a_{nm}(t) P_n(x) \Gamma_m(y). \quad (3.12)$$

By using Fourier functions, e^{inx_0x} , for $P_n(x)$ and basis functions constructed from Chebyshev polynomials for $\Gamma_m(y)$ (Joshi 1996), we obtain a first-order system. Define inner products in the streamwise (x) and normal (y) directions respectively:

$$[e^{inx_0x}, e^{imx_0x}]_x \triangleq \frac{1}{L} \int_{-L/2}^{L/2} e^{inx_0x} e^{-imx_0x} dx = \delta_{mn}, \quad \alpha_0 \triangleq \frac{2\pi}{L}, \quad (3.13)$$

and

$$[\Gamma_m(y), \Gamma_n(y)]_y \triangleq \int_{-1}^1 \frac{\Gamma_n(y) \Gamma_m(y)}{(1-y^2)^{1/2}} dy, \quad (3.14)$$

where L is the non-dimensional length of the finite-length channel. Applying the orthogonality of the basis functions in x , we obtain a system of first-order ordinary differential equations:

$$\begin{aligned} & - \sum_{m=0}^M \frac{\partial a_{lm}(t)}{\partial t} l^2 \alpha_0^2 \beta_{mk}^0 + \sum_{m=0}^M \frac{\partial a_{lm}(t)}{\partial t} \beta_{mk}^2 = \sum_{m=0}^M a_{lm}(t) il^3 \alpha_0^3 \beta_{mk}^{0+} - \sum_{m=0}^M a_{lm}(t) il \alpha_0 \beta_{mk}^{2+} \\ & + \sum_{m=0}^M a_{lm}(t) il \alpha_0 \beta_{mk}^{0-} + \frac{1}{Re} \sum_{m=0}^M a_{lm}(t) l^4 \alpha_0^4 \beta_{mk}^0 - 2 \frac{1}{Re} \sum_{m=0}^M a_{lm}(t) l^2 \alpha_0^2 \beta_{mk}^2 \\ & + \frac{1}{Re} \sum_{m=0}^M a_{lm}(t) \beta_{mk}^4 + \frac{\partial q(t)}{\partial t} \{S_{lk}^1\} + q(t) \{S_{lk}^2\}, l = -N \dots N, k = 0 \dots M, \end{aligned} \quad (3.15)$$

where

$$S_{lk}^1 \triangleq - \left[\frac{\partial^2 w(x)}{\partial x^2}, P_l(x) \right]_x [v(y), \Gamma_k(y)]_y - [w(x), P_l(x)]_x \left[\frac{\partial^2 v(y)}{\partial y^2}, \Gamma_k(y) \right]_y \quad (3.16)$$

and

$$\begin{aligned} S_{lk}^2 \triangleq & - \left[\frac{\partial^3 w(x)}{\partial x^3}, P_l(x) \right]_x [U(y)v(y), \Gamma_k(y)]_y - \left[\frac{\partial w(x)}{\partial x}, P_l(x) \right]_x \left[U(y) \frac{\partial^2 v(y)}{\partial y^2}, \Gamma_k(y) \right]_y \\ & + \left[\frac{\partial w(x)}{\partial x}, P_l(x) \right]_x \left[\frac{d^2 U(y)}{dy^2} v(y), \Gamma_k(y) \right]_y + \frac{1}{Re} \left[\frac{\partial^4 w(x)}{\partial x^4}, P_l(x) \right]_x [v(y), \Gamma_k(y)]_y \\ & + 2 \frac{1}{Re} \left[\frac{\partial^2 w(x)}{\partial x^2}, P_l(x) \right]_x \left[\frac{\partial^2 v(y)}{\partial y^2}, \Gamma_k(y) \right]_y + \frac{1}{Re} [w(x), P_l(x)]_x \left[\frac{\partial^4 v(y)}{\partial y^4}, \Gamma_k(y) \right]_y. \end{aligned} \quad (3.17)$$

In this system, α_0 is the fundamental wavenumber in the x -direction, defined as $2\pi/L$, and the β coefficients are defined in terms of the following scalar products, where the $\Gamma(y)$ are the basis functions in y :

$$\beta_{mk}^j \triangleq \left[\frac{\partial^j \Gamma_m(y)}{\partial y^j}, \Gamma_k(y) \right]_y, \quad j = 0 \dots 4, \quad (3.18)$$

$$\beta_{mk}^{0+} \triangleq [U(y)\Gamma_m(y), \Gamma_k(y)]_y, \quad (3.19)$$

$$\beta_{mk}^{0-} \triangleq \left[\frac{d^2 U(y)}{dy^2} \Gamma_m(y), \Gamma_k(y) \right]_y, \quad (3.20)$$

$$\beta_{mk}^{2+} \triangleq \left[U(y) \frac{\partial^2 \Gamma_m(y)}{\partial y^2}, \Gamma_k(y) \right]_y. \quad (3.21)$$

3.3.2. Transformation to state-space form

We may visualize (3.15) in block matrix form as

$$\begin{aligned} & \begin{bmatrix} M_{-N} & 0 & \cdots & 0 \\ 0 & M_{-N+1} & 0 & 0 \\ 0 & 0 & \ddots & 0 \\ 0 & 0 & 0 & M_N \end{bmatrix} \begin{bmatrix} \frac{d\tilde{a}_{l=-N}}{dt} \\ \frac{d\tilde{a}_{l=-N+1}}{dt} \\ \vdots \\ \frac{d\tilde{a}_{l=N}}{dt} \end{bmatrix} \\ &= \begin{bmatrix} K_{-N} & 0 & \cdots & 0 \\ 0 & K_{-N+1} & 0 & 0 \\ 0 & 0 & \ddots & 0 \\ 0 & 0 & 0 & K_N \end{bmatrix} \begin{bmatrix} \tilde{a}_{l=-N} \\ \tilde{a}_{l=-N+1} \\ \vdots \\ \tilde{a}_{l=N} \end{bmatrix} + \begin{bmatrix} Y_1 & Y_2 \end{bmatrix} \begin{bmatrix} q(t) \\ \frac{dq(t)}{dt} \end{bmatrix} \quad (3.22) \end{aligned}$$

where $\tilde{a}_{l=p}$ denotes a column vector of all a_{lk} coefficients whose first index, l , is the value p . In compact notation,

$$M \frac{da}{dt} = \mathbf{Ka} + [Y_1 \quad Y_2] \begin{bmatrix} q(t) \\ \frac{dq(t)}{dt} \end{bmatrix}. \quad (3.23)$$

Assuming non-singularity of the M matrix, we may invert to obtain

$$\frac{da}{dt} = M^{-1} \mathbf{Ka} + [M^{-1} Y_1 \quad M^{-1} Y_2] \begin{bmatrix} q(t) \\ \frac{dq(t)}{dt} \end{bmatrix} \quad (3.24)$$

where a , K , Y_1 and Y_2 are all complex. By expanding in terms of real and imaginary parts, we obtain

$$\begin{aligned} \frac{da_R}{dt} + i \frac{da_I}{dt} &= M^{-1} K_R a_R + i M^{-1} K_I a_R + i M^{-1} K_R a_I - M^{-1} K_I a_I \\ &\quad + M^{-1} Y_{1R} q(t) + i M^{-1} Y_{1I} q(t) + M^{-1} Y_{2R} \frac{dq(t)}{dt} + i M^{-1} Y_{2I} \frac{dq(t)}{dt}. \quad (3.25) \end{aligned}$$

where the subscript R or I indicates real or imaginary parts. Define

$$\tilde{p} \triangleq \begin{bmatrix} a_R \\ a_I \\ q(t) \end{bmatrix}. \quad (3.26)$$

Then the state space system is

$$\frac{d\tilde{p}}{dt} = \begin{bmatrix} M^{-1} K_R & -M^{-1} K_I & M^{-1} Y_{1R} \\ M^{-1} K_I & M^{-1} K_R & M^{-1} Y_{1I} \\ 0 & 0 & 0 \end{bmatrix} \tilde{p} + \begin{bmatrix} M^{-1} Y_{2R} \\ M^{-1} Y_{2I} \\ 1 \end{bmatrix} \frac{dq(t)}{dt} \quad (3.27)$$

We write (3.27) as

$$\frac{d\tilde{p}}{dt} = \mathbf{A}\tilde{p} + \mathbf{B}\frac{dq(t)}{dt} \triangleq \mathbf{A}\tilde{p} + \mathbf{B}u(t) \quad (3.28)$$

where the input to the system is $dq(t)/dt$. Note since $q(t)$ in (2.12) is related to physical blowing/suction, it is important to keep in mind that the input to this model is the derivative of $q(t)$. In physical terms, any input derived from this model will be in terms of $dq(t)/dt$ and therefore must be integrated before it can be applied as physical blowing/suction.

3.3.3. Measurement equations

By observing (2.30) and using the assumed solution form (3.12)

$$\begin{aligned} z(x_i, y = -1, t) &= \frac{\partial^2 \psi(x_i, y = -1, t)}{\partial y^2} = \frac{\partial^2 \phi}{\partial y^2} + q(t) \frac{\partial^2 f(y = -1)}{\partial y^2} w(x_i) \\ &= \sum_{n=-N}^N \sum_{m=0}^M a_{nm}(t) P_n(x_i) \frac{\partial^2 \Gamma_m(y = -1)}{\partial y^2} + q(t) \frac{\partial^2 f(y = -1)}{\partial y^2} w(x_i) + \rho(t, x_i, y = -1) \end{aligned} \quad (3.29)$$

where $\rho(t, x_i, y = -1)$, the residual component of streamwise shear due to the truncated expansion, is assumed to be negligible compared to the two other terms. The second term on the right-hand side of (3.29) is made up of the known input terms (2.12). Denote

$$D \triangleq \frac{\partial^2 f(y = -1)}{\partial y^2} w(x_i). \quad (3.30)$$

By pulling out the complex time coefficients and denoting them as the vector α as above we may construct a complex observation matrix, \mathbf{O}

$$z(x_i, y = -1, t) = \mathbf{O}\alpha + Dq(t). \quad (3.31)$$

Finally, by creating \tilde{p} by stacking the real and imaginary parts of α , as well as $q(t)$, we may construct an observation equation in state-variable form

$$\begin{bmatrix} z_R(x_i, y = -1, t) \\ z_I(x_i, y = -1, t) \end{bmatrix} = \begin{bmatrix} \mathbf{O}_R & -\mathbf{O}_I & D \\ \mathbf{O}_I & \mathbf{O}_R & 0 \end{bmatrix} \tilde{p}. \quad (3.32)$$

Since we may measure only real output (shear), we are left with only the top half of the observation matrix,

$$z_R(x_i, y = -1, t) = [\mathbf{O}_R \quad -\mathbf{O}_I \quad D] \tilde{p}. \quad (3.33)$$

In order to describe the system in traditional control terms, define

$$\mathbf{C} \triangleq [\mathbf{O}_R \quad -\mathbf{O}_I \quad D]. \quad (3.34)$$

Then,

$$z_R(x_i, y = -1, t) = \mathbf{C}\tilde{p} \quad (3.35)$$

3.3.4. Initial conditions

We have not accounted for the initial value (2.11) in our boundary value problem. We may account for the initial condition by assuming it can be written as a series expansion in terms of $P_n(x)$ and $\Gamma_m(y)$. Then

$$\begin{aligned} \phi(x, y, t = 0) &= \psi(x, y, t = 0) - s(t = 0)f(y)w(x) = g(x, y) - s(t = 0)f(y)w(x) \\ &= \sum_{n=-N}^N \sum_{m=0}^M b_{nm} P_n(x) \Gamma_m(y) \end{aligned} \quad (3.36)$$

where b_{nm} are assumed known. Then

$$\mathbf{a}(t = 0) = \mathbf{b}. \quad (3.37)$$

Since \mathbf{a} and \mathbf{b} are both complex, stack the real and imaginary components to arrive at an initial condition on $\tilde{\mathbf{p}}$:

$$\tilde{\mathbf{p}}(t = 0) = \begin{bmatrix} b_R \\ b_I \\ q(t = 0) \end{bmatrix}. \quad (3.38)$$

We have now defined the system completely in the state-variable form of (3.7), (3.9) where \mathbf{A} and \mathbf{B} are given in (3.28), \mathbf{C} is given in (3.35), and the initial condition is (3.38). Although we have shown the state-space formulation using a single input and a single output, we may formulate the multiple input/multiple output case similarly. In that case, the multiple input functions are represented as a *sum* of separable functions in (2.12) and multiple outputs are represented as a vector whose components are of the form (3.35). It should be noted that in the multiple input case, it is important for physical implementation that for any finite stretch in the x -direction, only one of the multiple input functions is non-zero.

4. Infinite-dimensional nature of the channel problem and effect on actuator design

In a system described by partial-differential equations, such as the channel flow problem, no finite-dimensional model will capture all the dynamics of the system. Such a system is called infinite-dimensional. By examining the Galerkin approximate solution (3.12), we see that the approximate solution can converge only as $N, M \rightarrow \infty$. This would result in an infinite number of ordinary differential equations. Each n value included in the approximate solution is referred to as adding an additional wavenumber in the dynamic model. Even for just one wavenumber, $n = N$ (say), we see the assumed Galerkin solution requires an infinite number of terms in the y -direction,

$$\phi_a(x, y, t) \triangleq \sum_{m=0}^{M \rightarrow \infty} a_{Nm}(t) P_N(x) \Gamma_m(y). \quad (4.1)$$

Interestingly, by examining the structure of the \mathbf{A} matrix in the resulting state-space model, we see that the dynamics associated with each individual wavenumber are decoupled from the others. This is characterized by a block diagonal form of the \mathbf{A} matrix, (4.2). As a result, we may separate the problem of determining system poles into a set of smaller problems that include only one wavenumber at a time:

$$\mathbf{A} = \begin{bmatrix} [\mathbf{A}_{(n=1)}] & 0 & \cdots & \infty \\ 0 & [\mathbf{A}_{(n=2)}] & 0 & 0 \\ 0 & 0 & \ddots & 0 \\ \infty & 0 & 0 & [\mathbf{A}_{(n=\infty)}] \end{bmatrix}. \quad (4.2)$$

Indeed, the eigenvalues (poles) of the entire \mathbf{A} matrix are simply the eigenvalues (poles) of each smaller \mathbf{A} matrix block. Offsetting this computational advantage, however, is the fact that the locations of the zeros are not decoupled by wavenumber. Therefore, even though the poles of the system can be calculated separately using only one wavenumber in a particular computation, the zeros of the system force all

the wavenumbers in the model to be considered together. This can easily be seen from an examination of the transfer functions associated with just two wavenumbers. Consider two transfer functions obtained by using two distinct wavenumbers and the same input, $u(t)$, and output, $z(t)$:

$$H_{(n=1)} = \frac{N_{(n=1)}(s)}{D_{(n=1)}(s)}, \quad H_{(n=2)} = \frac{N_{(n=2)}(s)}{D_{(n=2)}(s)}. \quad (4.3)$$

The roots of $N(s)$ are the zeros and the roots of $D(s)$ are the poles. In terms of input and output,

$$z = H_{(n=1)}u, \quad z = H_{(n=2)}u. \quad (4.4)$$

Considered together, however,

$$z = [H_{(n=1)} + H_{(n=2)}]u = \left[\frac{D_{(n=2)}(s)N_{(n=1)}(s) + D_{(n=1)}(s)N_{(n=2)}(s)}{D_{(n=1)}(s)D_{(n=2)}(s)} \right] u. \quad (4.5)$$

The poles of the new, combined transfer function are clearly those of each model separately. The zeros, however, are the roots of a completely new polynomial $D_{(n=2)}(s)N_{(n=1)}(s) + D_{(n=1)}(s)N_{(n=2)}(s)$, which, in general, has little to do with either of the original numerators.

We have seen that an infinite expansion is needed to fully model the channel system. Since in practice an infinite expansion cannot be used to create a state-space model, we will always have some part of the system dynamics that is unmodelled. Furthermore, we have seen that the \mathbf{A} (dynamic) matrix may be decoupled by wavenumber.

Consider a partition of the state-space model as

$$\frac{dx}{dt} = \begin{bmatrix} \frac{dx_m}{dt} \\ \frac{dx_u}{dt} \end{bmatrix} = \begin{bmatrix} \mathbf{A}_m & 0 \\ 0 & \mathbf{A}_u \end{bmatrix} \begin{bmatrix} x_m \\ x_u \end{bmatrix} + \begin{bmatrix} \mathbf{B}_m \\ \mathbf{B}_u \end{bmatrix} u(t), \quad (4.6)$$

$$z = [C_m \ C_u]x, \quad (4.7)$$

where the subscripts m and u represent the modelled and unmodelled parts of the system. In the channel flow problem, the unmodelled part is meant to denote only the dynamics of wavenumbers left out of the finite-dimensional model. Note that both \mathbf{A}_u and \mathbf{A}_m are of infinite dimension; \mathbf{A}_u because of the infinite number of wavenumbers left out of the reduced-order model and \mathbf{A}_m because of the infinite number of expansion functions needed in y for each of the finite number of modelled wavenumbers. One way to avoid considering unmodelled wavenumber dynamics is to ensure that the control input, $u(t)$, has no effect whatsoever on the unmodelled wavenumber dynamics. In terms of the state-space model (4.6), this is equivalent to rendering $\mathbf{B}_u = 0$. This is known as making the unmodelled wavenumber dynamics uncontrollable. By examining (3.27), we see that the \mathbf{B} matrix is formed from terms of S_{lk}^1 in (3.16). If $w(x)$ in (3.16) is such that $S_{lk}^1 = 0$, then those components of the \mathbf{B} matrix are zero. Equivalently, we must ensure that the projection of $w(x)$ onto the unmodelled wavenumbers is zero. Owing to the orthogonality of Fourier components, we select $w(x)$ to be made up of modelled Fourier components only.

5. Single-wavenumber channel model

Consider the channel model shown in figure 1. The total non-dimensional length of the channel, L , is 4π . In this case, the fundamental wavenumber, $\alpha_0 = 0.5$. Only one

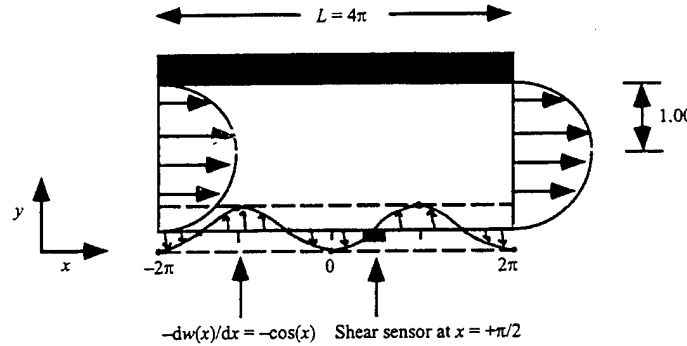


FIGURE 1. System model for Poiseuille flow. Input is applied along the bottom plate as $w(x) = \sin(x)$ and shear is measured at $x = \pi/2$ with $Re = 10000$ and $\alpha = 1.0$.

wavenumber is included in the model, corresponding to $\alpha = l\alpha_0 = 1.00$. The Reynolds number is chosen as $Re = 10000$. Input is distributed along the bottom plate with a sinusoidal weighting function in order to render the unmodelled wavenumber dynamics uncontrollable as described in §4. In terms of the input function, $w(x)$, see (2.12)

$$w(x) = \sin(x). \quad (5.1)$$

Note that the physical blowing/suction, $\hat{v}(x, y, t)$, takes the form

$$\hat{v}(x, y, t) = -q(t) \frac{\partial w(x)}{\partial x} f(y = -1) = -q(t) \cos(x) f(y = -1) \quad (5.2)$$

see (2.21). This type of input may be achieved in practice by a large number of independently controllable actuators that are distributed along the lower channel wall. The $f(y)$ function is chosen as in (2.20). The sensor location is $x = +\frac{1}{2}\pi$. In order to visualize the control-theoretic model, the system \mathbf{A} , \mathbf{B} , and \mathbf{C} matrices are transformed to transfer function form, $H(s)$. Figure 2 shows the locations of the poles and zeros in the s -plane for the single-wavenumber model.

5.1. Relation of poles to eigenvalues of the Orr-Sommerfeld equation

Poles of the transfer function or, equivalently, eigenvalues of the \mathbf{A} matrix are closely related to the eigenvalues of the Orr-Sommerfeld equation. Assume a solution of (2.6) of the form

$$\psi(x, y, t) \triangleq \beta(y) e^{ixx} e^{-i\alpha ct}. \quad (5.3)$$

By substituting into (2.6), we obtain the familiar Orr-Sommerfeld equation in the normal-mode form,

$$[U(y) - c] \left(\frac{\partial^2 \beta(y)}{\partial y^2} - \alpha^2 \beta(y) \right) - \frac{\partial^2 U(y)}{\partial y^2} \beta(y) = \frac{1}{i\alpha Re} \left[\frac{\partial^4 \beta(y)}{\partial y^4} - 2\alpha^2 \frac{\partial^2 \beta(y)}{\partial y^2} + \alpha^4 \beta(y) \right]. \quad (5.4)$$

Here, the Reynolds number, Re , is known; the wavenumber, α , is assumed real and known; the complex wave speed, c , is the eigenvalue of the problem; and the function $\beta(y)$ is the eigenvector of the problem. Stability of a flow for a given value of Re and α is determined by the imaginary part of c . If the imaginary part is positive, the solution (5.3) becomes an unbounded exponential and flow is unstable. Poles of the

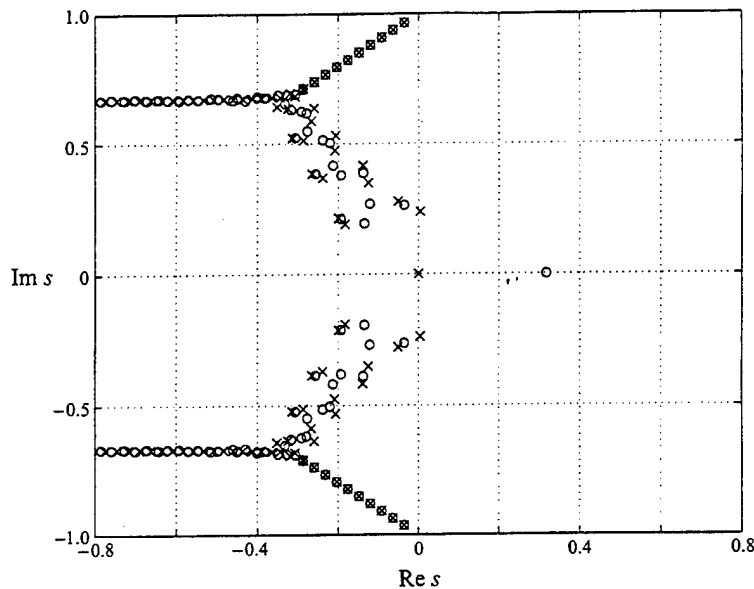


FIGURE 2. Pole (\times) and zero (\circ) configuration for the system model of figure 1. Note that all poles and zeros appear in complex-conjugate pairs. Each pair of complex-conjugate poles represents one mode of the system. One pair of poles is to the right of the imaginary axis. This indicates the system has one unstable mode. Note that the single pole at the origin represents a built-in integrator due to $u(t) = dq(t)/dt$. Channel model: $Re = 10000$, shear sensor at $\pi/2, w(x) = \sin(x)$, $L = 4\pi$, $\alpha = 1.0$.

transfer function in the Laplace domain at $s = p_i$ correspond to solutions in the time domain of $e^{p_i t}$. As a result, we observe that poles of the transfer function are related to eigenvalues of the Orr-Sommerfeld equation as

$$p_i \equiv -i\alpha c. \quad (5.5)$$

In order to validate our linear code, we compare our poles to eigenvalues produced in Orszag (1971). Orszag (1971) obtained Orr-Sommerfeld eigenvalues for the channel problem with $\alpha = 1.00$ and $Re = 10000$. He reported only one slightly unstable eigenvalue at $s = 0.00373967 + i0.23752649$ ($c = 0.23752649 - i0.00373967$). The eigenvalue is seen as unstable by its positive real part. We obtained identical results including the one unstable mode at

$$s = 0.00373967 \mp i0.23752649.$$

All other stable modes obtained in the present study are identical to those reported in Orszag (1971). The goal of our control system will be to move these unstable poles into the stable half of the s -plane or, equivalently, make sure the controlled-system poles all have real parts less than zero.

5.2. Verification of model zeros

Verification of the system zeros is more difficult due to the fact that no published results exist to our knowledge. We use the channel code simulation used in Kim, Moin & Moser (1987) to verify our zeros. This code is a spectral channel flow code which uses periodic boundary conditions. Consider the transfer function model (3.2)

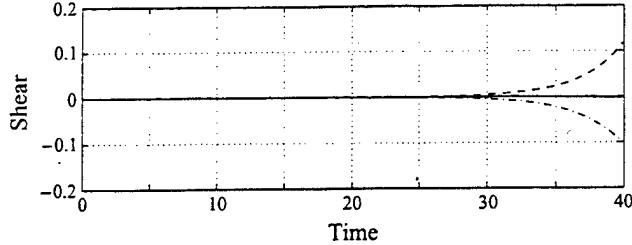


FIGURE 3. Output from the Navier-Stokes simulation with input applied as $u(t) = e^{+0.317557t}$. Although an unbounded input is applied, near zero output is observed at sensor location $\pi/2$ (solid curve). Sensor location 0 (dashed curve) and sensor location π (dash-dot curve) do not show zero output. Channel model: $Re = 10000$, shear sensor at $\pi/2$, $w(x) = \sin(x)$, $L = 4\pi$, $\alpha = 1.0$.

with $J = 1$ and $I = 1$:

$$H(s) = \frac{Z(s)}{U(s)} = \frac{(s - \zeta_1)}{(s - p_1)}. \quad (5.6)$$

In the Laplace domain,

$$sZ(s) - p_1 Z(s) = sU(s) - \zeta_1 U(s). \quad (5.7)$$

Assuming zero initial conditions and transforming into the time domain, (5.7) becomes

$$\frac{dz(t)}{dt} - p_1 z(t) = \frac{du(t)}{dt} - \zeta_1 u(t) \quad (5.8)$$

where $z(t)$ is the output function and $u(t)$ is the input function. If the input is taken as

$$u(t) = e^{\zeta_1 t} \quad (5.9)$$

then the right-hand side of (5.8) becomes zero and the system behaves as if zero input has been applied. As a result, $z(t)$ remains zero for all time. Therefore, we may verify zeros of the system by applying non-zero input in special ways and observing zero output. Note from figure 2 that for sensor location $x = +\frac{1}{2}\pi$, one zero exists in the right half plane at $s = +0.317557 + 0i$. This represents an ideal zero to check as this corresponds to an unbounded, unstable input. Figure 3 shows output from the Navier-Stokes simulation with input $u(t) = dq(t)/dt = e^{+0.317557t}$. Note that even though an unbounded, exponentially growing input is applied to the system, near zero output is observed at the sensor, thus verifying that ζ_1 is indeed a zero of the system. This is contrasted with measurements at different sensor locations that grow rapidly. With a sensor at a different location, the zeros of the system change position so zero output is no longer expected for this particular input. Absolute zero is not observed at sensor location $x = \frac{1}{2}\pi$ due to slight numerical inaccuracies in the model.

6. Feedback control and stabilization

At this point, with the construction of a valid state-variable model, any number of control schemes may be employed to stabilize the system. A general control system is shown in figure 4. The output of the system is fed into a controller. The output of the controller is then used to create an input to the system. The design of a controller that achieves certain system characteristics is the goal of control system design. Several

modern control techniques may be applied that require a state-variable model. In this paper, the primary goal will be system stability. For this purpose, a simple constant gain feedback with integral compensator will be shown to be sufficient.

6.1. Constant gain feedback with integral compensator

Figure 5 shows an integral compensator feedback control scheme. K is referred to as the gain of the feedback. The output of the system, in this case shear, is multiplied by a feedback gain, integrated in time, and then fed back as blowing and suction at the input. Note that the integrator is required because of the structure of the input given in (3.27), i.e. the input is taken as the derivative of suction/blowing. The signal, $r(t)$, is called the reference signal. It is used to define the desired output. In our case, we would like the shear output, $z(x_i, y = -1, t)$, to be zero. Therefore, we set $r(t)$ to zero. Then

$$u(t) \triangleq \frac{\partial q(t)}{\partial t} = -K z(x_i, y = -1, t). \quad (6.1)$$

Therefore, assuming $q(0) = 0$,

$$q(t) = -K \int_0^t z(x_i, y = -1, \tau) d\tau \quad (6.2)$$

and by observing (2.21), we may describe physical blowing and suction at the boundary:

$$\hat{v}(x, y = -1, t) = -q(t) \frac{\partial w(x)}{\partial x} f(y = -1) = K \cos(x) \int_0^t z(x_i, y = -1, \tau) d\tau \quad (6.3)$$

As defined earlier,

$$H(s) \triangleq \frac{\mathcal{L}[z(t)]}{\mathcal{L}[u(t)]} = \frac{Z(s)}{U(s)}. \quad (6.4)$$

Therefore,

$$Z(s) = H(s)U(s). \quad (6.5)$$

In the absence of feedback, one mode is unstable. Also, one pole exists at the origin for the integrator. Consider a new transfer function from the reference input, $r(t)$, to the output, $z(t)$, in the presence of feedback:

$$u(t) = r(t) - K z(t). \quad (6.6)$$

By taking the Laplace transform of (6.6),

$$U(s) = R(s) - K Z(s). \quad (6.7)$$

Then

$$Z(s) = H(s)[R(s) - K Z(s)]. \quad (6.8)$$

Finally,

$$\frac{Z(s)}{R(s)} = \frac{H(s)}{1 - KH(s)}. \quad (6.9)$$

The new poles of the feedback system are defined by

$$1 - KH(s) = 0. \quad (6.10)$$

As K gets larger and larger, it is clear that the poles of the new system tend toward the zeros of $H(s)$. In this way, modes of the system can sometimes be changed to

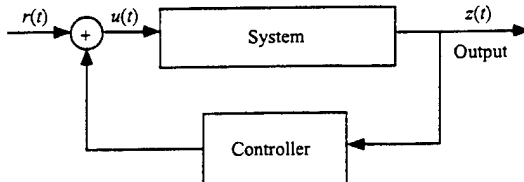


FIGURE 4. Feedback control. The output of the system is fed into a controller and then to the input.

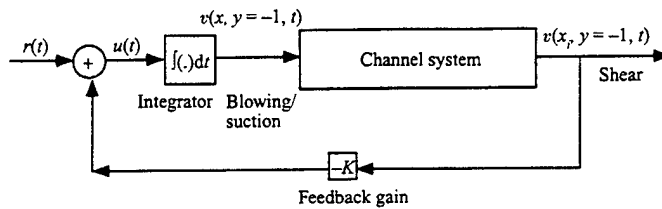


FIGURE 5. Feedback control for channel system. The output of the system is multiplied by a feedback gain, integrated in time, and then fed back at the input. The reference signal, $r(t)$, equals 0.

form a stable system (Franklin *et al.* 1988). Unstable modes that appear as poles on the right hand side of the complex s -plane and 'marginally stable' poles on the $\text{Im}(s)$ -axis are drawn to the left-hand side by applying feedback.

6.2. Sensor placement

We have seen that, by applying feedback, poles of the system will eventually be drawn to zeros of the system. In the channel flow system of figure 2, any feedback will cause either the pole at the origin (integrator pole) or the unstable mode poles to be drawn to the zero on the real axis in the right-hand plane, thus making the system unstable to a greater degree. Therefore, finding a transfer function that has all zeros in the left-hand plane becomes an important objective. The poles of the system are independent of sensing or actuation. However, the zeros of the system are dependent on both the type and location of sensing and the type and location of actuation. Figure 6 shows the pole/zero configuration for the channel model with the shear sensor at three different locations. Only the top half of the s -plane is shown since the bottom half is a mirror image projected across the real axis as shown in figure 2. The poles of all the models are in the same location as expected. However, the zeros are different in all three cases. In figures 6(a) and 6(b), we observe a lone zero in the right-hand s -plane. However, when the sensor is placed at $x = +\pi$, figure 6(c) shows all zeros in the left-hand plane. In fact, there is a region around $x = \pi$ that results in all zeros in the left-hand plane. By placing a shear sensor at $x = \pi$, simple feedback with integral compensation will allow stabilization with the proper value of gain, K . In the case of sensor locations that result in right-hand-plane, so called 'non-minimum phase', zeros stabilization is still possible. However, more complex controllers (Bryson & Ho 1975; Ogata 1990) must be designed that are beyond the scope of this paper.

6.3. Root locus analysis and numerical simulation

One way to visualize how system poles will change as the feedback gain, K , changes is to construct a root locus plot. This is a plot of all poles of a system as the feedback

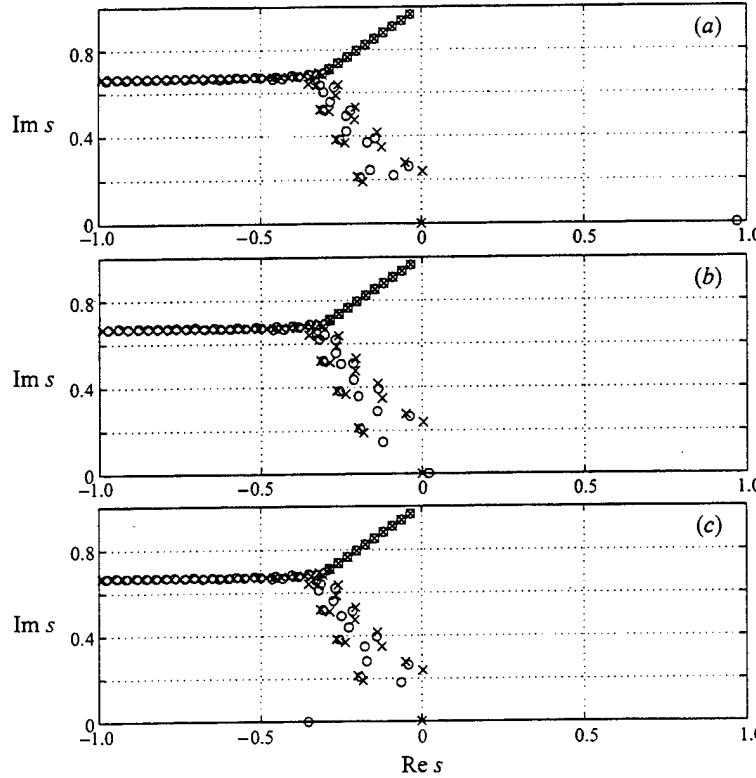


FIGURE 6. Pole (\times)/zero (\circ) configuration. Channel model: $Re = 10000$, $w(x) = \sin(x)$, $L = 4\pi$, $\alpha = 1.0$. Only the top half of the s -plane is shown. Shear sensor at (a) $\pi/4$ (b) $3\pi/4$, (c) π .

gain varies from $K = 0$ to $K = \infty$. Figure 7 shows such a plot for the system shown in figure 6(c). When K reaches ≈ 1 , all feedback system poles (closed-loop-poles) lie on the left-hand plane and no instabilities exist in the new feedback system. Numerical results obtained from the Navier-Stokes simulation for the new feedback controlled system are shown in figure 8. The computation is carried out without feedback until $t = 50$, after which the feedback is turned on. We see that the growing instability is quickly suppressed. At the instant the controller is turned on, the simulation shows a high transient response due to the non-continuous nature of the input at that time instant. In terms of the state space defined in (3.28), (3.35),

$$\frac{d\tilde{p}}{dt} = \mathbf{A}\tilde{p} + \mathbf{B}u(t), \quad (6.11)$$

$$z(x_i, y = -1, t) = \mathbf{C}\tilde{p}, \quad (6.12)$$

$$u(t) = -\mathbf{K}z(x_i, y = -1, t). \quad (6.13)$$

Then, in a closed loop,

$$\frac{d\tilde{p}}{dt} = \mathbf{A}\tilde{p} - \mathbf{B}(\mathbf{K}z(x_i, y = -1, t)) \quad (6.14)$$

$$= \mathbf{A}\tilde{p} - \mathbf{B}\mathbf{K}\mathbf{C}\tilde{p} = (\mathbf{A} - \mathbf{B}\mathbf{K}\mathbf{C})\tilde{p} \quad (6.15)$$

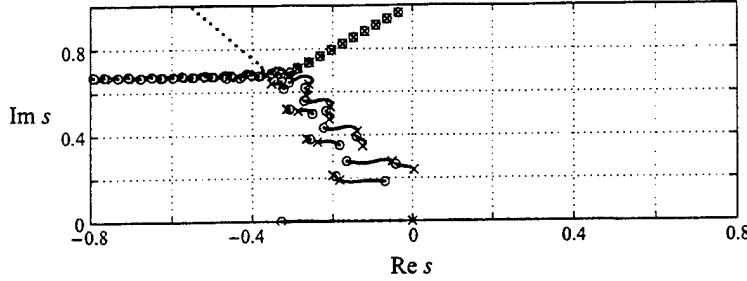


FIGURE 7. Root locus plot for channel system with input as in the channel model (figure 1) and shear output at $x = \pi$. The poles start at the open-loop poles shown with 'x's. As K increases, they start to move toward the location of the system zeros, shown as 'o's. The pole at position $s = (0,0)$ moves directly to the left. The unstable pole moves quickly to a position just to the left of the imaginary axis. Near $0.7 < y < 1.0$, $-0.6 < x < -0.4$, we see a pole moving towards a zero that is out of the range of this figure. Channel model: $Re = 10\,000$, shear sensor at π , $w(x) = \sin(x)$, $L = 4\pi$, $\alpha = 1.0$. Only the top half of the s -plane is shown.

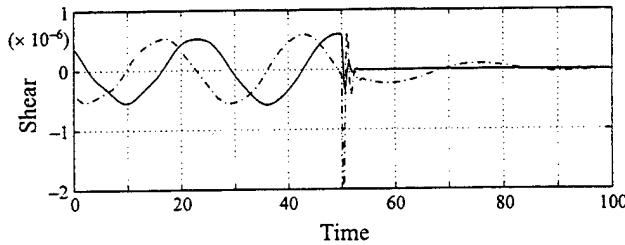


FIGURE 8. Navier-Stokes simulation of feedback control. Shear is multiplied by a feedback gain, integrated, and fed back into the input. Channel model: $Re = 10\,000$, feedback shear sensor at π , $w(x) = \sin(x)$, $L = 4\pi$, $\alpha = 1.0$. Curve 1 (solid) shows shear at location π ; curve 2 (dot-dash) shows shear at location $\pi/2$.

The solution to this equation is

$$\tilde{p}(t) = e^{(A-BKC)t} \tilde{p}(t=0). \quad (6.16)$$

This solution will approach zero as $t \rightarrow \infty$ since the eigenvalues of $A - BKC$ (closed-loop poles) are all stable.

6.4. Robustness in the presence of Reynolds number uncertainty

A major advantage of feedback control systems is their robustness to system uncertainty. From a practical point of view, Reynolds numbers may not be known exactly or may change frequently as in the flight of an airplane, for example. Figure 9 shows the open-loop pole/zero configurations for systems with varying Reynolds numbers. Note that these systems start with all zeros in the left-hand s -plane. A root locus analysis shows that a feedback system with $K = 0.1$ stabilizes both systems. Indeed, a feedback gain of $K = 0.1$ stabilizes systems for a wide range of Reynolds numbers from $Re = 1000$ to $Re = 40\,000$. Figure 10 shows the least-stable pole in both the controlled and uncontrolled systems for several Reynolds numbers. Recall that a pole with real part less than zero is stable. We see near $Re = 5772$, an unstable pole appears in the open-loop (uncontrolled) system. Unstable eigenvalues continue to exist in the open-loop system until

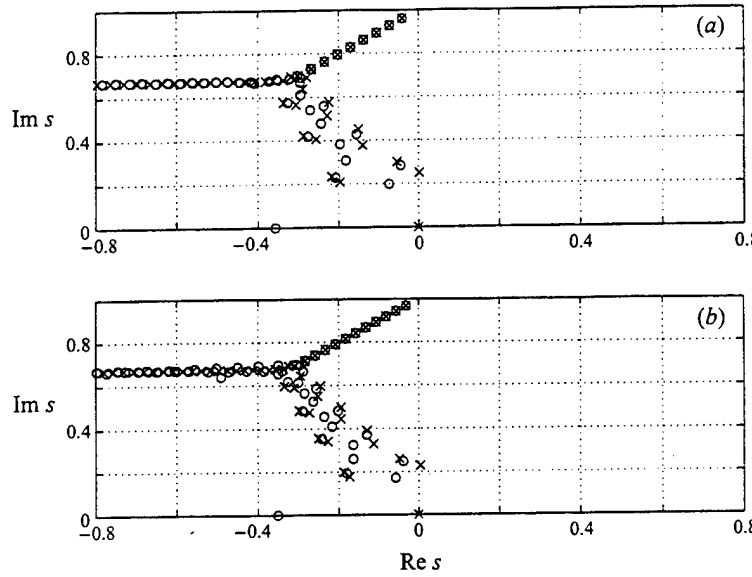


FIGURE 9. Pole (\times)/zero (\circ) configuration. Channel model: shear sensor at π , $w(x) = \sin(x)$, $L = 4\pi$, $\alpha = 1.0$. Only the top half of the s -plane is shown. (a) $Re = 7500$, (b) $Re = 12500$.

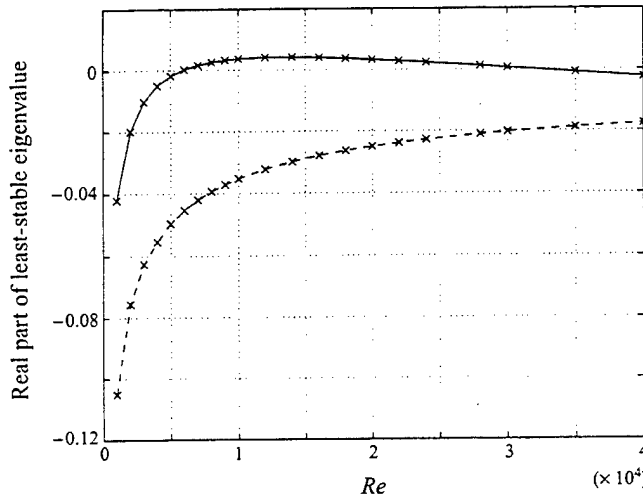


FIGURE 10. Real part of least-stable pole for open-loop (solid line) and closed-loop (dashed line) channel system with $1000 \leq Re \leq 40000$. Shear sensor at π , $w(x) = \sin(x)$, $L = 4\pi$, $\alpha = 1.0$. Data points are shown as \times 's.

$30000 \leq Re \leq 35000$. An identical feedback controller, with gain $K = 0.1$, however, stabilizes the system for Reynolds numbers in the range $1000 \leq Re \leq 40000$. Clearly, the feedback controller is extremely robust to changes in Reynolds number.

7. Unobservable transient response as a path of bypass transition

Recently, some authors (Trefethen *et al.* 1993; Butler & Farrell 1992; Farrell 1988; Henningson 1994) have suggested a possible path of bypass transition in Poiseuille flow that is caused by high transient response due to the non-self-adjointness of the evolution matrix. This high-transient behaviour is due to the non-orthogonality of the eigenmodes and not caused by any single mode, but rather a combination of many modes. In this section, we suggest a possible different form of bypass transition in a controlled system due to a single mode. In the presence of any type of control, it is possible that energy from an input is fed into a mode such that the mode is reinforced during the transient period before it eventually dies out. During the transient period, however, the mode may grow to an amplitude large enough to trigger nonlinear effects that induce transition to turbulence. This may be a possible path of bypass transition in a controlled system.

Single modes may be characterized in linear systems in terms of modal controllability and modal observability. Modal controllability implies that a particular mode may be affected by the actuators chosen (blowing/suction in our case). Modal observability implies that a particular mode may be measured by the sensors chosen (shear in our case). A particular mode may be non-observable, non-controllable, or both. This will be seen in §§7.1 and 7.2. If high-transient modes are controllable and observable, control theory may be used to suppress them. However, if high-transient modes are unobservable, the high transients will never be seen and feedback control cannot be used to suppress them.

7.1. Modal canonical form

The state-space formulation provides an excellent framework for assessing the reinforcement of each mode individually. Consider an n -dimensional state space with scalar input and output

$$\frac{dx}{dt} = Ax + Bu, \quad (7.1)$$

$$z = Cx. \quad (7.2)$$

We may perform a similarity transformation on the system to produce a new state-space representation with the same input-output relationship, but with a different interpretation of the state variables. Let

$$P \triangleq [v_1 \ v_2 \ \dots \ v_n] \quad (7.3)$$

where v_j is the j th eigenvector of the A matrix and n is the dimension of the A matrix. A new representation is constructed as (Grace *et al.* 1992; Kailath 1980)

$$\frac{d\tilde{x}}{dt} = P^{-1}AP\tilde{x} + P^{-1}Bu, \quad (7.4)$$

$$z = CP\tilde{x} \quad (7.5)$$

where $\tilde{x} \triangleq P^{-1}x$. The new representation is written as

$$\frac{d\tilde{x}}{dt} = \tilde{A}\tilde{x} + \tilde{B}u, \quad (7.6)$$

$$z = \tilde{C}\tilde{x} \quad (7.7)$$

where the real eigenvalues of the original A matrix appear on the diagonal of \tilde{A} and the complex eigenvalues appear in a 2×2 block on the diagonal of \tilde{A} . For an A

matrix with eigenvalues $(\alpha_1, \sigma \pm j\omega, \alpha_2)$, the $\tilde{\mathbf{A}}$ matrix is

$$\tilde{\mathbf{A}} = \begin{bmatrix} \alpha_1 & 0 & 0 & 0 \\ 0 & \sigma & \omega & 0 \\ 0 & -\omega & \sigma & 0 \\ 0 & 0 & 0 & \alpha_2 \end{bmatrix}. \quad (7.8)$$

In this form, each state-variable pair represents a mode of the system. Furthermore, the modes are block decoupled so that each mode is represented by the 2×2 system

$$\begin{bmatrix} \frac{d\tilde{x}_1}{dt} \\ \frac{d\tilde{x}_2}{dt} \end{bmatrix} = \begin{bmatrix} \sigma & \omega \\ -\omega & \sigma \end{bmatrix} \begin{bmatrix} \tilde{x}_1 \\ \tilde{x}_2 \end{bmatrix} + \begin{bmatrix} \tilde{b}_1 \\ \tilde{b}_2 \end{bmatrix} u, \quad (7.9)$$

$$z_1 = [\tilde{c}_1 \quad \tilde{c}_2] \begin{bmatrix} \tilde{x}_1 \\ \tilde{x}_2 \end{bmatrix}, \quad (7.10)$$

where $\omega, \sigma, \tilde{b}_1, \tilde{b}_2, \tilde{c}_1$, and \tilde{c}_2 are all scalars. This is known as the modal canonical state-space form. All modes can be monitored directly for high-transient reinforcement in this form.

7.2. Modal observability and controllability

It is easy to see that if \tilde{b}_1 and \tilde{b}_2 are zero, no input can affect the mode and the mode is uncontrollable. Similarly, if \tilde{c}_1 and \tilde{c}_2 are zero, then the motion of \tilde{x}_1 and \tilde{x}_2 cannot be measured at the output, z_1 , and the mode is unobservable. In terms of stabilization, an uncontrollable mode is not problematic as long as it is stable. However, if an unstable mode is uncontrollable, nothing can be done to stabilize it. Observability may be a problem even if modes are stable. If an unobservable mode is highly amplified by control energy, no attempt could be made to suppress it since it would not be observed at the output. In terms of poles and zeros, uncontrollable or unobservable modes both show up as pole/zero cancellations in the complex s -plane. As can be seen from figure 2, many poles and zeros for the channel system lie on top of each other, indicating that certain modes in the system are either uncontrollable, unobservable, or both. Although a mode may not be physically observable at the output, the modal canonical formulation allows us to numerically observe the state evolution of each mode directly. In this way, we may assess the risk of highly amplified modes triggering bypass transition. This is done for the controlled system simulated in figure 8. The uncontrolled linear system is simulated with an initial condition for 200 time steps at which time a feedback controller with gain $K = 0.1$ is turned on. Figure 11 shows the state evolution of the modes with poles at $s = -0.1474 \pm 0.8514i$ and $s = -0.3252 \pm 0.6361i$ as well as the state evolution of the one unstable mode.[†] In addition, figure 11(a) shows the shear measurement at the output. We see that the unstable mode dies out quickly as soon as the feedback is turned on. In addition, the mode at $s = -0.1474 \pm 0.8514i$ gains almost no energy after the feedback is activated. This indicates that the mode is not a bypass mode. The mode at $s = -0.3252 \pm 0.6361i$ is seen to gain a lot of energy after the controller is started. Indeed, the amplitude of the transient response is nearly twice that of the unstable mode. This represents a possible bypass mode since such an amplitude

[†] Note that amplitudes shown as a result of linear system simulations should only be used for comparison with each other since the linear model has been scaled to unity open-loop feedforward gain, i.e. $H(s) = \kappa Z(s)/U(s)$ where $\kappa = 1$.

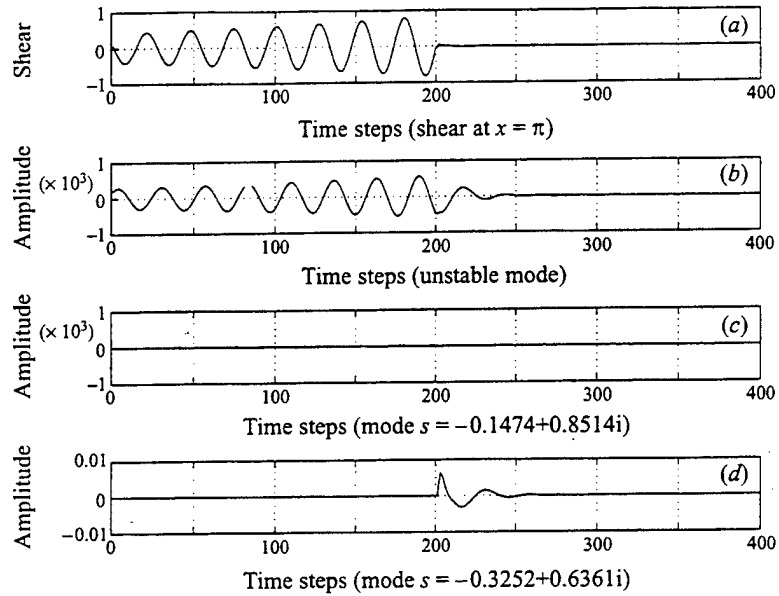


FIGURE 11. Linear model state evolution of system modes with control applied at $t = 200$: (a) measured shear, (b) the state evolution of the unstable mode, (c) the state evolution of the mode at $s = -0.1474 + 0.8514i$, (d) the state evolution of the mode at $s = -0.3252 + 0.6361i$. Channel model: $Re = 10\,000$, shear sensor at π , $w(x) = \sin(x)$, $L = 4\pi$, $\alpha = 1.0$.

may force the system into the nonlinear region where transition to turbulence may be triggered. Furthermore, the high energy nature of the mode cannot be observed at the shear sensor since this mode is unobservable. This can be seen from the plot of the shear sensor output. Modal un-observability is also suggested by noting the relatively low $\tilde{\epsilon}_1$ and $\tilde{\epsilon}_2$ values of 0.5155, -0.1131 compared to the $\tilde{\epsilon}_1$ and $\tilde{\epsilon}_2$ values of -162.85, 234.66 for the unstable mode, which is clearly seen at the output. Fortunately, the high energy nature of the mode does not lead to a bypass transition in this case. This is verified by the Navier-Stokes simulation in figure 8, which shows no nonlinear effects. If the instability were allowed to grow to a higher amplitude before the controller was applied, however, the highly amplified mode in the transient response might have triggered nonlinear effects.

8. Multiple instability control

Although most work has focused on suppression of single instabilities, more realistic models should include multiple wavenumbers. Indeed, for a given Reynolds number, an infinite number of wavenumbers exist. Each wavenumber contributes its own poles and zeros to the control-theoretic model. Consider a model with non-dimensional channel length 20π , where input is applied as $w(x) = \sin(x) + \sin(0.9x)$. In this model, wavenumbers of 0.9 and 1.0 are included. Both wavenumbers lead to unstable modes. The pole/zero configuration of this new two-wavenumber model with shear sensor at π is shown in figure 12(a). Note that in comparison to the one-wavenumber model, more poles and zeros exist. The original one-wavenumber model contained one 'fork' structure of poles, while the two-wavenumber model contains two 'fork'

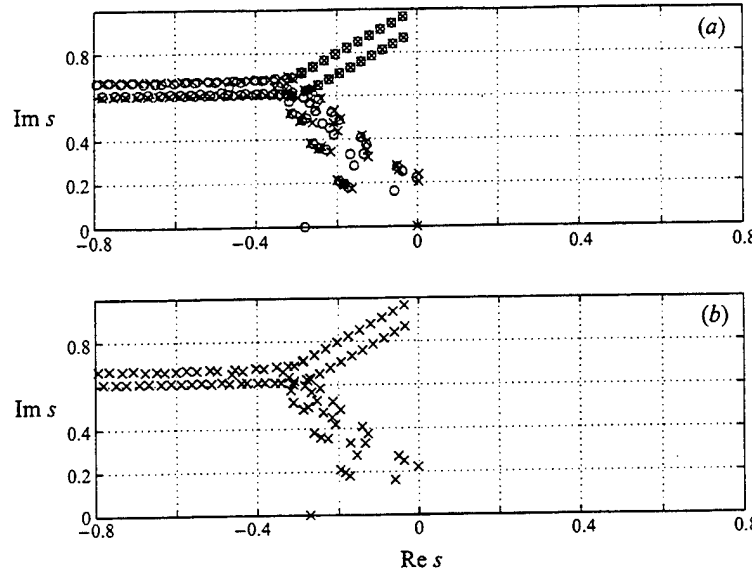


FIGURE 12. (a) Pole (x) and zero (o) configuration of channel system of length 20π , including wavenumbers of 0.90 and 1.00. $Re = 10000$, shear sensor at π , $w(x) = \sin(x) + \sin(0.9x)$. Only the top half of the s -plane is shown. (b) Same as (a) but showing closed-loop poles after feedback with gain $K = 0.1$.

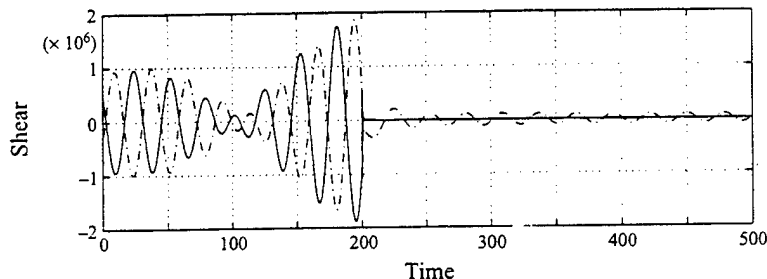


FIGURE 13. Navier-Stokes simulation of channel system of length 20π , including wavenumbers of 0.90 and 1.00. $Re = 10000$, feedback shear sensor at π , $w(x) = \sin(x) + \sin(0.9x)$, feedback gain $K = 0.1$. Curve 1 (solid) shows shear at location π ; curve 2 (dash-dot) shows shear at location 2π .

structures. It can be visualized that in a model with several wavenumbers, several 'forks' will stack on top of each other in the s -plane. Near $s = i0.2$ are two unstable poles in the right-hand plane that represent the two unstable modes in the system. As seen before, all zeros lie in the left hand s -plane. Figure 12(b) shows the closed-loop poles after feedback with gain $K = 0.1$. Results from the Navier-Stokes simulation are shown in figure 13. The computation is carried out without feedback until $t = 200$. A combination of two growing waves is seen at the shear sensor. At $t = 200$, feedback with integral compensation is applied and the system is stabilized.

9. Effect of linear controllers on two-dimensional finite-amplitude disturbances

The critical Reynolds number above which linear instabilities exist in plane Poiseuille flow is $Re \approx 5772$. Below this Reynolds number, Poiseuille flow is linearly stable. However, transition from laminar to turbulent flow occurs in experiments at much lower Reynolds numbers, typically around $Re = 1000$. Moreover, even for super-critical Reynolds number flows, linear instabilities predict extremely slow growth rates. In practice, transition occurs orders of magnitude more quickly. Therefore, linear stability alone does not dictate transition. Transition to turbulence is generally accepted to be a nonlinear three-dimensional phenomenon. In previous sections, we constructed two-dimensional linear controllers based on the two-dimensional linearized Navier-Stokes equations. By applying these controllers to plane Poiseuille flow with infinitesimal two-dimensional disturbances, we saw that we may linearly stabilize the system so that the flow could no longer support those disturbances. If we apply our linear controllers to flows that contain finite-amplitude disturbances, we can no longer use linear analysis to describe the flow dynamics as nonlinear terms become relevant. However, the application of a controller based on linear analysis does change the nonlinear system.

Many authors (Orszag & Patera 1983; Bayly, Orszag & Herbert 1988) have explored the effect of two-dimensional finite-amplitude disturbances on three-dimensional infinitesimal disturbances in plane Poiseuille flow. Above $Re \approx 2900$, for two dimensions, stable non-attenuating finite-amplitude equilibria exist in plane Poiseuille flow. Below $Re \approx 2900$, non-decaying, finite-amplitude equilibria do not exist. However, in flows with $1000 \leq Re \leq 2900$, the timescale for decay is so large that the flow may be considered in 'quasi-equilibrium'. It has been shown that in the presence of such two-dimensional finite-amplitude disturbances, infinitesimal three-dimensional disturbances are highly unstable and may cause transition in shear flows. Figure 14 shows the energy of a single-wavenumber, two-dimensional finite-amplitude disturbance ($\alpha = 1.0$) and a single-wavenumber-pair, three-dimensional infinitesimal disturbance ($\alpha = 1.0, \beta = \mp 1.0$) obtained through direct numerical simulation at $Re = 3000$. The maximum amplitude of the two-dimensional finite-amplitude disturbance is $0.1 U_c$. At this Reynolds number, wavenumber, and initial energy level, we see the two-dimensional finite-amplitude disturbance decaying slowly. The three-dimensional disturbance, on the other hand, is seen to rapidly gain energy. Orszag & Patera (1983) show that the two-dimensional instability acts as a mediator for transfer of energy from the mean flow to the three-dimensional disturbance, but does not directly provide energy. The growth rate of the three-dimensional disturbance is orders of magnitude larger than that of the Orr-Sommerfeld instabilities.

Orszag & Patera show, in the case where $Re \leq 1000$, that the attenuation of finite-amplitude two-dimensional disturbances is large enough that three-dimensional disturbances do not become unstable. The fact that high attenuation of the two-dimensional finite-amplitude disturbance prevented three-dimensional instability below $Re \approx 1000$ suggests that if controllers can be created that speed up the attenuation of the finite-amplitude two-dimensional disturbance for flows with Reynolds numbers greater than 1000, three-dimensional instability may be eliminated. We have seen in §6 that linear controllers did stabilize infinitesimal two-dimensional disturbances. Figure 15 shows the effects of the linear controller of §6 when applied to a system with the same finite-amplitude two-dimensional disturbance and infinitesimal three-dimensional disturbance shown in figure 14. The linear controller

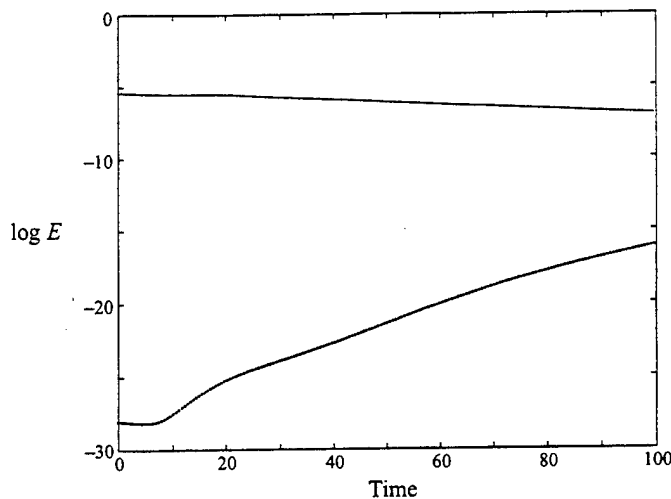


FIGURE 14. Energy of a two-dimensional finite-amplitude disturbance ($\alpha = 1.0$) and a three-dimensional infinitesimal disturbance ($\alpha = 1.0, \beta = \mp 1.0$) for $Re = 3000$. Solid line represents the total energy of the two-dimensional finite-amplitude disturbance and the dotted line represents that of the three-dimensional infinitesimal disturbance.

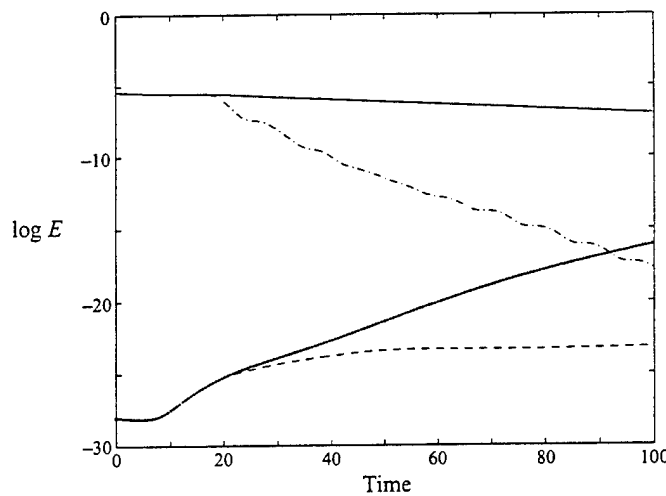


FIGURE 15. Effect of linear controller when applied at $t = 15$ for $Re = 3000$. The top two lines show the two-dimensional finite-amplitude disturbance without (solid) and with (dash-dot) linear control. We see at $t = 15$ that the controlled two-dimensional finite-amplitude disturbance is highly damped. The bottom two lines show the infinitesimal three-dimensional disturbance without (dot) and with (dashed) linear control. That without controller gains energy quickly, while that with controller quickly fails to gain energy.

dramatically increased the attenuation of the finite-amplitude two-dimensional disturbance. As a result, the infinitesimal three-dimensional disturbance was rendered stable. Clearly, the linear controller not only stabilized the two-dimensional linear system, but also had a stabilizing effect on the three-dimensional nonlinear system. These results show the promise of linear controllers even in nonlinear systems.

10. Conclusions

In this paper, we have developed feedback controllers that linearly stabilize plane Poiseuille flow. We used a Galerkin spectral method to generate state-space models. Indeed, any (convergent) numerical method that reduces the governing partial differential equations into a set of ordinary-differential equations may be used. It is important to note, however, that the meaning of the state variables in the state-space model changes as different numerical methods are employed. Even though state variables may not have any specific physical meaning, some numerical methods may result in favourable divisions of system dynamics. In the plane Poiseuille flow case, the spectral Galerkin method with the use of Fourier components in the x -direction and combination-Chebyshev polynomials in the y -direction led to modelled dynamics that were de-coupled by wavenumber. This led to a block diagonal form of the A matrix. As a result, we were clearly able to describe modelled and unmodelled dynamics in terms of wavenumber dynamics included and not included in our finite-dimensional model. This also led us to the concept of using distributed control to render certain wavenumbers 'uncontrollable'. If other numerical methods had been used, this concept would not have been so transparent. Furthermore, plane Poiseuille flow can be linearly stabilized with simple feedback controllers if sensors are placed at judicious locations. Both the position and the type of sensing and actuation change the zeros of single-input/single-output models. In our case, we have seen that certain shear sensor locations lead to 'minimum-phase' systems and some locations lead to 'non-minimum phase' systems. Minimum-phase systems are in general easier to control than non-minimum phase systems. As a result, we were able to stabilize plane Poiseuille flow with a constant gain feedback, integral compensator controller. In addition, the controller was extremely robust to a wide range of Reynolds numbers. Also, we have shown that one danger of feedback control is that the linear transient response of a controlled system can lead to high amplitudes for a short period of time. If these amplitudes are high enough, it is possible that they may invalidate the linear model and enhance nonlinear effects. Furthermore, the high transients may not be observable at the output so that feedback control cannot be used to suppress them. Finally, we have shown that linear controllers have a strong stabilizing effect on two-dimensional finite-amplitude disturbances. As a result, three-dimensional secondary instabilities can be rendered stable.

This research was performed under grant number F49620-93-1-0332 from the United States Air Force. The authors would like to thank Professors J. S. Gibson and Robert Kelly of the UCLA Mechanical and Aerospace engineering department for many helpful discussions and suggestions. The authors are also grateful to Mr. Jaisig Choi who performed the computations presented in §9. Computer resources have been provided by the NAS program at NASA Ames Research Center.

REFERENCES

- BAYLY, B. J., ORSZAG, S. A. & HERBERT, T. 1988 Instability mechanisms in shear-flow transition. *Ann. Rev. Fluid Mech.* **20**, 359–391.
- BERINGEN, S. 1984 Active control of transition by periodic suction and blowing. *Phys. Fluids* **27**, 1345–1348.
- BOWER, W. W., KEGELMAN, J. I. & PAL, A. 1987 A numerical study of two-dimensional instability-wave control based on the Orr-Sommerfeld equation. *Phys. Fluids* **30**, 998–1004.
- BRYSON, A. E. JR. & HO, T.-C. 1975 *Applied Optimal Control*. Taylor and Francis.
- BURNS, J. A. & OU Y.-R. 1994 Feedback control of the driven cavity problem using LQR designs. *Proc. 33rd Conf. on Decision and Control, December, 1994*, pp. 289–294.
- BUTLER, K. M. & FARRELL, B. F. 1992 Three-dimensional optimal perturbations in viscous shear flows. *Phys. Fluids A* **4**, 1637–1650.
- CHOI, H., MOIN, P. & KIM, J. 1994 Active turbulence control for drag reduction in wall bounded flows. *J. Fluid Mech.* **262**, 75–110.
- DRAZIN, P. G. & REID, W. H. 1981 *Hydrodynamic Stability*. Cambridge University Press.
- FARRELL, B. F. 1988 Optimal perturbations in viscous shear flows. *Phys. Fluids* **31**, 2093–2102.
- FRANKLIN, G., POWELL, J. D. & EMAMI-NAEINI, A. 1988 *Feedback Control of Dynamic Systems*. Addison-Wesley.
- GRACE, A., LAUB, A. J., LITTLE, J. N. & THOMPSON, C. M. 1992 *Control System Toolbox: For use with MATLAB*. The Math Works.
- GUNZBURGER, M. D., HOU, L. & SVOBODNY, T. 1992 Boundary velocity control of incompressible flow with an application to viscous drag reduction. *SIAM J. Control Optimization* **30**, 167–181.
- HENNINGSON, D. S. 1994 Bypass transition – Proceedings from a Mini-workshop. *Tech. Rep.* Royal Institute of Technology, Department of Mechanics, S-100,44, Stockholm, Sweden.
- JOSHI, S. S. 1996 A systems theory approach to the control of plane Poiseuille flow. PhD thesis, UCLA, Department of Electrical Engineering.
- JOSLIN, R. D., ERLEBACHER, G. & HUSSAINI, M. Y. 1994 Active control of instabilities in laminar boundary layer flow- Part I: An overview. *ICASE Rep. 94-97*. NASA Langley Research Center, Hampton, VA.
- KAILATH, T. 1980 *Linear Systems*. Prentice-Hall.
- KIM, J., MOIN, P. & MOSER, R. 1987 Turbulence statistics in fully developed channel flow at low Reynolds numbers. *J. Fluid Mech.* **177**, 133–166.
- KREISS, H.-O. & LORENZ, J. 1989 *Initial Boundary Value Problems and the Navier-Stokes Equations*. Academic.
- LADYZHENSKAYA, O. A. 1969 *The Mathematical Theory of Viscous Incompressible Flow*. Gordon and Breach.
- NOSENCHUCK, D. M. 1982 Passive and active control of boundary layer transition. PhD thesis, California Institute of Technology.
- OGATA, K. 1990 *Modern Control Engineering*. Prentice-Hall.
- ORR, W. M'F. 1907 The stability or instability of the steady motions of a perfect liquid and of a viscous liquid. *Proc. R. Irish Acad. A* **27**, 9–68.
- ORSZAG, S. A. 1971 Accurate solution of the Orr Sommerfeld stability equation. *J. Fluid Mech.* **50**, 689–703.
- ORSZAG, S. A. & PATERA, A. T. 1983 Secondary instability of wall-bounded shear flows. *J. Fluid Mech.* **128**, 347–385.
- REED, H. L. & NAYFEH, A. H. 1986 Numerical perturbation technique for stability of flat plate boundary layer with suction. *AIAA J.* **24**.
- SCHUBAUER, G. B. & SKRAMSTAD, H. K. 1947 Laminar boundary layer oscillations and stability of laminar flow. *J. Aeronaut. Sci.* **14**, 68–78.
- SOMMERFELD, A. 1908 Ein Beitrag zur hydrodynamicischen Erklaerung der turbulenten Flues-sigkeitsbewegungen. *Proc. 4th Intl Congress of Mathematics*, Vol. III, pp. 116–124.
- TEMAM, R. 1984 *Navier-Stokes Equations*. North-Holland.
- TREFETHEN, L. N., TREFETHEN, A. E., REDDY, S. C. & DRISCOLL, T. A. 1993 Hydrodynamic stability without eigenvalues. *Science* **261**, 578–584.

Appendix 4

LETTERS

The purpose of this Letters section is to provide rapid dissemination of important new results in the fields regularly covered by Physics of Fluids. Results of extended research should not be presented as a series of letters in place of comprehensive articles. Letters cannot exceed four printed pages in length, including space allowed for title, figures, tables, references and an abstract limited to about 100 words. There is a three-month time limit, from date of receipt to acceptance, for processing Letter manuscripts. Authors must also submit a brief statement justifying rapid publication in the Letters section.

A linear process in wall-bounded turbulent shear flows

John Kim^{a)} and Junwoo Lim

*Department of Mechanical and Aerospace Engineering, University of California, Los Angeles,
California 90095-1597*

(Received 11 January 2000; accepted 12 April 2000)

A linear process in wall-bounded turbulent shear flows has been investigated through numerical experiments. It is shown that the linear coupling term, which enhances non-normality of the linearized Navier-Stokes system, plays an important role in fully turbulent—and hence, nonlinear—flows. Near-wall turbulence is shown to decay without the linear coupling term. It is also shown that near-wall turbulence structures are not formed in their proper scales without the nonlinear terms in the Navier-Stokes equations, thus indicating that the formation of the commonly observed near-wall turbulence structures are essentially nonlinear, but the maintenance relies on the linear process. Other implications of the linear process are also discussed. © 2000 American Institute of Physics. [S1070-6631(00)00708-X]

The transient growth due to non-normality of the eigenmodes of the linearized Navier-Stokes (N-S) equations has received much attention during the past several years (see, for example, Refs. 1–3). It has been shown that the energy of certain disturbances can grow to $\mathcal{O}(\text{Re}^2)$ in time proportional to $\mathcal{O}(\text{Re})$, where Re denotes Reynolds number of the flow.² It has been postulated that this transient growth, which is a linear process, can lead to transition to turbulence at a Reynolds number smaller than the critical Reynolds number, below which a classical linear stability theory based on the modal analysis predicts that all small disturbances decay asymptotically. As such, some investigators attributed this linear process as a possible cause for subcritical transition in some wall-bounded shear flows, such as plane Poiseuille flow and Couette flow.

Some investigators further postulated that the same linear process is also responsible for the observed wall-layer streaky structures in turbulent boundary layers.^{1,4} The optimal disturbance, which has the largest transient growth according to their optimal perturbation theory, looks similar to the near-wall streamwise vortices that create the streaky structures in turbulent boundary layers. However, this optimal disturbance occupies the entire boundary layer, in contrast to the streamwise vortices in turbulent boundary layers, which are confined to the near-wall region. In order to relate their optimal perturbation theory to those structures observed in turbulent boundary layers, a time scale corresponding to the bursting process in turbulent boundary layers, which is essentially a nonlinear process, was introduced as an additional parameter.⁴ It has been argued that the transient growth in turbulent boundary layers would be disrupted by turbulent motions on a time scale corresponding to the bursting process, which is smaller than the viscous time scale, and

hence, the globally optimal disturbance will never have a chance to grow to its maximum possible amplitude. The notion that commonly observed wall-layer structures are related to a linear process, although it is the nonlinear process that determines the proper length scale, suggests that the same linear process may play an important role in fully nonlinear turbulent boundary layers.

Other evidence that a linear process may play an important role in turbulent boundary layers can be found in the work of Joshi *et al.*^{5,6} and others,^{7,8} who successfully applied controllers developed based on a liner system theory to the nonlinear flow in their attempt to reduce the viscous drag in turbulent boundary layers. Bewley⁹ applied linear optimal control theory to a nonlinear convection problem. Although it is not clear how controllers based on a linearized model work so well for nonlinear flows and it is a subject of further investigation, these results suggest that the essential dynamics of near-wall turbulence may well be approximated by a linear model.

Motivated by the above findings, we investigate the role of this linear process in fully nonlinear turbulent flows. In particular, we investigate the role of the linear coupling term (see below for its definition), which is a source of the non-normality of the eigenmodes of the linearized Navier-Stokes equations, in wall-bounded shear flows, using a turbulent channel flow as an example.

In this Letter, we shall use (x, y, z) for the streamwise, wall-normal, and spanwise coordinates, respectively, and (u, v, w) for the corresponding velocity components. Reynolds number, Re_τ , is based on the wall-shear velocity, $u_\tau = \sqrt{\tau_w/\rho}$, and the channel half-width, h , where $\tau_w = \nu dU/dy|_w$ is the mean shear stress at the wall, and U , ν , and ρ denote the mean velocity, viscosity, and density, re-

spectively. The superscript “+” denotes quantities nondimensionalized by ν and u_τ .

Representing the wall-normal velocity, v , and the wall-normal vorticity, ω_y , in terms of Fourier modes in the streamwise (x) and the spanwise (z) directions, the linearized N-S equations can be written in an operator form

$$\frac{d}{dt} \begin{bmatrix} \hat{v} \\ \hat{\omega}_y \end{bmatrix} = [A] \begin{bmatrix} \hat{v} \\ \hat{\omega}_y \end{bmatrix}, \quad (1)$$

where

$$[A] = \begin{bmatrix} L_{os} & 0 \\ L_c & L_{sq} \end{bmatrix}, \quad (2)$$

and the hat denotes a Fourier-transformed quantity. Here L_{os} , L_{sq} , and L_c represent the Orr-Sommerfeld, Squire, and the coupling operators, respectively, and defined as

$$\begin{aligned} L_{os} &= \Delta^{-1}(-ik_x U \Delta + ik_x (d^2 U / dy^2) + (1/\text{Re}) \Delta^2), \\ L_{sq} &= -ik_x U + (1/\text{Re}) \Delta, \\ L_c &= -ik_z (dU/dy), \end{aligned} \quad (3)$$

where k_x and k_z are the streamwise and spanwise wave numbers, respectively, $k^2 = k_x^2 + k_z^2$, $\Delta = \partial^2 / \partial y^2 - k^2$, and U is the mean velocity about which the N-S equations are linearized. Note that the full nonlinear N-S equations can be written also as

$$\frac{d}{dt} \begin{bmatrix} \hat{v} \\ \hat{\omega}_y \end{bmatrix} = [A] \begin{bmatrix} \hat{v} \\ \hat{\omega}_y \end{bmatrix} + \begin{bmatrix} \mathcal{N}_v \\ \mathcal{N}_{\omega_y} \end{bmatrix}, \quad (4)$$

where all nonlinear terms are lumped into \mathcal{N}_v and \mathcal{N}_{ω_y} . The operator A in this case, however, is a function of v and ω_y , because U depends on v and ω_y .

It has been shown that operator A in Eq. (2) is non-normal, and hence, its eigenmodes are nonorthogonal, thus allowing a transient growth of energy even if all individual modes are stable and decay asymptotically.^{1,3} Note that the coupling term L_c vanishes for two-dimensional (2-D) disturbances ($k_z = 0$), and therefore, there is no coupling between v and ω_y for 2-D disturbances. For 3-D disturbances, however, v evolves independently, but ω_y is forced by v through the coupling term. It should be noted that L_{os} itself is not self-adjoint, and hence, 2-D disturbances can have a transient growth, but it was shown that 3-D disturbances have much larger transient growth due to the coupling term, which causes larger non-normality. In the present study, we concentrate on the role of the coupling term in fully nonlinear turbulent flows, using a fully developed turbulent channel flow as an example.

In order to investigate the role of the coupling term in fully turbulent flows, we proceed to solve the following modified nonlinear equations:

$$\frac{d}{dt} \begin{bmatrix} \hat{v} \\ \hat{\omega}_y \end{bmatrix} = \begin{bmatrix} L_{os} & 0 \\ 0 & L_{sq} \end{bmatrix} \begin{bmatrix} \hat{v} \\ \hat{\omega}_y \end{bmatrix} + \begin{bmatrix} \mathcal{N}_v \\ \mathcal{N}_{\omega_y} \end{bmatrix}. \quad (5)$$

This modified system can be viewed as representing a synthetic turbulent flow without the coupling term, or a turbu-

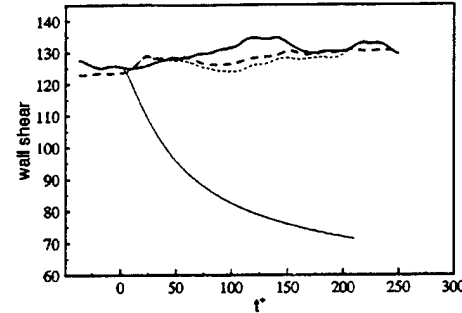


FIG. 1. Time evolution of mean shear at wall: —, upper wall; — — —, lower wall. Thick lines are for a regular channel flow, while thin lines are for a channel flow with $L_c = 0$ in the upper half of the channel starting from $t^+ = 0$.

lent flow with control by which the coupling term is suppressed. For instance, surface blowing and suction activated to eliminate (reduce) the spanwise variation of v (i.e., $\partial v / \partial z$) could eliminate (reduce) the effect of the coupling term.

A spectral channel code similar to that of Kim *et al.*¹⁰ was used to solve the above modified nonlinear equations. To further contrast the role of the coupling term, we used the modified N-S equations only in the upper half of the channel and the regular N-S equations in the lower half of the channel. We used the same Reynolds number ($\text{Re}_\tau = 100$) and grid ($32 \times 65 \times 32$ in x, y, z) as Lee *et al.*¹¹

In the first numerical experiment, we used a regular turbulent velocity field obtained by Lee *et al.* as our initial field. Starting from this initial field, we integrated in time to see how the turbulent flow in the upper half of the channel evolves in the absence of the coupling term. Time evolution of the mean shear at both walls is shown in Fig. 1, which illustrates a drastic reduction in the wall shear without the coupling term. Several snapshots of the velocity field are shown in Fig. 2, where contours of streamwise vorticity in a

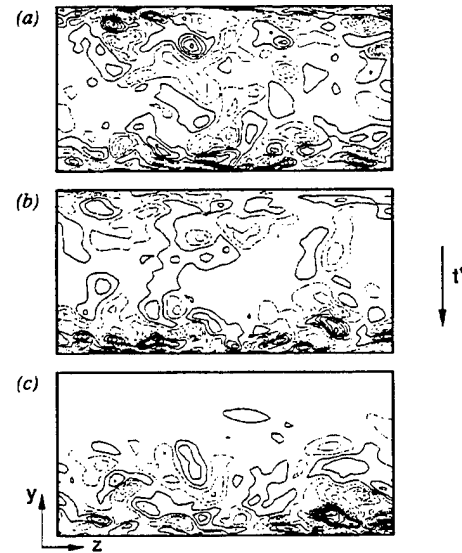


FIG. 2. Contours of streamwise vorticity in $y-z$ plane: (a) $t^+ = 0$; (b) $t^+ = 20$; (c) $t^+ = 200$. $-80 < \omega_x < 80$ with 18 contour levels. Note that $L_c = 0$ only in the upper-half of the channel.

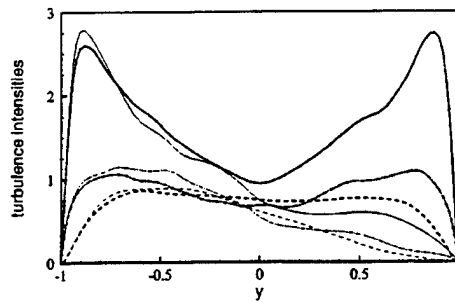


FIG. 3. Root-mean-square turbulence intensities: —, $\sqrt{u^2}$; - - -, $\sqrt{v^2}$; - · - · -, $\sqrt{w^2}$. Thick lines are for $t^+ = 0$, while thin lines are for $t^+ = 180$.

$y-z$ plane are shown to illustrate the effect of the coupling term on turbulence structures. It is evident that streamwise vortices quickly disappear without the coupling term. The reduction of the wall shear in conjunction with the disappearance of the streamwise vortices is a common feature of many drag-reduced turbulent flows.¹¹ Turbulence intensities shown in Fig. 3 indicate drastic reductions without the coupling term.

In the second numerical experiment, we used an initial velocity field consisting of the same mean velocity as the first experiment but with random disturbances, and hence, there are no organized turbulence structures present initially. A divergence-free white-noise spectrum was used for this purpose. The amplitude was chosen such that neither they decay too quickly (too small) nor they cause a numerical instability due to non-smoothness of the initial condition (too

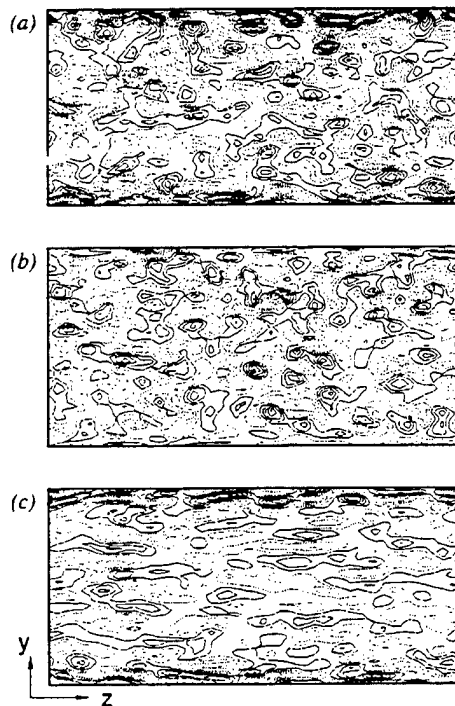


FIG. 4. Contours of streamwise vorticity in $y-z$ plane at $t^+ = 20$, started from an initial random field: (a) Case 1, regular turbulent flow; (b) Case 2, without the linear coupling term, L_c ; (c) Case 3, without the nonlinear terms. Contour levels are the same as Fig. 2.

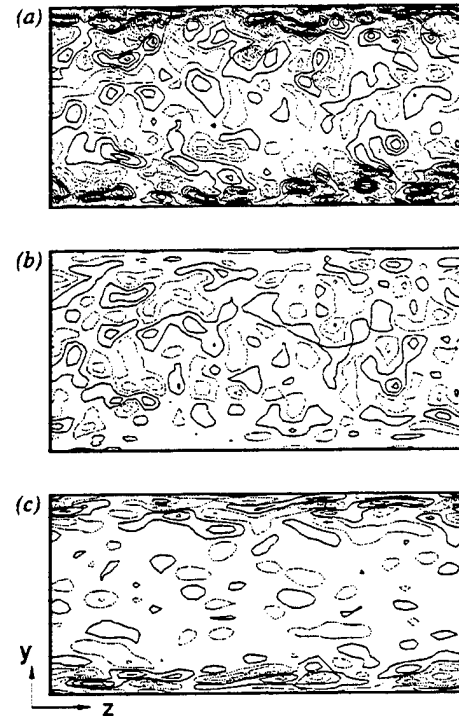


FIG. 5. Contours of streamwise vorticity in $y-z$ plane at $t^+ = 40$, started from a random initial field. See figure caption in Fig. 4 for legend.

large). Starting with the same random initial field, three different simulations were carried out: Case 1, with the full nonlinear N-S equations (i.e., regular turbulent flow); Case 2, with N-S equations without the linear coupling term; Case 3, with N-S equations without the nonlinear terms (i.e., linearized N-S). The purpose of these simulations is to investigate whether the linear coupling term is indeed responsible for formation of the streamwise vortices and near-wall streaks, and if so, whether the time scale associated with the formation of these structures corresponds to the bursting process ($t^+ \approx 100$), as hypothesized by Butler and Farrell.⁴

Time evolution of the three velocity fields is shown in Figs. 4–6 with streamwise vorticity contours in a $y-z$ plane. Organized structures are discernible in all three cases as early as $t^+ = 20$ (Fig. 4), but they look different from each other. For Case 3 (without the nonlinear terms), the structures that appear from the structureless random initial condition have larger spanwise scales than those in the regular flow (Figs. 4 and 5). For Case 2 (without the linear coupling term), the vortical structures appear briefly (Fig. 4) but disappear quickly, especially in the wall region (Figs. 5 and 6), since they cannot be maintained without the linear coupling term as demonstrated in the first experiment mentioned above. For Case 1, the time for these structures to appear is shorter than that implied by the optimal disturbance mechanism of Butler and Farrell.⁴ Note that the structures in Case 3 are already substantially different from those in Case 1 at $t^+ = 40$, indicating that the effect of nonlinear terms is felt much earlier than the eddy turnover time ($t^+ \approx 100$) as proposed by Butler and Farrell.⁴ The present result is also consistent with Jiménez and Pinelli,¹² who showed that the formation of streaky structures can be prevented by damping

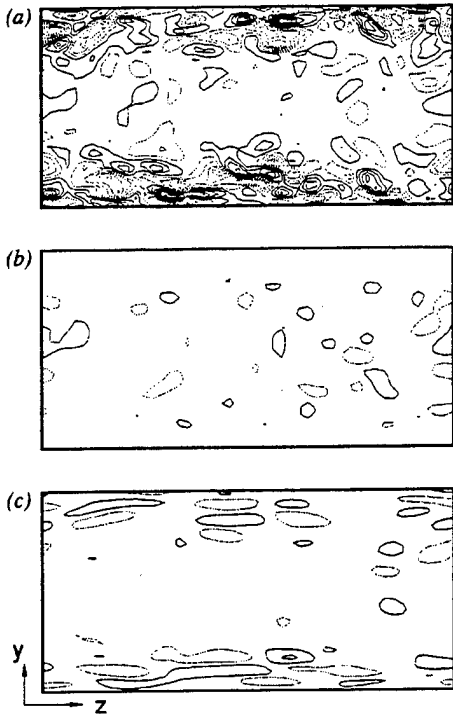


FIG. 6. Streamwise contours in $y-z$ plane at $t^+ = 80$, started from a random initial field. See figure caption in Fig. 4 for legend.

$\langle v \omega_z \rangle$ [the $\langle \rangle$ indicates streamwise average], which is related to the linear coupling term. While both results clearly demonstrate the essential role of the linear coupling term in the formation and maintenance of the wall-layer streaks, while the present work also indicates that a nonlinear mechanism is responsible for producing the proper streak spacing.

We have used several different initial conditions to determine whether the above results depend on initial conditions, but found no such evidence. It thus appears that both the nonlinear terms and the linear coupling term are necessary for the formation and maintaining of these structures at their proper scale. The nonlinear terms are necessary for the formation of streamwise vortices and the linear coupling term is necessary to generate the wall-layer streaks, the instability of which in turn strengthens the streamwise vortices through a nonlinear process. In the absence of either mechanism, turbulence ceases to exist. The result of this second experiment is consistent with Hamilton *et al.*¹³ and Waleffe and Kim¹⁴ in that the formation of the streamwise vortices is a result of a nonlinear process.

We have demonstrated that the linear process associated with the coupling term plays an important role even in fully nonlinear wall-bounded turbulent shear flows. Near-wall streamwise vortices, which play the essential role in the dynamics of wall-bounded shear flows, are seen to be formed but cannot be sustained without the coupling term.

This result is consistent with the analysis by Henningson and Reddy¹⁵ who showed that non-normality of the linearized Navier-Stokes operator is a necessary condition for disturbances to grow for Reynolds number below the critical Reynolds number predicted by the traditional linear stability analysis. However, we believe this is the first direct demon-

stration that turbulence (nonlinear disturbance) decays when the non-normality of the underlying linear operator in nonlinear flows is reduced. The time scale associated with the formation is found to be smaller than the bursting process used in the optimal perturbation theory. The fact that the coupling term plays an essential role in maintaining the streamwise vortices, which have been found to be responsible for high skin-friction drag in turbulent boundary layers, suggests that an effective control algorithm for drag reduction should be aimed at reducing the effect of the coupling term in the wall region. In fact, the opposition control used by Choi *et al.*¹⁶ can be viewed as a control scheme trying to reduce the effect of the coupling term by suppressing the spanwise variation of v in the wall region. It should be interesting to design a control algorithm that directly accounts for the coupling term in a cost function to be minimized.

A portion of this work was carried out while the first author was visiting the Isaac Newton Institute for Mathematical Sciences at Cambridge University. This work has been supported by the Air Force Office of Scientific Research (F49620-97-10276, Dr. Marc Jacobs). The computer time has been provided by the San Diego Supercomputer Center.

^aAuthor to whom correspondence should be addressed. Telephone: (310)825-4393; Fax: (310)206-4830. Electronic mail: jkim@seas.ucla.edu

- ¹K. M. Butler and B. F. Farrell, "Three-dimensional optimal perturbations in viscous shear flow," *Phys. Fluids A* **4**, 1637 (1992).
- ²B. F. Farrell and P. J. Ioannou, "Stochastic forcing of the linearized Navier-Stokes equations," *Phys. Fluids A* **5**, 2600 (1993).
- ³S. C. Reddy and D. S. Henningson, "Energy growth in viscous channel flows," *J. Fluid Mech.* **252**, 209 (1993).
- ⁴K. M. Butler and B. F. Farrell, "Optimal perturbations and streak spacing in wall-bounded turbulent shear flow," *Phys. Fluids A* **5**, 774 (1993).
- ⁵S. S. Joshi, J. L. Speyer, and J. Kim, "A systems theory approach to the feedback stabilization of infinitesimal and finite-amplitude disturbances in plane Poiseuille flow," *J. Fluid Mech.* **332**, 157 (1997).
- ⁶S. S. Joshi, J. L. Speyer, and J. Kim, "Finite dimensional optimal control of Poiseuille flow," *J. Guid. Control Dyn.* **22**, 340 (1999).
- ⁷L. Cortelezzi, K. H. Lee, J. Kim, and J. L. Speyer, "Skin-friction drag reduction via robust reduced-order linear feedback control," *Int. J. Comp. Fluid Dyn.* **11**, 79 (1998).
- ⁸K. H. Lee, *A Systems Theory Approach to Control of Transitional and Turbulent Flows*, Ph.D. dissertation, University of California at Los Angeles (1999).
- ⁹T. R. Bewley, "Linear control and estimation of nonlinear chaotic convection: Harnessing the butterfly effect," *Phys. Fluids* **11**, 1169 (1999).
- ¹⁰J. Kim, P. Moin, and R. K. Moser, "Turbulence statistics in fully developed channel flow at low Reynolds number," *J. Fluid Mech.* **177**, 133 (1987).
- ¹¹C. Lee, J. Kim, D. Babcock, and R. Goodman, "Application of neural networks to turbulence control for drag reduction," *Phys. Fluids* **9**, 1740 (1997).
- ¹²J. Jiménez and A. Pinelli, "The autonomous cycle of near-wall turbulence," *J. Fluid Mech.* **389**, 335 (1999).
- ¹³J. M. Hamilton, J. Kim, and F. Waleffe, "Regeneration mechanisms of near-wall turbulence structures," *J. Fluid Mech.* **287**, 317 (1995).
- ¹⁴F. Waleffe and J. Kim, "How streamwise rolls and streaks self-sustain in a shear flow," in *Self-Sustaining Mechanisms of Wall Turbulence*, edited by R. L. Panton (Computational Mechanics Publications, Southampton, UK and Boston, USA, 1997), pp. 309-332.
- ¹⁵D. S. Henningson and S. C. Reddy, "On the role of linear mechanism in transition to turbulence," *Phys. Fluids* **6**, 1396 (1994).
- ¹⁶H. Choi, P. Moin, and J. Kim, "Active turbulence control for drag reduction in wall-bounded flows," *J. Fluid Mech.* **262**, 75 (1994).